DEVELOPMENT OF AEROSOL CHEMICAL IONIZATION MASS SPECTROMETRY FOR THE STUDY OF ORGANIC PARTICLES

by

JOHN DANIEL HEARN

(Under the Direction of Geoffrey D. Smith)

ABSTRACT

An aerosol chemical ionization mass spectrometer (A-CIMS) has been developed for the study of organic particles. The low degree of fragmentation from this soft ionization technique enables detection of intact molecular ions which simplifies quantification and identification, especially in complex mixtures. Chemical ionization also allows flexible ionization which allows organic functional groups to be selectively ionized. For example, alkanes are not detectable with proton transfer ionization from protonated water clusters, but NO^+ will ionize them. The instrument has been calibrated and it is sensitive to organics near its calculated detection limit, and efforts have been made to reduce this limit further through off-line or on-line particle concentration. As examples of the utility of A-CIMS, heterogeneous reactions involving ozone, OH, or Cl attack on organic particles have been investigated as a function of particle phase and morphology. Accurate measurements of heterogeneous kinetics with A-CIMS have reconciled discrepancies among other published results. Products from these reactions have also been detected, and since A-CIMS is sensitive to both gas and condensed phases, it gives a more complete picture of particle evolution. The implications of the

results of these heterogeneous reaction studies are discussed in the context of atmospheric chemistry.

INDEX WORDS: organic aerosol, chemical ionization, heterogeneous, ozone, oleic acid, dioctyl sebacate, hydroxyl radical, chlorine radical, uptake coefficient

DEVELOPMENT OF AEROSOL CHEMICAL IONIZATION MASS SPECTROMETRY FOR THE STUDY OF ORGANIC PARTICLES

by

JOHN DANIEL HEARN

Bachelor of Arts, Asbury College, 2001

A Dissertation Submitted to the Graduate Faculty of The University of Georgia in Partial Fulfillment of the Requirements for the Degree

DOCTOR OF PHILOSOPHY

ATHENS, GEORGIA

2007

DEVELOPMENT OF AEROSOL CHEMICAL IONIZATION MASS SPECTROMETRY FOR THE STUDY OF ORGANIC PARTICLES

by

JOHN DANIEL HEARN

Major Professor: Geoffrey D. Smith

Committee: Michael A. Duncan
Nigel G. Adams

Electronic Version Approved:

Maureen Grasso
Dean of the Graduate School
The University of Georgia
May, 2007

DEDICATION

This work is first of all, dedicated to my Lord and Savior, Jesus Christ. He has provided an incredibly beautiful and complex creation to study and admire, and I am eternally grateful for the mind that he has given me that I can comprehend, at least in some small way, the world that He has made. Second, I want to dedicate this to my loving wife who has been patient as I pursue this degree. She is a wonderful companion and makes me want to be a better man. Finally, this is dedicated to my parents who have provided a wonderful home to grow up in and played an integral role in my development.

ACKNOWLEDGEMENTS

First, I acknowledge my advisor, Geoffrey Smith, for the leadership and friendship that he has provided these past few years. The work I presented here would not exist if it were not for Geoff. I would also like to acknowledge Lisabeth Hoffman, Jeremy Wolff, and Jon Amster for their help with the FTMS work I present in Chapter 7. Finally, I acknowledge Jon Washington at the EPA with his generosity in letting me use his differential scanning calorimeter for some measurements I made for Chapter 4.

TABLE OF CONTENTS

Page

LIST OF ABBREVIATIONS

Name	Abbreviation
Aerodynamic particle sizer	APS
Aerosol chemical ionization mass spectrometer	A-CIMS
Bis (2-ethylhexyl) sebacate	DOS
Chlorine radical	Cl
Docosane	DO
Excited Criegee Intermediate	ECI
Fourier transform mass spectrometer	FTMS
Hydroxyl radical	OH
Lauric acid	LA
Myristic acid	MA
Oleic acid	OL
Palmitic acid	PA
Scanning mobility particle sizer	SMPS
Stabilized Criegee Intermediate	SCI
Stearic acid	SA

CHAPTER 1

INTRODUCTION TO ATMOSPHERIC CHEMISTRY OF ORGANIC PARTICLES

1.1 Introduction to the field of atmospheric chemistry

Earth's atmosphere is composed of several isolated layers that exhibit complex chemical and physical processes. The troposphere is the lowest layer characterized by a decrease in temperature with increasing altitude. It extends approximately 10 km in elevation, but the actual boundary of the troposphere varies with latitude and diurnal and seasonal cycles. Above the troposphere is the stratosphere where the temperature increases with altitude because of the increased absorption of solar radiation and it houses the protective ozone layer. Above the stratosphere are the mesosphere and thermosphere, and while there is rich chemistry at all levels of earth's atmosphere [1], the focus of this work will be on reactions that are relevant in the troposphere.

The troposphere plays important roles in many cyclic processes in the biosphere where there is a balance among sources, sinks, and reservoirs of many chemicals. Some of the better known cycles are the hydrolytic cycle, carbon cycle, and nitrogen cycle. In order to have a correct understanding of the atmosphere, sources and sinks must be characterized, and it is critical to understand what happens to the material between the source and the sink. Some of the questions that research in the field of atmospheric chemistry tries to answer are:

1. What are the sources of gases and particles?
2. What are the chemical lifetimes of gases and particle components?

3. What are the physical lifetimes of particles?
4. What are the effects on human health?
5. What products are produced from chemical reactions?
6. What are the sinks for gases and particles?
7. What policies should be put in place to minimize anthropogenic influences on atmospheric chemistry?

There are a variety of approaches to answering these questions, and the flow chart in Figure 1.1 shows some broad categories of research in atmospheric chemistry. The three broadest categories are field measurements, laboratory measurements, and mathematical modeling. Almost all of the results presented in this manuscript fall under "laboratory measurements" with an emphasis on how organic aerosol particles chemically evolve in the atmosphere (follow the bold arrows in Figure 1.1). The challenge, as you will see, is to make the predictions from laboratory measurements consistent with field observations.

The remainder of this introduction will serve to give relevant background information for understanding the importance and context of heterogeneous chemistry (reactions between solid or liquid particles and gas phase species) in the atmosphere. I will start by describing some of the relevant sources and sinks of ambient aerosol, then I will list some impacts particles can have on climate and atmospheric processes, and finally, I will outline the goals of these studies.

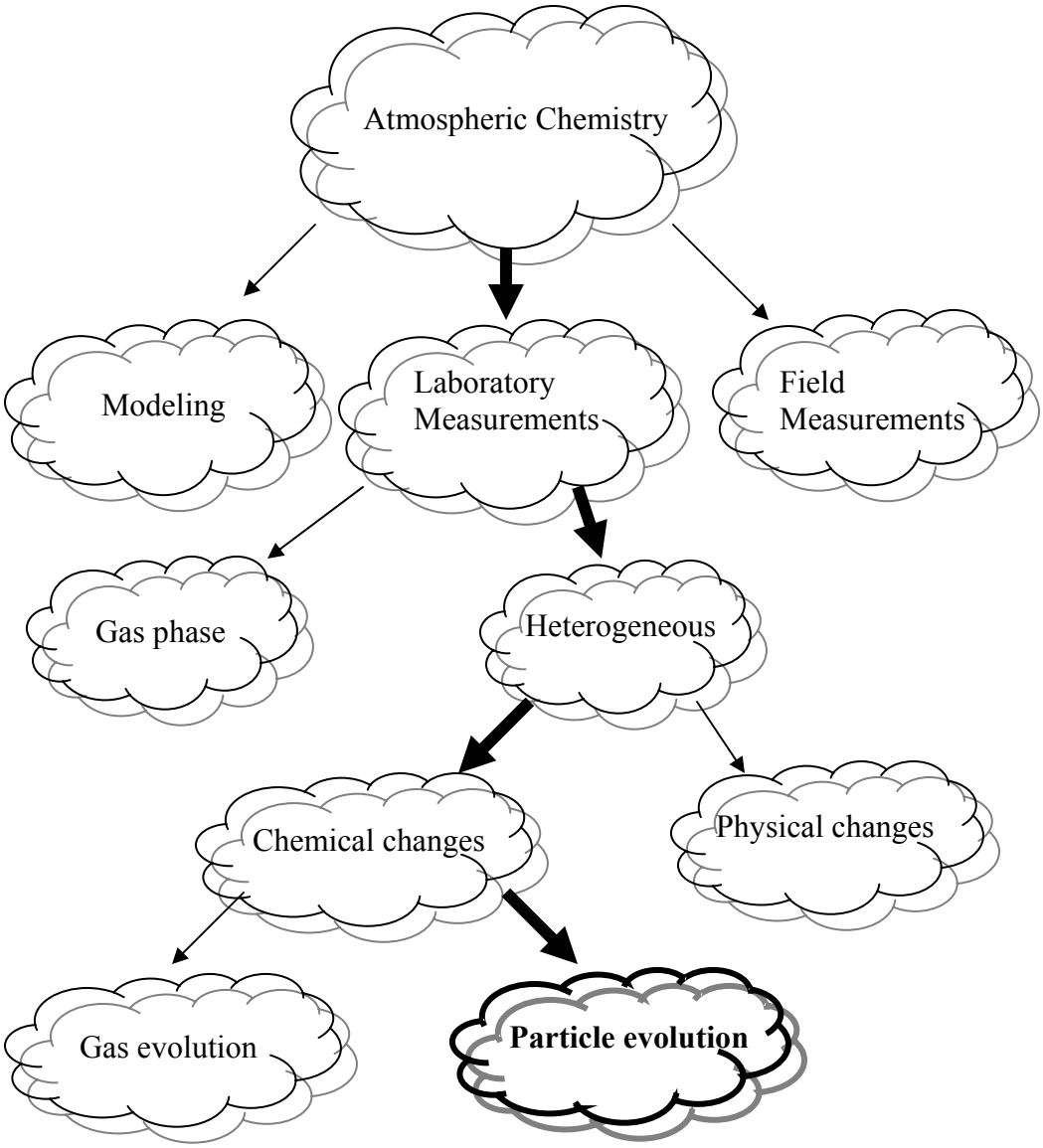

Figure 1.1. Flow chart for the field of atmospheric chemistry showing how we contribute.

1.2 Sources and sinks of ambient aerosol particles

There are a variety of sources of aerosol particles in the atmosphere such as volcanic eruptions, biogenic emissions, wind blown dust, sea spray, secondary organic aerosol, and forest fires to name a few natural ones. Anthropogenic emissions include

automobile exhaust, coal fired power plants, and other combustion processes [1]. The particles from each of these sources have characteristic chemical compositions. For example, volcanoes emit large amounts of sulfur, sea spray generates salt particles, and combustion processes produce elemental and organic carbon [1, 2]. Of course, there will be a variety of elements produced from each source, but each will have a characteristic "fingerprint". Additionally, the particle size distributions are dependent on its source. For example, mechanically generated particles are very large (diameter > 10 μm) and tend to exhibit the composition of the material they were made from (e.g. soil). Secondary organic aerosol formation, on the other hand, can generate new particles (diameter < 10 nm) or cause existing particles to grow (diameter > 10 nm) through the partitioning of low volatility products from gas phase reactions to nuclei or particles.

Interestingly, both inorganic and organic compounds are found in aerosol particles ubiquitously [1]. Their relative abundance will depend on the proximity to their sources, so organic particles will comprise a larger fraction of the aerosol mass in urban areas than in remote regions. In addition to their global presence, condensed phase organics are found on ambient particles in all size fractions (diameter = 2 nm – 100 μm).

While particle sources are varied and abundant, there are only two significant sinks of ambient particulate matter: wet and dry deposition. The only difference between these two deposition processes is their water content when they impact a surface. Wet deposition is the removal of particles through rain, and dry deposition is the removal of particles through diffusion or settling toward a surface. Since both will be dependent on the meteorology of the local environment, it is difficult to estimate their relative importance. However, dry deposition will be more important in arid regions whereas wet

deposition will be more important in regions with heavier rainfall. Additionally, dry deposition will be dependent on the particle size. Larger particles have a much faster deposition velocity, and this is what sets the upper limit on the operational definition of an aerosol particle (diameter < 100 μm). The deposition rate is proportional to the square of the radius of the particle, so small particles will have much slower deposition velocities. Instead, particles below 200 nm diameter will have a dry deposition rate that is dependent on their diffusion [1].

Therefore, the lifetime of particles will be dependent on their sizes, altitude, and the meteorological conditions. Estimates range from 1-5 days at lower altitudes and up to a month at higher altitudes [3]. This is important because when extrapolating laboratory kinetic measurements (such as those presented here) to atmospheric conditions, it provides an estimate on the reaction time. Some reactions will be too slow to contribute significantly to the chemical evolution of particles before they are removed from the atmosphere.

1.3 Particles in the atmosphere

The lifetime of particles in the atmosphere is between 1 and 30 days, so what are they doing there before their removal? Particles are involved in a number of atmospheric processes, and their most obvious effect is their ability to scatter and absorb solar radiation. The haze that is present in many cities is due to this aerosol direct effect, and the scattering and absorption cross-sections are dependent on particle sizes and compositions. On a global scale, the scattering of solar radiation by aerosol particles may have impacts on global climate change by attenuating the light that reaches the surface,

but currently, there is a large uncertainty on the magnitude of this effect because particles also scatter and absorb radiation emitted from the earth's surface [1].

Another important role of aerosol particles is cloud albedo. If particles take up water efficiently, they can act as cloud condensation nuclei (CCN), and cloud cover has important implications in radiative forcing and precipitation. The ability of a particle to grow into a cloud droplet is a function of both its size and composition. Particles that are more hygroscopic will more easily take up water than particles with hydrophobic constituents. Therefore, aerosol particle sources and the subsequent heterogeneous chemical modifications are important parameters to consider when predicting whether they will act as CCN [1].

Particles can also have important human heath impacts, and in large cities there is a direct correlation between excess deaths (death rate larger than average) and the aerosol concentration [4]. This primarily affects the elderly and those with breathing problems, but long-term exposure to high aerosol concentrations can contribute to lung deficiencies (e.g. pneumoconiosis, "black lung disease"). This provides additional motivation for studying aerosol particles because the impacts on human health are dependent on size and composition [1].

Finally, it has been proposed that particles can act as sinks for reactive gases such as HO_2 [5, 6], and particles can be sources of gas phase molecules. So even to have a complete understanding of gas phase chemistry in the atmosphere, the contribution of heterogeneous reactions must be included. It is important, therefore, to quantify the significance of particles as sinks and sources of gas phase molecules and radicals.

1.4 Goals of this work

As described above, organic particles are ubiquitous in the troposphere, and they have impacts on visibility, climate, human health, and gas phase reactions. Since particle composition and size are involved to some degree in all of these effects, it is not only necessary to chemically and physically characterize particle sources, but the chemical and physical evolution of particles in the atmosphere need to be well understood too. This includes accurately predicting rates of heterogeneous reactions and product branching ratios from those reactions. The work presented here has been done with the goal of obtaining a better understanding of organic aerosol evolution.

There are several different approaches to studying heterogeneous reactions of organic aerosols, and we have set out to build a custom chemical ionization mass spectrometer for the study of organic aerosol. I will first describe this analytical technique and how it compares to other similar techniques in measuring aerosol particle composition. The aerosol chemical ionization mass spectrometer (A-CIMS) will then be characterized and tested to ensure that its performance is optimum.

After the instrument has been shown to be working correctly, I will describe studies on three classes of reactions. First will be the reaction between ozone and particles composed of unsaturated organic molecules in order to compare the A-CIMS results to previous studies. Second, ozonolysis of oleic acid particles will be used to examine phase and morphology effects on organic aerosol reactivity by generating binary mixtures where the second component is a solid. Finally, radical initiated reactions will be studied with a mixed phase relative rates approach to measure the kinetics of

oxidation. Additionally, chemical and physical changes will be measured with a variety of techniques to determine the fate of radically oxidized organic particles.

After these studies on heterogeneous reactions, I will put A-CIMS to the test by analyzing complex particles from some common particle sources and detecting ambient particle components in real-time. There will be some effort to improving the detection limit of the instrument, and in the last chapter, I will give some suggestions for further improvements to A-CIMS.

References

1. Finlayson-Pitts, B.J. and J.N.J. Pitts, *Chemistry of the Upper and Lower Atmosphere*. 2000, San Diego, CA: Academic Press. 969.

2. Rogge, W.F., et al., *Sources of Fine Organic Aerosol .2. Noncatalyst and Catalyst-Equipped Automobiles and Heavy-Duty Diesel Trucks.* Environmental Science & Technology, 1993. **27**(4): p. 636-651.

3. Williams, J., et al., *Application of the variability-size relationship to atmospheric aerosol studies: estimating aerosol lifetimes and ages.* Atmospheric Chemistry and Physics, 2002. **2**: p. 133-145.

4. Ito, K., et al., *Associations of London, England, Daily Mortality with Particulate Matter, Sulfur-Dioxide, and Acidic Aerosol Pollution.* Archives of Environmental Health, 1993. **48**(4): p. 213-220.

5. Saylor, R.D., *An estimate of the potential significance of heterogeneous loss to aerosols as an additional sink for hydroperoxy radicals in the troposphere.* Atmospheric Environment, 1997. **31**(21): p. 3653-3658.

6. Thornton, J. and J.P.D. Abbatt, *Measurements of HO2 uptake to aqueous aerosol: Mass accommodation coefficients and net reactive loss.* Journal of Geophysical Research-Atmospheres, 2005. **110**(D8): p. -.

CHAPTER 2

INSTRUMENT DEVELOPMENT[1,2]

2.1 Introduction to Aerosol Mass Spectrometry

Aerosol mass spectrometry has dramatically changed the field of atmospheric chemistry by allowing real-time measurements of aerosol chemical composition both in the laboratory and in the field [1, 2]. This enables transient changes in particle composition to be measured within minutes whereas filtered samples can give time resolution of only a few hours [3]. Aerosol mass spectrometers are varied in their designs and capabilities, and in order to put the Aerosol Chemical Ionization Mass Spectrometer (A-CIMS) in the proper context, I will first briefly highlight some of the biggest differences among aerosol mass spectrometers.

One step in mass spectral analysis of particles is getting the sample into the gas phase in order to ionize, filter, and detect the components. This is accomplished by either thermal vaporization on a heated probe or capillary inlet (< 300°C) [4-6], flash vaporization on a heated surface (> 400°C) [7], or laser vaporization [8]. A few issues arise in choosing a vaporization method. First, fragmentation can occur more easily during the ionization process if the molecules are "hot" [9], and second, particles are not

---

[1] Hearn, J.D. and G.D. Smith, *A chemical ionization mass spectrometry method for the online analysis of organic aerosols.* Analytical Chemistry, 2004. **76**(10): p. 2820-2826. Copyright 2004 American Chemical Society. Reproduced in part with permission of the publisher.

[2] Hearn, J.D. and G.D. Smith, *Reactions and mass spectra of complex particles using Aerosol CIMS.* International Journal of Mass Spectrometry, 2006. **258**(1-3): p. 95-103. Reproduced in part with permission of the publisher.

always completely vaporized. Flash vaporization has problems with generating hot molecules, and laser vaporization only vaporizes portions of a particle. Therefore, we chose thermal vaporization which completely vaporizes particles without causing excessive heating and fragmentation. The trade-off is that thermal vaporization takes much longer (msec) than flash or laser vaporization (μsec.).

The second step in analyzing particles with mass spectrometry is ionization, and this plays the biggest role in fragmentation. Electron impact ionization is the most energetic way of generating ions, and organic molecules fragment significantly [10]. This can be useful because ambient particles are composed of hundreds of individual compounds and electron impact ionization collapses the entire ion signal into a few characteristic peaks in the mass spectrum that correspond to key functional groups. Photo-ionization, both multi- and single-photon, provides a gentler way of ionizing the particle constituents than EI [11]. Multi-photon ionization may still cause significant fragmentation of organic molecules, but the advantage here is that it can be used to vaporize and ionize particles in a single step [12]. Another ionization source that has been recently developed for use with aerosol particles is photo-electron resonance capture ionization (PERCI) [13]. This is a soft way to attach electrons to molecules in a particle plume with essentially no fragmentation; however, quantification is difficult [14] and organics without functional groups (alkanes) lack electron affinity and are not detectable with PERCI. Finally, we chose chemical ionization to detect aerosol particles because it is a very soft way of ionizing molecules [15]. The reagent ion can be tailored to ionize a species of interest, and it is sensitive to functionalized organics and alkanes.

One more characteristic of aerosol mass spectrometers warrants comment. Some monitor single particles and others monitor integrated particle signal from many particles. Single particle mass spectrometers use a time-of-flight mass analyzer so that all of the ions created are detected. Mass spectrometers that monitor integrated signal from many particles can use essentially any mass filter desired, but the most common are a time-of-flight or quadrupole mass filters [1, 2, 6].

We have set out to build an aerosol chemical ionization mass spectrometer (A-CIMS) in order to exploit the advantages of chemical ionization:

- soft ionization
- detection of intact molecular ions
- flexible ionization schemes
- simple experimental set-up (no critical timing involved)
- simultaneous detection of gas and condensed phases

However, chemical ionization is not without limitation:

- cannot detect single particles
- does not yield particle size information

In the rest of this chapter, I will describe the A-CIMS design, characterize its detection through particle and gas phase calibrations, and relevant parameters for obtaining the best detection. Additionally, particle generation techniques used for experiments in this manuscript are described. I would like to point out that recently, a commercial atmospheric chemical ionization mass spectrometer has been retrofitted for aerosol analysis by placing a modified heated capillary inlet before the ionization region [6, 16-18].

2.2 A-CIMS Design

The A-CIMS consists of a heated flow-limiting inlet, a heated chemical ionization region, differential pumping to transport the ions into high vacuum, and mass separation with a quadrupole mass analyzer. Figure 2.1 shows a schematic of the A-CIMS, and pictures are shown in Figure 2.2. The main difference between this system and other chemical ionization mass spectrometers is that the inlet and ionization regions are heated to vaporize particles. The two inlet designs used are an orifice inlet and a capillary inlet. The capillary inlet was adopted because it eliminates the need for o-rings and simplifies the design. The inlet is resistively heated to 200 – 300°C with a coil of nichrome wire, and the gas intake is 1.2 standard liters per minute (slpm). Reagent ions are generated by passing 2.0 slpm N_2 and a trace amount of another gas through an alpha emitter (^{210}Po, model P-2031, NRD, Grand Island, NY). Table 2.1 gives a summary of trace gases used and the corresponding reagent ions generated.

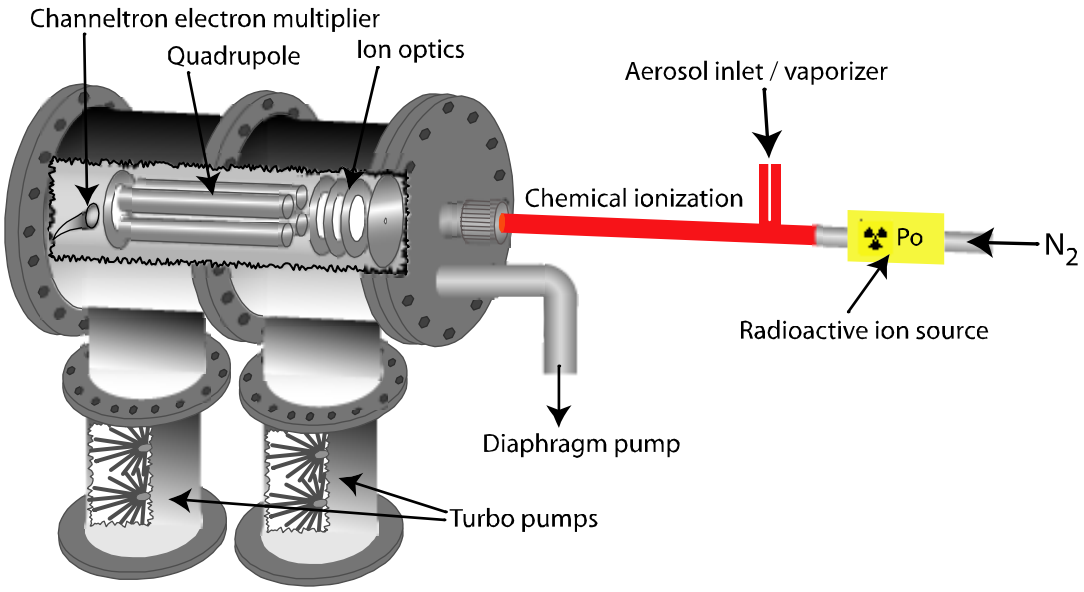

Figure 2.1. Schematic of Aerosol Chemical Ionization Mass Spectrometer.

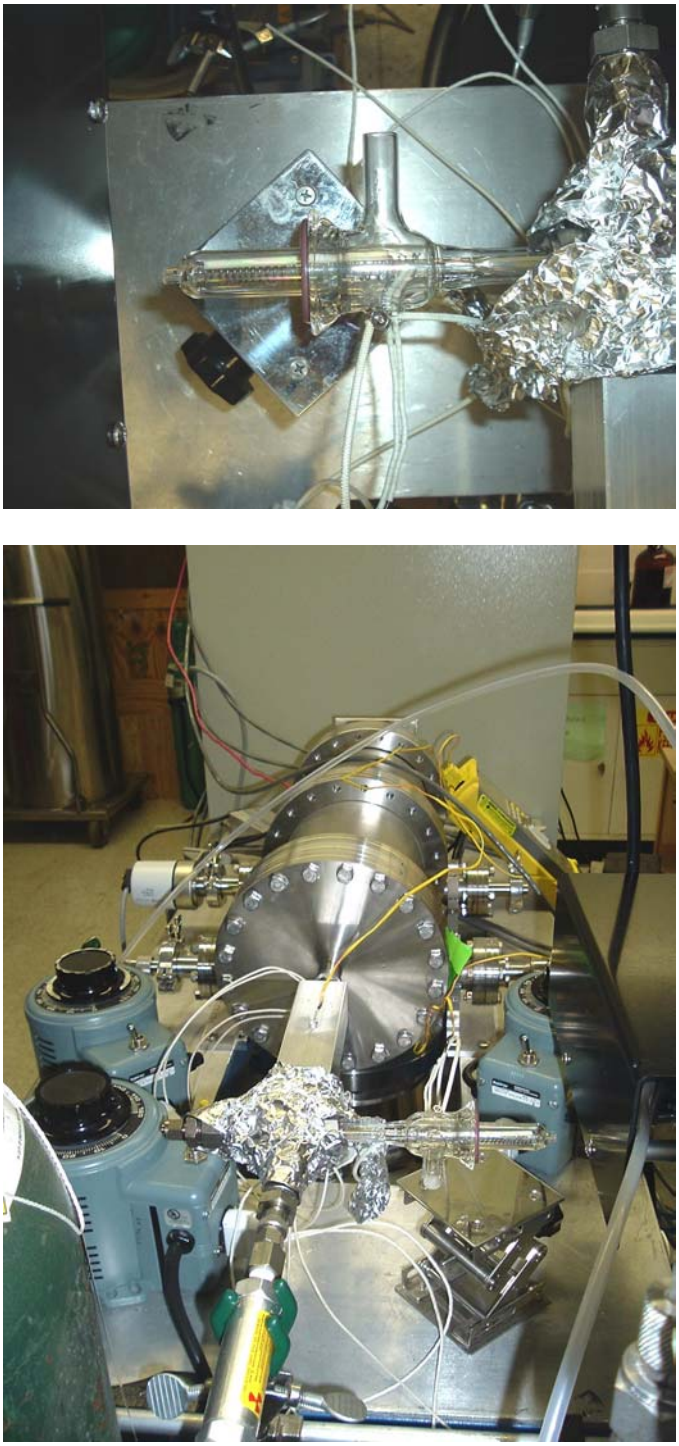

Figure 2.2. Photographs of the vaporizer (top) and the entire aerosol chemical ionization mass spectrometer system (bottom).

Table 2.1. Gases used to generate a variety of primary ions. LN trap indicates the flow was sent through a liquid nitrogen trap prior to the polonium.

Bath gas	Trace gas	Primary ion
N_2	O_2	$(H_2O)_nH^+$, n=2,3,4
N_2	NO	NO^+
N_2, LN trap	O_2, LN trap	O_2^+
N_2	O_2	O_2^-
N_2	SF_6	SF_6^-
N_2	NF_3	F^-

The reagent ion flow meets the sample flow at a 90º angle in a Swagelok tee. Chemical ionization occurs in a heated ¼ or ½ inch o.d. 25 cm long stainless steel tube (100 – 220ºC). At a pressure of 40 Torr this provides an ionization reaction time of 3 or 20 msec for the ¼ and ½ inch ion tubes, respectively. The ions are then sampled through either a 100 or 200 μm diameter orifice through differential pumping and a small potential gradient (≈ 3V) by placing a small charge on the orifice. To prevent the build-up of oil in the ion tube, an oil-free diaphragm pump is used to pump the excess flow from the ion tube. Otherwise, the oil from a mechanical pump can interfere with the ion chemistry and cause excessive background signal. The ions are then guided into the quadrupole mass filter with a series of electrostatic optics. Filtered ions exit the quadrupole and either impact on the dynode (positive ion detection) or the channeltron electron multiplier (negative ion detection). Recently, it has been found that the background noise at high m/z for positive ion detection can be drastically reduced by turning the dynode off. The poor performance of the dynode is probably caused by some degradation of the dynode or multiplier over time.

One important issue that needs to be addressed is the degree of vaporization, i.e. is the entire aerosol vaporized? There are three pieces of evidence that support the conclusion that organic aerosol is completely vaporized in the vaporizer. The first and easiest test is to simply turn the particle flow off and monitor the decay of the particle signal. Figure 2.3 shows the signal decay of oleic acid (OL) particles after the particle flow was stopped (t = 0 seconds), and the signal decreases with a time constant of 7.2 seconds. This is not much longer than the 5 second running average of the data acquisition, and the slightly longer time is probably due to residual particle concentration in the flow tube or injector. These results suggest that the vaporizer (> 200ºC) and ion tube (> 150ºC) are hot enough to prevent particles from depositing on the walls. The second test is to simply turn the heat up on the vaporizer and monitor the mass spectrometer signal while sampling a constant amount of aerosol. This results in no significant change in the organic signal and suggests that no additional vaporization is occurring in the vaporizer at higher temperatures (T > 200ºC, data not shown).

Third, we crudely measured the proton transfer reaction rate constant for an organic aerosol and compared it to a similar gas phase organic. This is a crude measurement because the flow is laminar (Re ≈ 250) and the reaction time is not well known. However, we calculated 21 msec for the reaction time from the pressure, flow, and dimensions of the ion tube. The rate constant was measured assuming a pseudo-first order reaction by adding excess organic aerosol into the system to deplete the protonated water cluster signal (m/z = 37) and plotting the natural logarithm of the water signal loss versus the organic aerosol concentration (in the ion tube). Figure 2.4 shows reaction decays for both OL and bis (2-ethylhexyl) sebacate (DOS). Organic particle

concentrations at the vaporizer entrance were measured with an aerodynamic particle sizer (APS model 3321, TSI inc.) in parallel with the A-CIMS measurement, and the concentrations were corrected for ion tube dilution and pressure. The slopes of these curves give k*t, and accounting for the reaction time, rate constants of 2.7 and 3.8 $\times 10^{-9}$ cm^3/molecule/second were obtained for OL and DOS, respectively. These rate constants are very close to proton transfer rate constants of other gas phase organics, such as acetone and acetic acid ($k_{PT} \approx 3 \times 10^{-9}$ cm^3/molecule/second) [19]. This doesn't provide direct evidence for complete vaporization of OL and BES particles; however, if significant amounts of OL and DOS remained in the condensed phase, it would cause a systematic positive error in the organic vapor concentration. This would translate into an underestimation of the proton transfer rate constant, but considering the good agreement with other work, these results corroborate the conclusion that OL and DOS particles are completely vaporized.

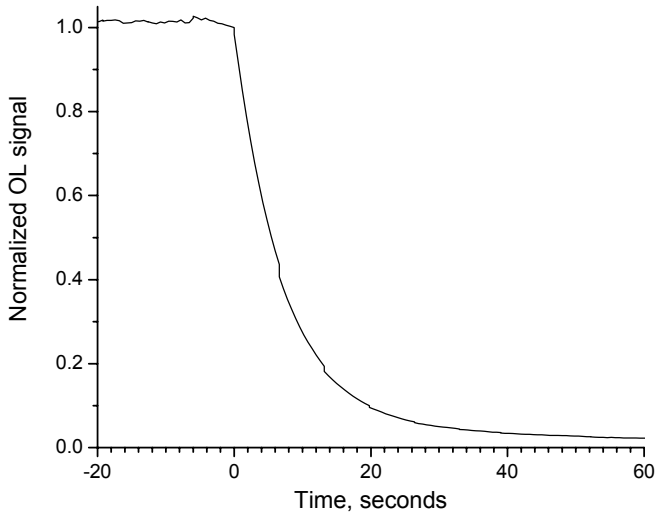

Figure 2.3. The OL particle flow was stopped at t = 0 seconds and the signal decreases with a time constant of 7.2 seconds. This is not much longer than the 5 second running average for data acquisition and indicates that particles are not depositing on the walls of the vaporizer or ion tube.

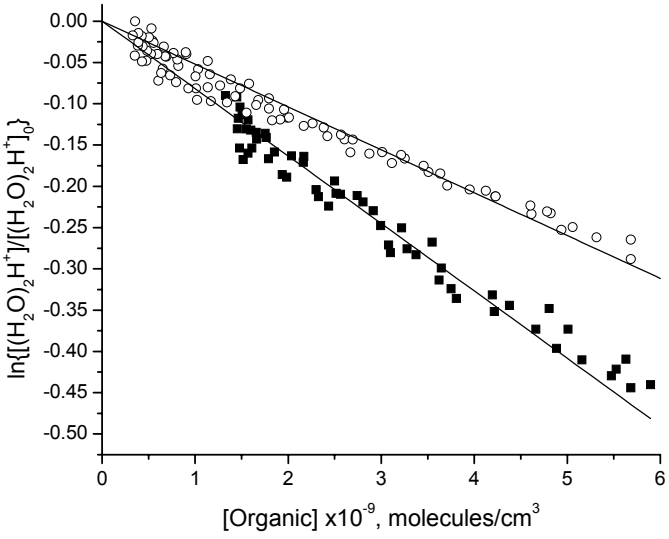

Figure 2.4. Plot of water signal (m/z = 37) vs. organic particle concentration. The lines are first order exponential fits to the data which yield proton transfer rate constants of 2.7 and 3.8×10^{-9} cm^3/molecule/second for OL (open circles) and DOS (closed squares), respectively.

2.3 Detection limits and Sensitivity

Chemical ionization (CI), as the name implies, relies on a chemical reaction to ionize molecules of interest. For optimum performance, the reagent ion signal needs to be very abundant, and the reaction time needs to be very long. The reason for these two conditions becomes apparent when the kinetic equations are analyzed. Equation (2.1) shows the solution for product ion (B^+) concentration as a function of reagent ion (A^+) concentration and reaction time (t) assuming pseudo first-order kinetics [20]. Equation (2.1) can be approximated by Equation (2.2) for less than 10% change in $[A^+]$, where the exponential term has been replaced by the first two terms in the Taylor expansion. This provides a linear relationship between the signal and concentration of the sample, and it can be used to determine theoretical detection limits and sensitivities.

$$[B^+] = [A^+]_0 \left(1 - e^{(-k[B]t)}\right) \tag{2.1}$$

$$[B^+] \approx [A^+]_0 k[B]t \tag{2.2}$$

With known proton transfer reaction rate constants, this allows the detection limit to be estimated and gives a benchmark for optimum performance of a chemical ionization system. For instance, assuming that a 200 count per second (cps) rise is the minimum signal for positive detection, a typical proton transfer rate constant ($k_{PT} \approx 3 \times 10^{-9}$ cm^3/molecule/sec) [19], a primary ion intensity of 10^6 counts per second (cps), and a reaction time of 20 msec, the detection limit for B in the ion tube is approximately 3×10^6 molecules/cm^3. Correcting for the ion tube dilution (1/3) and pressure (40 Torr), this yields a detection limit of 10^8 molecules/cm^3 in the flow tube at atmospheric pressure. A-CIMS ought to get reasonably close to this detection if the system is properly designed and tuned. For the remainder of this chapter, sample concentrations are those in the flow tube, not the ion tube.

In order to determine if A-CIMS is reaching its capability, it was calibrated first with a gas phase compound (NO_2) in order to simplify the instrument by removing the need for a heated inlet and ion tube. NO_2 was ionized via charge transfer from SF_6^-, and in order to demonstrate the importance of long reaction time in the ionization region, both 0.4 and 1.16 cm i.d. stainless steel tubes were used for the calibration. Figure 2.5 shows the results from three calibrations done under different conditions, and a few things warrant comment. First, all three plots are linear, providing evidence that a linear approximation for small changes in reagent ion intensity is valid. Second, there is a drastic improvement in sensitivity between the two different tubes used. The increase in detection sensitivity is nearly a factor of 350! A simple calculation of the reaction times

between the two tubes will show that there should only be an improvement of approximately a factor of 8. Clearly, there are other factors affecting the sensitivity which brings up the third point. A "turbulizer" was placed at the intersection of the sample and reagent ion flows in the smaller tube, and this improved the detection by about a factor of 30. This "turbulizer" was simply a small glass rod (≈ 1/8 in. diameter) that was placed in the swagelok "tee" so that it was at a right angle with respect to the ion tube flow. The improvement gained with the increased mixing explains almost all of the discrepancy between the calculated and observed increases in detection between the smaller and larger diameter tubes. Apparently, the larger diameter tube causes better mixing between the sample and reagent ion flows.

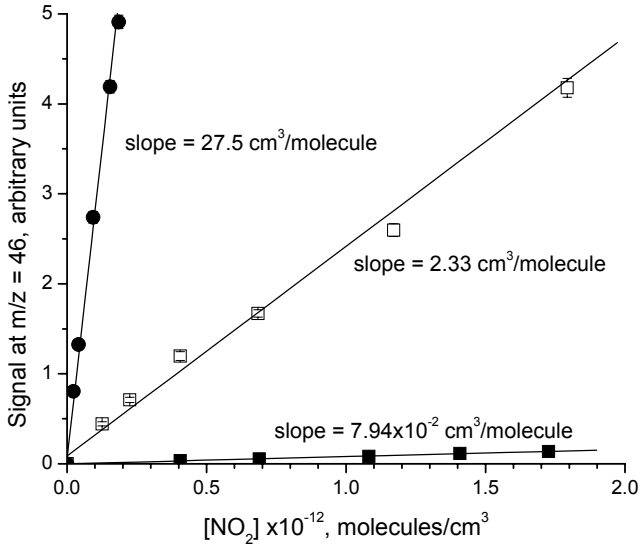

Figure 2.5. NO_2 calibration with ion tube inner diameters of 0.4 cm (squares) and 1.16 cm (circles) and with a "turbulizer" (open squares). Lines represent linear fits to the data. Note the increased detection with improved mixing (closed and open squares).

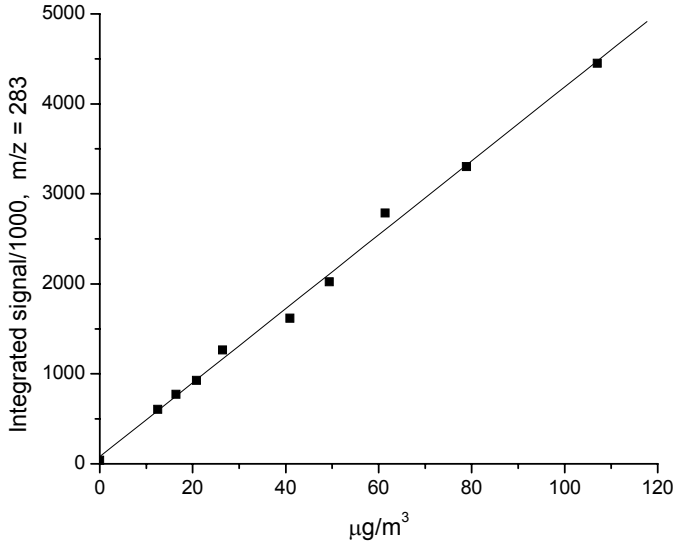

Figure 2.6. A-CIMS calibration of OL particles. The line represents a linear fit to the data ($R^2 = 0.966$), and the detection limit is 200 ng/m^3.

In order to demonstrate the usefulness of the A-CIMS for detecting organic aerosol, it was calibrated for oleic acid (OL) particles using proton transfer ionization from protonated water clusters ($(H_2O)_nH^+$, n = 2 or 3). OL particles were generated by nebulizing pure OL liquid into a 500 mL flask. Particles were then swept out of the flask with a small flow of N_2 (10-20 sccm) and immediately diluted with a large flow of N_2 (≈ 10 slpm). This flow was then split to enable simultaneous measurements on the A-CIMS and an aerodynamic particle sizer (APS model 3321, TSI inc.). The APS was used to measure the particle concentration (μg/m^3) entering the mass spectrometer and Figure 2.6 shows the results from this calibration.

The OL detection plot is linear ($R^2 = 0.996$), and this demonstrates that A-CIMS is not only useful for detection of condensed phase organics, but a linear approximation (Equation (2.2)) is also valid. From the slope of the plot in Figure 2.6 and a signal-to-noise ratio of 2, we calculate a detection limit of 200 ng/m^3 (4.3×10^8 molecules/cm^3).

This is only slightly larger than the detection limit calculated above (10^8 molecules/cm^3), and the good agreement verifies that A-CIMS is working properly. While this is a low detection limit, many organics exist in the atmosphere at several ng/m^3 or less, so A-CIMS is not well-suited for detecting ambient organic aerosol without the aid of a real-time concentrator [21]. However, laboratory measurements, which are the focus of this work, use much higher concentrations of organic aerosol, and from this OL calibration, it is evident that A-CIMS is a powerful analytical tool in the laboratory.

2.4 Ionization schemes

In order to demonstrate the capabilities of A-CIMS for detecting organic aerosol, single- and multi-component aerosols were analyzed with different ion schemes. Table 2.2 gives a summary of some of the trace gases used and how different functionalized organics are detected with each primary ion. For organics, the most general reagent ion is NO^+ which ionizes both functionalized organics and n-alkanes either by hydride abstraction to form $[M-H]^+$ or NO^+ addition to form $[M+NO]^+$. Figure 2.7 shows a spectrum of docosane chemically ionized with NO^+ (A) and ionized with electron impact (EI) ionization (B). In the A-CIMS spectrum, there is not an abundant amount of NO^+ adduct formed in this spectrum, but functionalized organics do show appreciable amounts of NO^+ addition in their spectra (data not shown). There is also more fragmentation of docosane than in spectra of functionalized organics (see below), but this is insignificant compared to the fragmentation electron impact ionization yields (panel B) [22]. The abundance of the molecular ion relative to the total ion current is 10 times higher in the A-CIMS spectrum than in the EI spectrum. While alkanes fragment more easily than

functionalized organics from chemical ionization the dominant peak is still the parent ion ($[M-H]^+$).

Table 2.2. Product ions detected from different organics with a variety of primary ions. ND = not detected, HA = hydride abstraction, PT = proton transfer, A = association, WL = water loss, CT = charge transfer, x = not obtained.

	Primary ion			
	$(H_2O)_2H^+$	NO^+	O_2^+	O_2^-
Docosane	ND	HA	x	x
1-Octadecene	PT	A	CT	ND
Oleyl alcohol	PT, WL	HA, A	WL	A
Octyl aldehyde	PT	HA, A	x	A
Oleic acid	PT, WL	HA, A	CT	PA, A

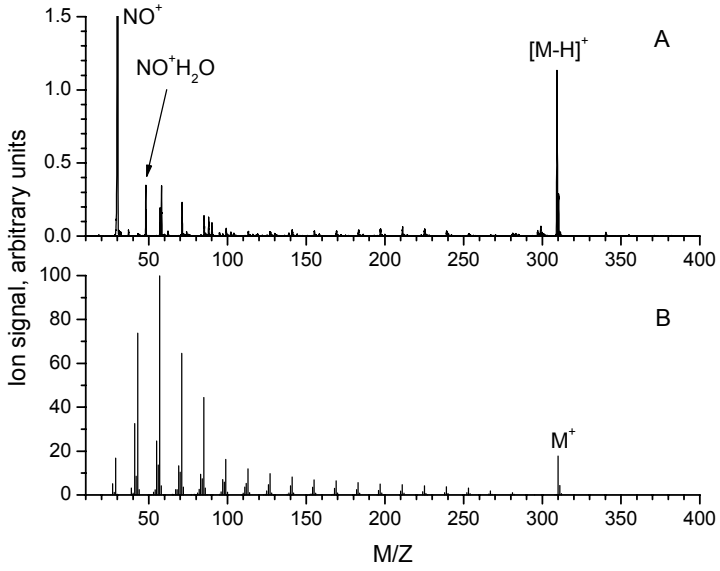

Figure 2.7. (A) A-CIMS spectrum of n-docosane particles using NO^+ as the primary ion. Docosane is detected as $[M-H]^+$ (m/z = 309). (B) Electron impact (EI) ionization mass spectrum of docosane. The molecular ion in the A-CIMS spectrum is 10 times higher than in the EI spectrum relative to the fragmentation.

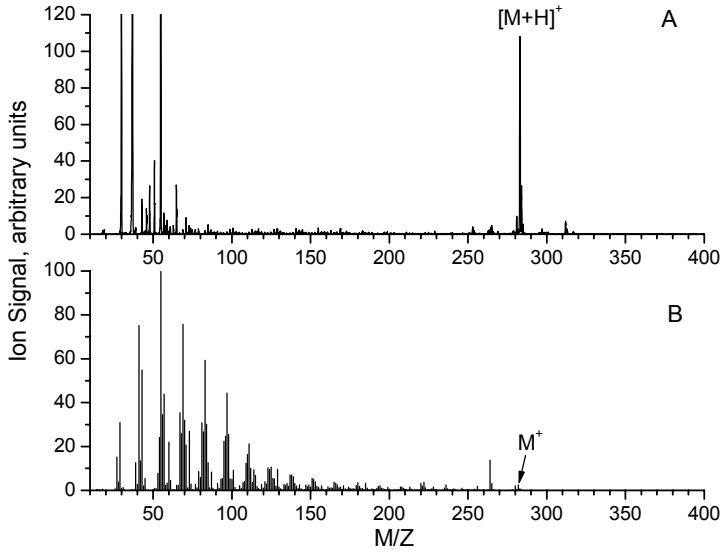

Figure 2.8. (A) A-CIMS spectrum of OL particles using proton transfer ionization from protonated water clusters. The primary OL ion is $[M+H]^+$ at m/z = 283 with a small contribution of $[M+NO]^+$ at m/z = 312 from an NO^+ contamination. The peaks below m/z = 75 are protonated water clusters, NO^+ peaks, and some small organic contamination. (B) Electron impact ionization mass spectrum of OL showing the M^+ peak with an 0.25% abundance of the total ion signal.

The second most general reagent ion is protonated water clusters ($(H_2O)_nH^+$, n = 2, 3, or 4), which is the predominate ion used in this work. It will ionize any organic with a functional group on it, and as an example, Figure 2.8 shows OL ionized via proton transfer. Here, the parent ion appears at one mass unit higher than OL (m/z = 283), and there is only some minor fragmentation from water loss (m/z = 265). The peaks at lower molecular weight (m/z = 100-200) are background organics and are unaffected by the presence of OL, and the peaks at m/z < 75 are protonated water clusters, NO^+ peaks, and contamination of small organics. In contrast to the A-CIMS spectrum, the EI spectrum is shown in panel B [22], and the molecular ion (M^+) only accounts for 0.25% of the total ion signal from OL. In the A-CIMS spectrum there are small peaks at m/z = 281 and 312 which correspond to the hydride abstraction and addition from NO^+ ionization of OL.

Unfortunately, there is a small source of NO^+ in the polonium, presumably from the reaction between O_2 and N atoms [23]. When the polonium flow is made entirely of O_2, the NO^+ peak disappears.

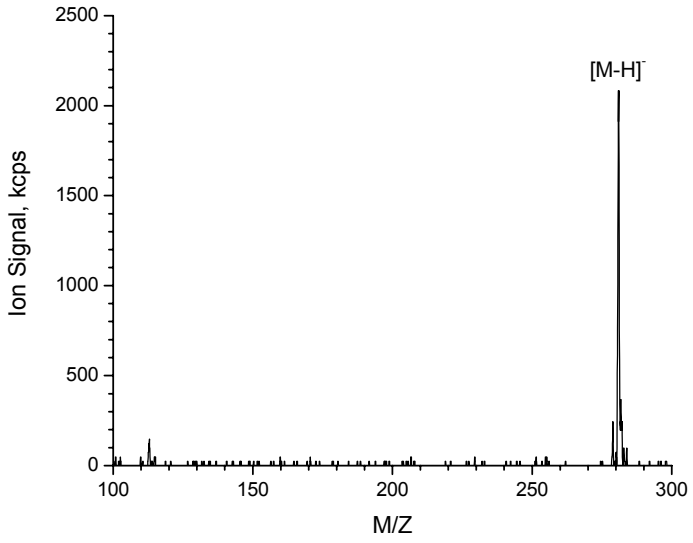

Figure 2.9. A-CIMS spectrum of OL particles using O_2^- as primary ion. OL is detected as $[M\text{-}H]^-$ at m/z = 281.

In addition to positive ionization, negative ionization can also be used to detect some organics. As an example, Figure 2.9 shows a spectrum of OL particles ionized with O_2^-. A peak appears at m/z = 281 via proton abstraction, and there is no evidence for fragmentation in this spectrum. In addition, there seems to be less contribution from background organics in the negative ionization spectrum. This is probably because it is more selective and less sensitive, so fewer of the background organics are detected. To demonstrate the use of selective ionization, Figure 2.10 shows OL particles that have been reacted with ozone, generating 4 products that are analogous to gas phase ozonolysis reactions (see Chapter 3 for more details): nonanal, nonanoic acid, 9-

oxononanoic acid, and azelaic acid [11, 13, 24-27]. With proton transfer, all four expected products are observed as well as some water loss fragments, and nonanal is the most abundant product ion. However, with proton abstraction (O_2^- ionization), only the acidic products are detected with any appreciable signal while nonanal is barely detected. Additionally, proton transfer ionization causes more extensive water loss fragmentation of the acidic products whereas there is no detectable fragmentation with proton abstraction ionization.

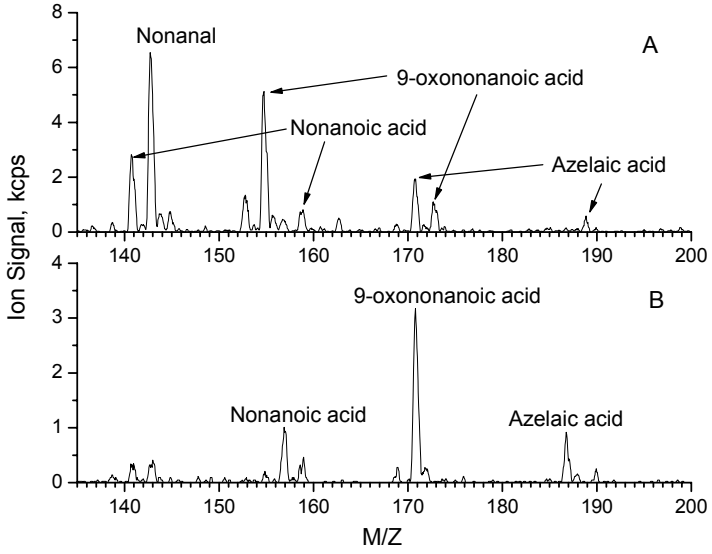

Figure 2.10. A-CIMS spectra of OL particles reacted with ozone and ionized with (A) proton transfer ionization and (B) proton abstraction ionization. Nonanal is not efficiently detected with proton abstraction ionization whereas the products containing carboxylic acid groups are.

While fragmentation in A-CIMS is impressively low, as seen above, it is not completely absent. Water loss peaks are observed in the proton transfer spectra of carboxylic acids, and docosane showed multiple fragment peaks (Figure 2.7). This will

be discussed in more detail in Chapter 5, but it is important to be aware of the significance a small amount of fragmentation can have on spectral interpretation especially when trying to determine product yields when product compounds are not commercially available. Factors that affect the fragmentation are the functional group accepting the charge, the temperatures of the vaporizer and ion tube, and the potential gradient at the end of the ion tube.

2.5 Quadrupole transmission

While chemical ionization provides a clean spectrum with little fragmentation, it also yields abundant parent ion signals for large molecular weight organics. This may be an issue if the quadrupole voltage settings are not tuned properly because improper tuning will lead to transmission biases through the quadrupole [28, 29]. In general, smaller ions are transmitted with higher yield than larger ions because they have a smaller resonance time in the quadrupole, but this can be compensated for by adjusting a few voltage settings. It should be noted that this issue is not specific for this chemical ionization system, but a general issue for all quadrupole mass spectrometers. It has been dealt with in other publications [28, 29], and I will only briefly deal with the relevant settings for obtaining uniform transmission across the mass range.

The setting that has the largest effect on ion transmission through the quadrupole is the total ion energy, i.e. the difference between the pole bias potential and the potential where the ions are "born". Ions with larger energy pass through the quadrupole more quickly ($E = \frac{1}{2}mv^2$), experience fewer RF cycles, and are therefore transmitted more efficiently. However, when ions experience fewer RF cycles, the resolution is decreased, so as always, there is a trade-off between resolution and signal. The important thing to

note is that larger ions need a larger energy to maintain the same resonance time (i.e. velocity) as smaller ions, and probably the single most important setting in the quadrupole for uniform transmission is the ion energy (pole bias). In the Merlin software, this setting can be mass programmed so that larger ions have more energy.

The second setting that warrants comment is the resolution which can also be mass programmed to achieve more uniform transmission. The "delta res" setting in the Merlin software includes some mass discrimination, but the specific function of this setting is unknown to me. In practice, I have simply adjusted it to get better signal. The other tune settings do not affect the mass discrimination significantly, but they are important in obtaining well resolved, abundant ion signal.

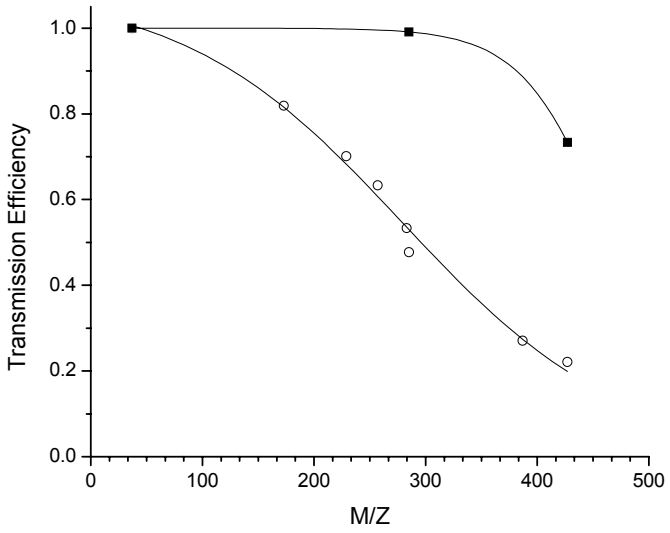

Figure 2.11. Quadrupole transmission efficiency relative to m/z = 37. A smaller pole bias (open circles) passes the larger molecular weight species less efficiently than a large pole bias (closed squares). Lines are drawn to guide the eye.

As an example of the importance of pole bias and resolution settings, Figure 2.11 shows the transmission efficiency relative to m/z = 37 as a function of m/z for two

different tune settings. Transmission efficiencies were determined by measuring the signal rise in an organic peak ($\Delta S_{m/z=[M+H]^+}$) and the depletion of m/z = 37 ($\Delta S_{m/z=37}$) for varying amounts of organic. The slope of a plot of $\Delta S_{m/z=37}$ vs $\Delta S_{m/z=[M+H]^+}$ (data not shown) gives the transmission efficiency. These tune settings differ predominately in the pole bias and resolution for large molecular weight ions. For poorly tuned transmission, ions with large molecular weight (m/z > 400 amu) are passed with 20% efficiency relative to m/z = 37. After proper tuning, large ions are passed with 75% efficiency.

2.6 Particle generation

Particle generation techniques vary, but they can be broken down into two broad categories: techniques that do or do not use organic solvents. Organic solvents, while convenient for generating particles, may cause problems in experiments when a portion of the solvent remains in the particles [30, 31]. Additionally, with A-CIMS, the solvent generally dominates the mass spectrum and the ion chemistry is no longer controllable. For these two reasons, particles here are generated without the aid of organic solvents by either direct nebulization of the pure organic, homogenous nucleation, or heterogeneous nucleation on seed particles.

Particle output from a nebulizer is extremely high for A-CIMS, and if not significantly diluted, depletes the primary ion. Additionally, the aerosol has a polydisperse size distribution which complicates kinetic analysis. In order to circumvent one or both of these problems, one of two solutions is used. First, particles are nebulized directly into a 500 mL flask and stored. The stored particles are then swept out with a small flow of N_2 (10 sccm) to the flow tube for the experiment. Since the particle

generation is not continuous, this technique provides a decaying particle signal, but sufficient signal is maintained for more than 30 minutes (long enough for an experiment). Second, particles are continuously generated using the nebulizer, and part of the flow is dumped to the exhaust and the remaining 0.2 slpm particle flow is sent to a differential mobility analyzer (DMA model 3080, TSI inc.) for particle selection. The DMA separates particles based on their size, so a monodisperse particle distribution is generated this way using the nebulizer. Unfortunately, the DMA also passes particles of a larger size that have 2 or 3 charges on them, provided they are present, which complicates kinetic analysis. An impactor can be placed at the inlet to the DMA that removes particles over a certain cut point diameter, and the particle size distribution is measured by an aerodynamic particle sizer (APS model 3321, TSI inc.) to ensure that doubly charged particles account for less than 5% of the mass weighted particle signal. This provides a stable, continuous source of monodisperse particles. However, the nebulizer does have a large aerosol output that can (and does) clog valves used to adjust the flow into the DMA, so shut-off valves that have a large opening instead of needle valves are used to prevent clogging. When using the DMA for this purpose, the sheath flow must be cleaned by passing through a -80ºC trap; otherwise, a large amount of ammonia contaminates the flow and the A-CIMS signal is dominated by NH_4^+ (m/z = 18).

Homogenous nucleation is a useful tool for generating polydisperse aerosol of organics that readily condense to form seed particles. This is especially useful when making internally mixed aerosol containing solid and liquid components because it eliminates the need for a solvent. Two reservoirs containing pure organics are heated

independently, and a small flow of N_2 (100 sccm) is passed through both. The flows are immediately mixed and sent into a heated tube to ensure mixing of the vapors. The flow is cooled back to room temperature generating internally mixed particles. This does make a polydisperse aerosol, so it is sent through the DMA to select out one particle size for experiments.

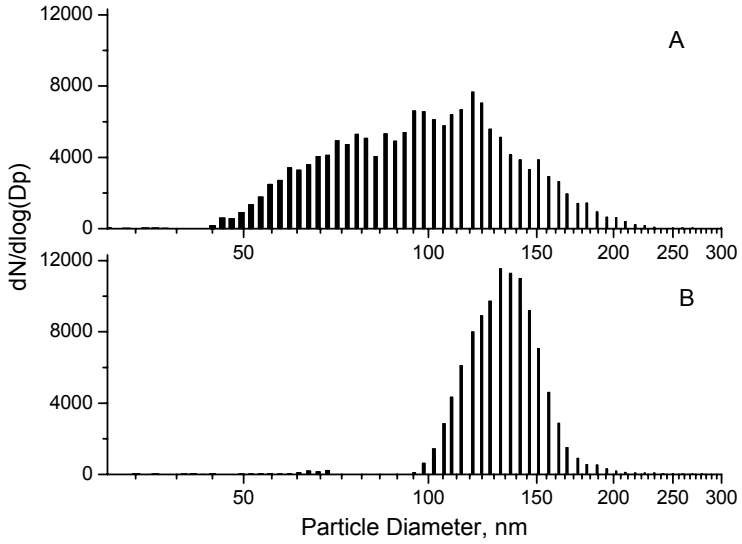

Figure 2.12. Particle size distributions using heterogeneous nucleation (A) without a second heating region and (B) with a second heating region. The geometric standard deviation is reduced from 1.44 to 1.23.

Heterogeneous nucleation is accomplished by first generating seed particles (< 10 nm diameter) by nebulizing distilled water and passing the aerosol through a diffusion drier (0.8 – 1.0 slpm) [32]. The seed particles are composed of impurities in the distilled water, and they are passed through a heated pickup cell containing an organic. The flow is then cooled and reheated to generate a monodisperse particle distribution with diameters between 100-300 nm. The purpose of the second heated region is to create a monodisperse size distribution. It is unclear how this works, but a polydisperse size

distribution is achieved in the absence of the second heater. Figure 2.12 shows size distributions of the generated aerosol with and without the second heater, and the geometric standard deviation is reduced from 1.44 to 1.23. Routinely, geometric standard deviations less than 1.2 (and as low as 1.12) are achieved with this technique.

2.7 Summary

In conclusion, we have adapted chemical ionization mass spectrometry to detect aerosol in real time. The low degree of fragmentation yields simplified spectra with most of the ion intensity in the parent ion of an organic molecule, and linear detection enables quantitative measurements to be made. The primary ion can be tailored to preferentially detect a species of interest which can help verify a specific assignment of a peak. A-CIMS, however, is not without limitation. The detection limit is not low enough to monitor ambient particle concentrations of species with low concentrations. Some particle components, however, exist at high concentrations such as ammonium sulfate (1-5 $\mu g/m^3$) for which A-CIMS may be useful for ambient measurements. Second, A-CIMS is truly an "aerosol" mass spectrometer because it detects both gas and condensed phase species. Additional work must be done to determine the fraction that a specific organic partitions to particles. Regardless of these limitations, A-CIMS is an excellent tool for studying heterogeneous reactions in the laboratory, and in the following chapters, I will demonstrate its usefulness through detailed study of ozone and radical initiated oxidation of organic aerosol.

References

1. Suess, D.T. and K.A. Prather, *Mass Spectrometry of Aerosols.* Chemical Reviews, 1999. **99**: p. 3007-3035.

2. Noble, C.A. and K.A. Prather, *Real-time single particle mass spectrometry: A historical review of a quarter century of the chemical analysis of aerosols.* Mass Spectrometry Reviews, 2000. **19**: p. 248-274.

3. Walker, J.T., et al., *Inorganic PM2.5 at a US agricultural site.* Environmental Pollution, 2006. **139**(2): p. 258-271.

4. Tobias, H.J. and P.J. Ziemann, *Compound identification in organic aerosols using temperature-programmed thermal desorption particle beam mass spectrometry.* Analytical Chemistry, 1999. **71**(16): p. 3428-3435.

5. Hearn, J.D. and G.D. Smith, *A chemical ionization mass spectrometry method for the online analysis of organic aerosols.* Analytical Chemistry, 2004. **76**(10): p. 2820-2826.

6. Warscheid, B. and T. Hoffmann, *On-line measurements of a-pinene ozonolysis products using an atmospheric pressure chemical ionisation ion-trap mass spectrometer.* Atmospheric Environment, 2001. **35**(16): p. 2927-2940.

7. Jayne, J.T., et al., *Development of an aerosol mass spectrometer for size and composition analysis of submicron particles.* Aerosol Science and Technology, 2000. **33**(1-2): p. 49-70.

8. Morrical, B.D., D.P. Fergenson, and K.A. Prather, *Coupling two-step laser desorption/ionization with aerosol time-of-flight mass spectrometry for the analysis of individual organic particles.* Journal of the American Society for Mass Spectrometry, 1998. **9**(10): p. 1068-1073.

9. Sykes, D.C., et al., *Thermal Vaporization-Vacuum Ultraviolet Laser Ionization Time-of-Flight Mass Spectrometry of Single Aerosol Particles.* Analytical Chemistry, 2002. **74**: p. 2048-2052.

10. McLafferty, F.W. and F. Turecek, *Interpretation of mass spectra*. 4 ed. 1993, Sausalito, CA: University Science Books.

11. Smith, G.D., et al., *Reactive uptake of ozone by oleic acid aerosol particles: Application of single-particle mass spectrometry to heterogeneous reaction kinetics.* Journal of Physical Chemistry A, 2002. **106**(35): p. 8085-8095.

12. Gard, E., et al., *Real-time analysis of individual atmospheric aerosol particles: Design and performance of a portable ATOFMS.* Analytical Chemistry, 1997. **69**(20): p. 4083-4091.

13. LaFranchi, B.W., J. Zahardis, and G.A. Petrucci, *Photoelectron resonance capture ionization mass spectrometry: a soft ionization source for mass spectrometry of particle-phase organic compounds.* Rapid Communications in Mass Spectrometry, 2004. **18**(21): p. 2517-2521.

14. LaFranchi, B.W. and G.A. Petrucci, *Photoelectron resonance capture ionization (PERCI): A novel technique for the soft-ionization of organic compounds.* Journal of the American Society for Mass Spectrometry, 2004. **15**(3): p. 424-430.

15. Munson, M.S.B. and F.H. Field, *Chemical Ionization Mass Spectrometry .I. General Introduction.* Journal of the American Chemical Society, 1966. **88**(12): p. 2621-&.

16. Warscheid, B., U. Kuckelmann, and T. Hoffmann, *Direct quantitative analysis of organic compounds in the gas and particle phase using a modified atmospheric pressure chemical ionization source in combination with ion trap mass spectrometry.* Analytical Chemistry, 2003. **75**(6): p. 1410-1417.

17. Hoffmann, T., et al., *On-line characterization of gaseous and particulate organic analytes using atmospheric pressure chemical ionization mass spectrometry.* Spectrochimica Acta Part B-Atomic Spectroscopy, 2002. **57**(10): p. 1635-1647.

18. Warscheid, B. and T. Hoffmann, *Structural elucidation of monoterpene oxidation products by ion trap fragmentation using on-line atmospheric pressure chemical ionisation mass spectrometry in the negative ion mode.* Rapid Communications in Mass Spectrometry, 2001. **15**(23): p. 2259-2272.

19. Zhao, J. and R.Y. Zhang, *Proton transfer reaction rate constants between hydronium ion (H3O(+)) and volatile organic compounds.* Atmospheric Environment, 2004. **38**(14): p. 2177-2185.

20. Houston, P.L., *Chemical Kinetics and Reaction Dynamics*. 1 ed. 2001, New York, NY: McGraw-Hill.

21. Geller, M.D., et al., *A new compact aerosol concentrator for use in conjunction with low flow-rate continuous aerosol instrumentation.* Journal of Aerosol Science, 2005. **36**(8): p. 1006-1022.

22. Stein, S.E., *Mass Spectra*, in *NIST Chemistry WebBook, NIST Standard Reference Database Number 69*, P.J. Linstrom and W.G. Mallard, Editors. 2005, National Institute of Standards and Technology: Gaithersburg MD, 20899.

23. Atkinson, R., et al., *Evaluated Kinetic and Photochemical Data for Atmospheric Chemistry .3. Iupac Subcommittee on Gas Kinetic Data Evaluation for Atmospheric Chemistry.* Journal of Physical and Chemical Reference Data, 1989. **18**(2): p. 881-1097.

24. Thornberry, T. and J.P.D. Abbatt, *Heterogeneous reaction of ozone with liquid unsaturated fatty acids: detailed kinetics and gas-phase product studies.* Phys. Chem. Chem. Phys., 2004. **6**: p. 84-93.

25. Katrib, Y., et al., *Products and mechanisms of ozone reactions with oleic acid for aerosol particles having core-shell morphologies.* Journal of Physical Chemistry A, 2004. **108**(32): p. 6686-6695.

26. Hearn, J.D. and G.D. Smith, *Kinetics and product studies for ozonolysis reactions of organic particles using aerosol CIMS.* Journal of Physical Chemistry A, 2004. **108**(45): p. 10019-10029.

27. Zahardis, J. and G.A. Petrucci, *The oleic acid-ozone heterogeneous reaction system: products, kinetics, secondary chemistry, and atmospheric implications of a model system – a review.* Atmospheric Chemistry and Physics, 2006. **6**(6): p. 11093-11179.

28. Wood, K.V., A.H. Grange, and J.W. Taylor, *Mass Discrimination Effects in a Quadrupole Mass-Spectrometer.* Analytical Chemistry, 1978. **50**(12): p. 1652-1654.

29. Wojcik, L. and K. Bederski, *Determination of the ion transmission coefficient for a mass spectrometer with a quadrupole ion analyzer.* International Journal of Mass Spectrometry and Ion Processes, 1996. **153**(2-3): p. 139-144.

30. Asad, A., B.T. Mmereki, and D.J. Donaldson, *Enhanced uptake of water by oxidatively processed oleic acid.* Atmospheric Chemistry and Physics, 2004. **4**(8): p. 2083-2089.

31. Broekhuizen, K.E., et al., *Formation of cloud condensation nuclei by oxidative processing: Unsaturated fatty acids.* Journal of Geophysical Research-Atmospheres, 2004. **109**(D24): p. -.

32. Peters, C. and J. Altmann, *Monodisperse Aerosol Generation with Rapid Adjustable Particle-Size for Inhalation Studies.* Journal of Aerosol Medicine-Deposition Clearance and Effects in the Lung, 1993. **6**(4): p. 307-315.

CHAPTER 3

HETEROGENEOUS OXIDATION OF UNSATURATED ORGANICS WITH O_3[1,2,3]

3.1 Introduction

A-CIMS is a useful tool for detecting organic aerosol in real time, and because it has a linear response to concentration it can be used for quantitative measurements [1, 2]. In order to verify that A-CIMS can be used to investigate heterogeneous chemical reactions, we monitored the reaction between O_3 and particles composed of oleic acid (OL), methyl oleate (MO), linoleic acid (LO), 1-octadecene (OD), and oleyl alcohol (OLA). In particular, the reaction between OL and O_3 has been the focus of many recent studies [3-15], so it serves as a good benchmark to test the capabilities of A-CIMS and ensure that it gives the "right" answer. For this reason OL ozonolysis will be the focus of this chapter with some less detailed remarks of the other unsaturated organics. I will first provide some motivation for studying OL ozonolysis and some background of heterogeneous reaction kinetics.

---

[1] Hearn, J.D. and G.D. Smith, *Kinetics and product studies for ozonolysis reactions of organic particles using aerosol CIMS.* Journal of Physical Chemistry A, 2004. **108**(45): p. 10019-10029. Copyright 2004 American Chemical Society. Reproduced in part with permission by the publisher.

[2] Hearn, J.D., A.J. Lovett, and G.D. Smith, *Ozonolysis of oleic acid particles: evidence for a surface reaction and secondary reactions involving Criegee intermediates.* Physical Chemistry Chemical Physics, 2005. **7**(3): p. 501-511. Reproduced in part with permission by the publisher.

[3] Hearn, J.D. and G.D. Smith, *Measuring rates of reaction in supercooled organic particles with implications for atmospheric aerosol.* Physical Chemistry Chemical Physics, 2005. **7**(13): p. 2549-2551. Reproduced in part with permission by the publisher.

3.1.1 Background of OL ozonolysis

Oleic acid (OL) is an 18 carbon-length carboxylic acid with a double bond between carbons 9 and 10. It has a very low vapor pressure (1 Torr at 176.5ºC) [16] and exists in the liquid phase at room temperature. It reacts readily with ozone because of the double bond, and it can easily be made into liquid particles through a variety of techniques. OL is also found on ambient particles and is sourced primarily from cooking emissions [17], but it has also been found in automobile and diesel exhaust [18], wood smoke [19], and cigarette smoke [20]. For these reasons, it makes a convenient and relevant reaction to study in the laboratory. When ozone reacts with an alkene, it adds across the double bond forming what is called the primary ozonide (see Figure 3.1) [21, 22]. This is highly unstable and decomposes rapidly to form an aldehyde and an excited Criegee Intermediate (ECI). In gas phase reactions the ECI can decompose or become collisionally stabilized [23, 24]. However, in heterogeneous reactions, the ECI is quickly stabilized from the frequent collisions it encounters in the condensed phase, so decomposition is expected to be a minor channel. The stabilized Criegee intermediate (SCI) is still very reactive and can be involved in a number of reactions [25-28], complicating the distribution of expected products. It can recombine with the aldehyde to form a secondary ozonide or a peroxide oligomer [29] which are stable at room temperature but would probably not survive the elevated temperature of the vaporizer [30]. The SCI can also react with another SCI to form two aldehydes and O_2 [31]. It can react with carboxylic acid functional groups to form an α-acyloxyalkyl hydroperoxide [29], and it has been recently proposed to react with carbon-carbon double bonds [9].

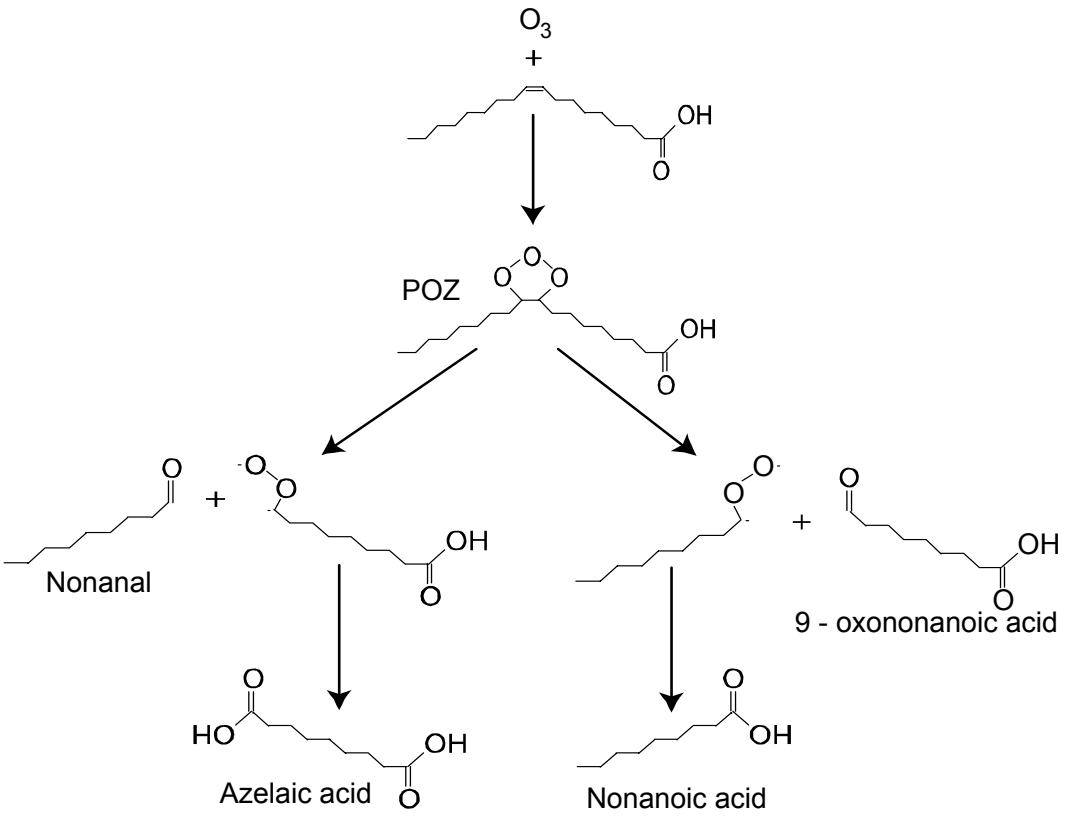

Figure 3.1. Reaction mechanism for ozonolysis of oleic acid. The primary ozonide (POZ) rapidly decomposes into an aldehyde and a Criegee biradical intermediate that can rearrange to yield carboxylic acids.

These last two pathways, if large enough, can affect the kinetics of an acidic condensed phase reactant (such as OL), so it is important to understand and account for this secondary chemistry when making kinetic measurements. Measurements of OL ozonolysis have been made both from monitoring the gas phase loss of ozone on an OL coated surface [3, 5, 10] and loss of OL in particles where ozone is in excess [8, 11-14, 32]. The "ozone loss" measurements can be taken at face value because the loss of ozone is unaffected by the secondary chemistry. These measurements report an uptake coefficient (the rate of loss of ozone normalized to the gas-surface collisions) of ca. 8×10^{-4} [3, 5]. The "OL loss" measurements report a higher uptake coefficient of $(1 - 7.3) \times$

10^{-3} [12, 14] suggesting that there are additional loss processes for OL that are not accounted for.

Despite this apparent discrepancy, this reaction provides the best studied benchmark for verifying A-CIMS as a tool for measuring heterogeneous reaction kinetics. The results discussed in this chapter quantitatively explain the discrepancy between the aerosol and coated flow tube experiments. Secondary chemistry plays critical roles in both the kinetics of the reaction and the observed product distributions.

3.1.2 Heterogeneous Reaction Kinetics

Traditionally, heterogeneous reactions have been conceptualized by a kinetic "resistor" model in which the reaction is broken down into several individual steps [33, 34]. Each step has its own conductance (γ) where the inverse of the conductance is the resistance of that step ($1/\gamma$). The first step is gas transport to the surface (Γ_g), followed by mass accommodation (α), and finally, chemical reaction (Γ_{rxn}) competes with solubility (Γ_s). Alternatively, reaction can occur at the surface (Γ_{surf}) and bypass the accommodation and solubility steps. The conductances can be directly added together if the steps are in parallel (e.g. Γ_{rxn} and Γ_s) or their inverses can be summed if the steps are in series. If one step in a series has a high resistance (low conductance) compared to the other steps, it is the rate limiting step and all the others can be ignored. Equation (3.1) shows the relationship between what is measured and the individual steps of the reaction. In the case of OL ozonolysis, the uptake coefficient is limited by the chemical reaction since gas phase diffusion is fast ($\Gamma_g \approx 0.45$) and ozone solubility is insignificant after 10 msec ($\Gamma_s \approx 1.5 \times 10^{-5}$) [33]. For additional reading see these references [33, 34].

$$\frac{1}{\gamma_{obs}} = \frac{1}{\Gamma_g} + \left\{ \left(\frac{1}{\alpha} + \frac{1}{\Gamma_{rxn} + \Gamma_s} \right)^{-1} + \Gamma_{surf} \right\}^{-1} \approx \frac{1}{\Gamma_{rxn}} \tag{3.1}$$

The most straightforward way of measuring the gas phase uptake coefficient is to monitor the concentration of gas phase reactant as a function of gas-surface collisions. This is convenient because there is a straightforward relationship between reactant concentration and time (i.e. number of collisions). However, gas phase measurements are blind to the chemistry in the particles, and A-CIMS is designed for aerosol detection. The loss of condensed phase species can be related to the uptake coefficient by equating the loss of O_3 to the loss of OL in Equation (3.2) where [OL] is the concentration of oleic acid, γ is the uptake coefficient, $[O_3]$ is the gas phase ozone concentration, $\bar{c}$ is the mean speed of ozone ($\bar{c}$ = 362 m/sec), R is the gas constant (R = 0.082 atm K^{-1} M^{-1}), T is the temperature (T = 293 K), a is the particle radius, and φ is the "reaction yield" [14, 35]. The reaction yield (φ) accounts for secondary losses to OL in addition to the reaction with ozone, so if there are no additional losses, $\varphi = 1$. The measured uptake coefficient is the product of γ and φ, so in order to simplify the discussion I am going to use γ_{OL} to represent the "OL uptake coefficient" (the product of γ and φ).

$$\frac{d[OL]/[OL]_0}{dt} = -(\gamma \times \varphi)\left(\frac{[O_3]\bar{c}}{4RT} \right) \frac{3}{a} \left(\frac{1}{[OL]_0} \right) \tag{3.2}$$

In Equation (3.2), γ and φ are both functions of [OL], and the normalized rate of loss of OL is dependent on the particle radius. An exact analytical solution cannot be obtained for Equation (3.2), but since $\gamma_{obs} \approx \Gamma_{rxn}$ or Γ_{surf}, approximate solutions can be obtained for a bulk reaction near the surface (Equation (3.3)) and a surface reaction (Equation (3.4)).

$$\frac{[OL]}{[OL]_0} = \left(1 - \frac{3[O_3]\gamma_{OL}\bar{c}}{8RTa[OL]_0}t\right)^2 \tag{3.3}$$

$$\frac{[OL]}{[OL]_0} = e^{\left(-\frac{3[O_3]\gamma_{OL}\bar{c}}{4aRT[OL]_0}t\right)} \tag{3.4}$$

The only difference in these two approximations is that the normalized rate of loss follows quadratic and exponential functions, respectively. Distinguishing between a quadratic and exponential function is not feasible when secondary chemistry is important or when other physical properties change during the reaction such as solubility and diffusion. The data collected with a monodisperse aerosol is fit with both functions, and the better fit is used as a measure of the initial rate of reaction.

3.2 Experimental Set-up

Polydisperse aerosol was generated by nebulizing pure OL into a 500 mL flask and stored as described in section 2.6. Monodisperse aerosol was generated as described in section 2.6 by selecting a particle size from a continuously nebulized aerosol. Figure 3.2 shows a schematic of the flow tube reactor where the particle flow (200 sccm) was sent through an injector and entrained in a 2 slpm flow of N_2 carrying O_3 ($\approx 2\times10^{15}$ molecules/cm^3, 10^{-4} atm). The particles remained on-axis for the length of the flow tube which was verified by eye with light scattering from a green diode laser and a constant signal on the mass spectrometer as the injector was pulled back. In order to determine the reaction time, the particles were introduced through the injector, and the time of the particle front arrival was measured by light scattering at different positions along the flow tube reactor. For the polydisperse measurements, the particle velocity was 15.5 cm/sec. This is in good agreement with the calculated laminar flow (Re ≈ 60) velocity at the

center of the flow tube under these flow conditions (14.5 cm/sec.). For kinetic measurements of monodisperse particles, the measured particle velocity was slightly higher (v = 18 cm/sec.).

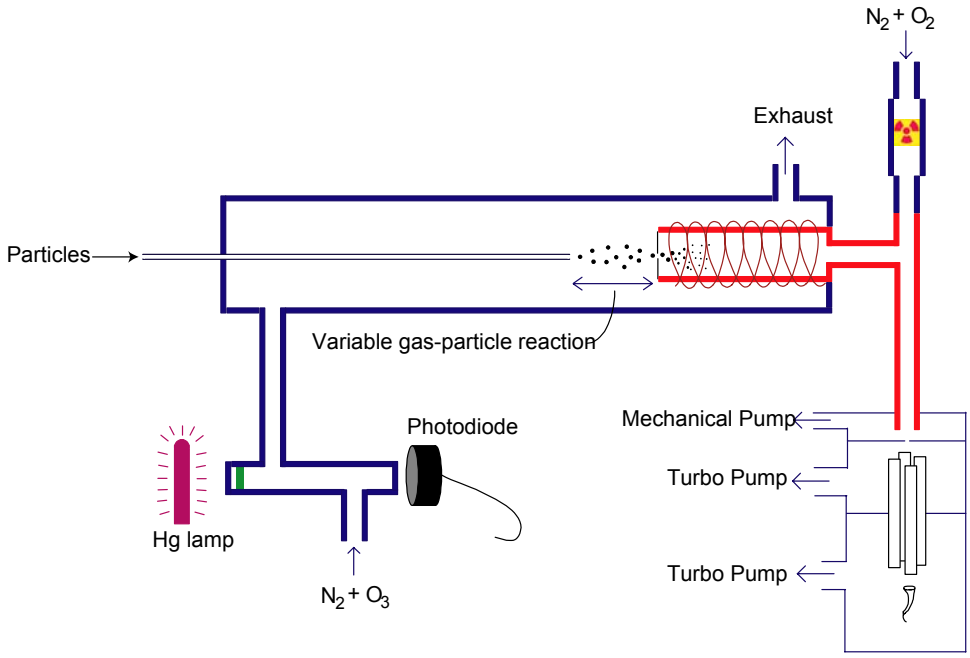

Figure 3.2. Schematic of the aerosol flow tube reactor.

In a laminar flow reactor mixing relies on gas diffusion instead of turbulence which lowers the effective reaction time in the flow tube. At atmospheric pressure we calculate a time of 0.4 seconds for O_3 to diffuse to the center of the injector flow. In order to verify this, we measured the reaction between OL and O_3 at 4 different O_3 concentrations. The exposure is the product of $[O_3]$ and time, so according to equation (3.5), two different O_3 pressures can be used to determine τ. Full reaction decays were measured at four different $[O_3]$, and τ was adjusted to achieve the best exponential fit (i.e. highest R^2). Figure 3.3 shows the results from this experiment, and it is clear that with τ = 0 seconds, the higher $[O_3]$ are systematically shifted to the right of the curve (panel A).

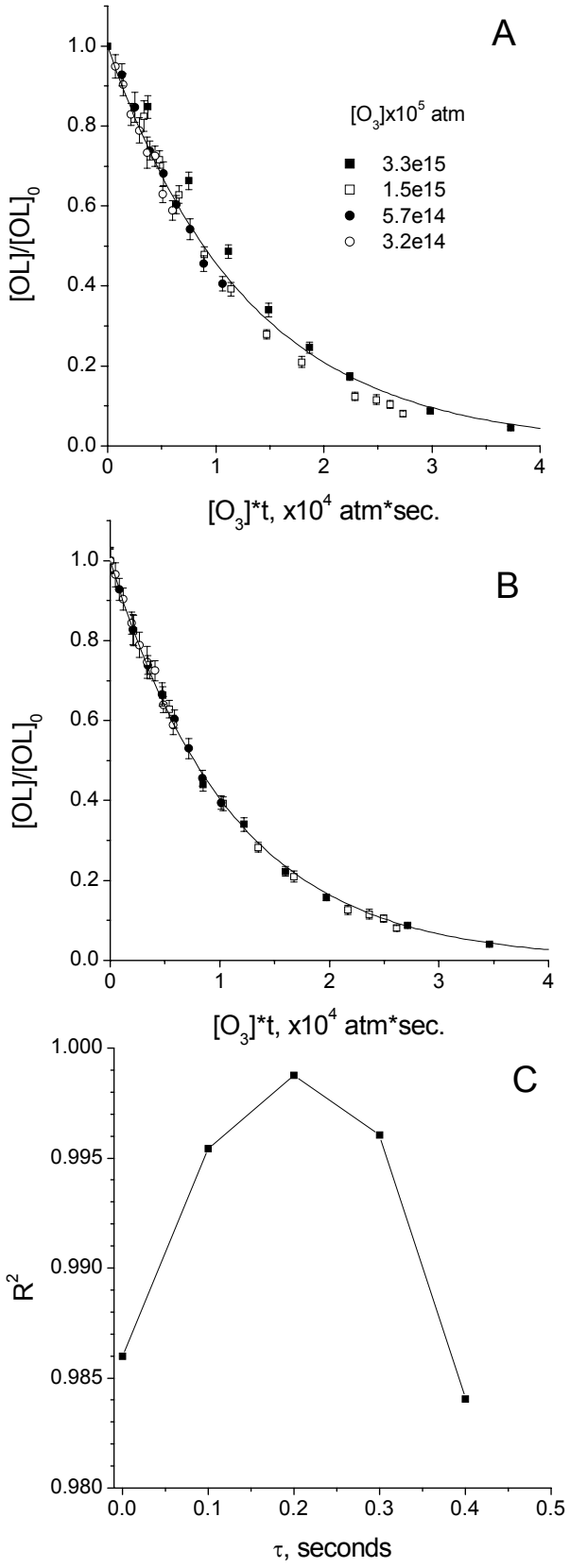
A
[O3]x10^5 atm
3.3e15
1.5e15
5.7e14
3.2e14
[OL]/[OL]0
[O3]*t, x10^4 atm*sec.
B
[OL]/[OL]0
[O3]*t, x10^4 atm*sec.
C
R^2
τ, seconds

Figure 3.3. Reaction of OL particles with different concentrations of O_3 to determine τ (the mixing time). (A) OL reaction with $\tau = 0$ seconds shows a systematic shift in the high O_3 pressure data (closed squares) to the right. (B) OL reaction with $\tau = 0.2$ seconds shows much less scatter in the data. (C) R^2 values for exponential fits as a function of τ, and $\tau = 0.2$ seconds is the approximate mixing time in the flow tube. Lines in (A) and (B) show first order exponential fits to the data.

With $\tau = 0.2$ seconds, the data for the different $[O_3]$ show much better overlap (panel B), and as shown in panel C, $\tau = 0.2$ seconds yields the best fit ($R^2 = 0.999$). The results presented here are corrected for the mixing time ($\tau = 0.2$ seconds), and this is in good agreement with the calculated time (0.4 seconds) and the mixing time estimated by Morris et al. [12].

$$\text{Exposure} = [O_3]_A \times (t_A - \tau) = [O_3]_B \times (t_B - \tau) \tag{3.5}$$

Since A-CIMS uses a relatively high pressure (40 Torr) for vaporization and ionization of aerosol components, there is potential for additional reaction between O_3 and the particle constituents. In fact, we observe a significant depletion ($\approx 50\%$) of the organic upon addition of O_3 when the injector is pushed in. Part of this depletion is due to decreased sensitivity when O_3 is present, but some of the decrease is most likely due to chemical reaction. Since this is a gas phase reaction in the vaporizer and ion tube and O_3 is in excess, it is a pseudo-first order reaction that removes a constant fraction of the organic aerosol vapor [36]. Normalizing the unreacted signal (injector pushed in) to a reacted signal (injector pulled back) conveniently cancels out the gas phase reaction. Equation (3.6) demonstrates this where $[OA]_0$ is the organic aerosol concentration before adding O_3, k is the second order rate constant for the gas phase reaction, t is the resonance time in the vaporizer and ion tube, c is a constant describing the heterogeneous reaction rate, and t_{FT} is the resonance time in the flow tube. When this equation is

normalized to the pushed in position (t_{FT} = 0 seconds), the gas phase component is removed.

$$[OA]_{t_{FT}} = [OA]_0 e^{-k[O_3]t}\left(1 - ct_{FT}\right)^2 \tag{3.6}$$

For the experiments described in this chapter, the ionization tube was a ¼ inch o.d. stainless steel tube wrapped with heating tape. Although the small ion tube yielded low sensitivity, the aerosol concentration was high enough to maintain sufficient signal to measure reaction kinetics. For the polydisperse measurements, the vaporizer had a flow limiting orifice, whereas the monodisperse measurements employed a capillary inlet. Gases used were purchased from National Welders and used without further purification: N_2 (99.99%), O_2 for ion tube flow (99.5%), O_2 for O_3 generation (99.99%). O_3 was made with a commercial O_3 generator (model L11, Pacific Ozone Technology) and stored on silica gel at -80ºC. O_3 was measured using Beer's law absorption at 254 nm in a 10 cm path length cell (σ = 1.159 $\times 10^{-17}$ cm^{-2} $molecule^{-1}$). Chemicals were purchased from Aldrich and used without further purification: oleic acid (*cis*-9-octadecenoic acid, 90% and 99%), methyl oleate (*cis*-9-octadecenoic acid methyl ester, 99%), myristic acid (n-tetradecanoic acid, 99%), lauric acid (n-dodecanoic acid, 99%), oleyl alcohol (cis-9-octadecen-1-ol, 85%), linoleic acid (cis-9, cis-12-octadecedienoic acid, 95%), and 1-octadecene (97%). There was no observable difference between the 90% and 99% purities of oleic acid, and most of the data presented here uses the 90% stock.

3.3 Heterogeneous reaction kinetics: polydisperse aerosol

As mentioned in section 3.1.2, heterogeneous reaction kinetics are dependent on the size of the particle, so for simple analysis, the reaction would be done with a monodisperse aerosol. However, in the absence of expensive equipment to generate or

select a monodisperse particle distribution the kinetics of a heterogeneous reaction can, in principle, be de-convolved from a polydisperse aerosol if the size distribution and size dependence on the kinetics are known. For the analysis of the experiments in this section, I will assume that the reaction occurs in the bulk (Equation (3.3), quadratic function) [12].

Figure 3.4 shows raw data collected during the reaction of ozone with OL particles (geometric mean ≈ 800 nm diameter). The integrated signal at m/z = 283 is plotted as a function of time, and the injector was pulled back to various injector positions to achieve different ozone exposures. Between each reaction measurement, the injector was pushed in to measure the unreacted OL signal since the particle signal was naturally decaying away. The fractional amount of OL remaining was calculated by normalizing the reacted signal to the average of the unreacted particle signal before and after the measurement, and Figure 3.5 shows the normalized signal as a function of O_3 exposure.

In addition to the A-CIMS measurements, the particle size distribution was measured before and after the experiment to account for drifts, and Figure 3.6 shows size measurements for the data shown in Figure 3.5 before (solid line) and after (dashed line) the experiment. Initially, the size distribution is bimodal with a significant contribution to the signal from 2 μm diameter particles. After the experiment, the second mode is mostly gone with only a shoulder remaining on the lower mode around 1 μm diameter. The line in Figure 3.5 shows the fit to the data. A quadratic function could not be used to fit the data directly since the size distribution was polydisperse (geometric standard deviation > 1.2). In order to fit the data, the mass weighted sum of decays for binned

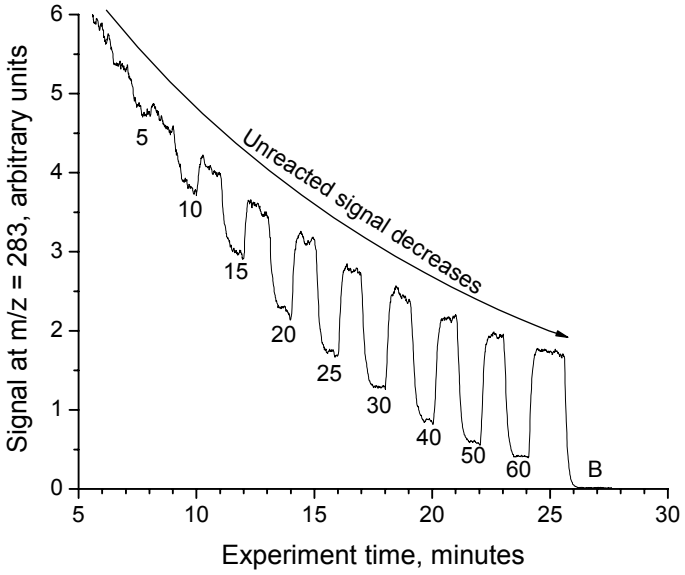

Figure 3.4. Raw ion signal for OL particles during an ozonolysis reaction. Numbers on the graph indicate the reaction distance in cm, and a no reaction point is taken between each measurement for normalization. Note the decaying unreacted particle signal as the aerosol concentration in the flask decreases.

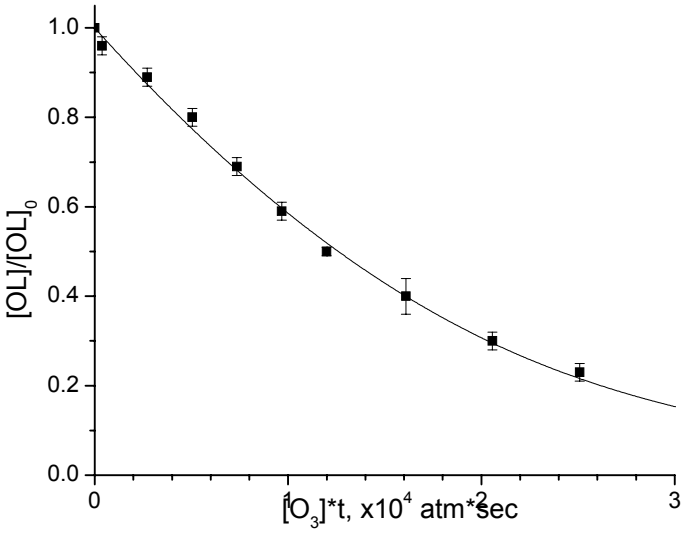

Figure 3.5. Reaction of polydisperse OL particles with O_3. The line represents the best fit to the data and it yields uptake coefficients of 8×10^{-4} and 7×10^{-4} for the size data collected before and after the experiment, respectively. Error bars represent the standard deviation of the A-CIMS measurement.

particle sizes for a given γ_{OL} was compared to the data, and γ_{OL} was adjusted to obtain the best fit. Appendix 1 shows the algorithm that calculates this best fit, and the best fits for the data in Figure 3.5 yield $\gamma_{OL} = 8\times10^{-4}$ and 7×10^{-4} for the size data measured before and after the experiment, respectively.

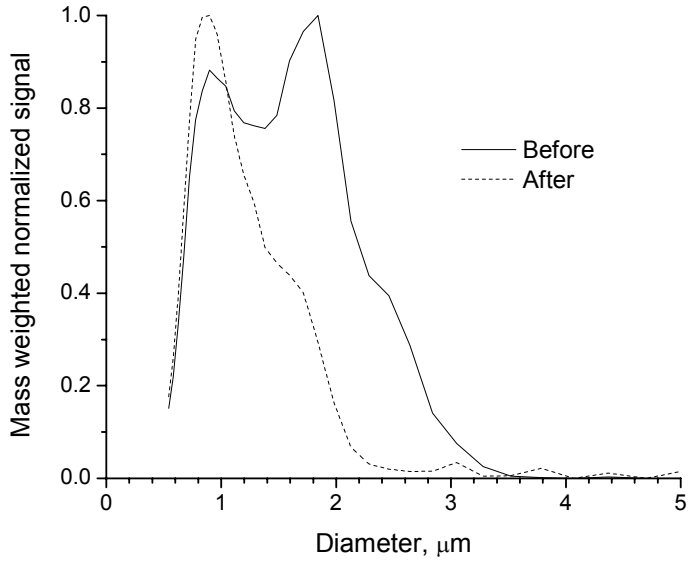

Figure 3.6. Normalized, mass weighted size distribution measured before (solid line) and after (dashed line) an experiment. The distribution shifts to smaller particles since large particles have a faster settling velocity.

In an effort to better understand the kinetics and to verify that there is no size dependence on γ_{OL}, the size distribution was crudely changed to an average size of 1.2 and 1.4 μm diameter by generating the particles using homogenous nucleation. These larger particle sizes yielded the same γ_{OL} (7.2×10^{-4} and 7.3×10^{-4}, respectively) as 800 nm particles (7.5×10^{-4}) corroborating the approximation that the reaction is not limited by O_3 solubility (Γ_s). Unfortunately, the polydisperse size distribution makes a distinction between a quadratic and exponential function impractical, so at this point, it is unclear whether the reaction occurs at the surface or in the bulk.

In addition to the OL ozonolysis reaction, we used A-CIMS to measure kinetics of the reaction of ozone with linoleic acid (LO), oleyl alcohol (OLA), and 1-octadecene (OD). The results are shown in Table 3.1 for all the organics studied as well as results from other studies. Our results show that O_3 reacts most quickly with LO, which is thought to be because it has two double bonds and therefore has a higher probability of reaction with O_3. However, the bimolecular rate constants for the O_3 + LO and OL reactions are the same ($k_{LO} = 9.9\times10^5$ M^{-1} s^{-1} and $k_{OL} = 10.4\times10^5$ M^{-1} s^{-1}) [37], so solubility or O_3 diffusion might also be different between OL and LO. OL and OLA have the same uptake coefficient within our error bars, which is expected since they have such similar structures only differing in the terminal functional group (acid vs. alcohol). These functional groups must do little to affect the solubility and diffusion of ozone in the particles. OD has the lowest γ, which is expected since reactions in the gas phase involving molecules with terminal double bonds react much more slowly with O_3 than molecules with non-terminal double bonds [38].

Table 3.1. Uptake coefficients from this work and other recent studies. The other two Aerosol flow tube experiments report higher uptake coefficients than the coated flow tube studies.

	Aerosol Flow tube (aerosol loss)			Coated flow tube (O_3 loss)	
	Hearn and Smith	Morris et al.	Smith et al.	Moise and Rudich	Thornberry and Abbatt
OL	$(7.5 \pm 1.2)\times10^{-4}$	$(1.6 \pm 0.2)\times10^{-3}$	$(1.0 - 7.3)\times10^{-3}$	$(8.3 \pm 0.2)\times10^{-4}$	$(8.0 \pm 1.0)\times10^{-4}$
LO	$(1.1 \pm 0.2)\times10^{-3}$			$(1.2 \pm 0.2)\times10^{-3}$	$(1.3 \pm 0.1)\times10^{-3}$
OLA	$(7.5 \pm 1.3)\times10^{-4}$				
OD	$(2.4 \pm 0.4)\times10^{-4}$				

Within the uncertainties of our measurements, the OL and LO uptake coefficients quantitatively agree with experiments that measured the loss of O_3 on coated surfaces, but

there is a significant discrepancy between our measurements and the other particle measurements. Morris et al. [12] and Smith et al. [14] both report larger uptake coefficients for O_3 on OL particles. In hindsight, the agreement with the coated flow tube measurements is probably fortuitous and caused by some sampling bias in the size measurements. For instance, the larger particles may have been lost to the walls when mixed with the large dilution flow of N_2 (5 slpm) during the size measurement. This would cause an artificially small γ to be calculated from the fit. In any case, the uptake kinetics are roughly the same as all the reported measurements ($\gamma \approx 10^{-3}$), and it is clear that A-CIMS can be used for kinetic measurements. As you will see in the next section, A-CIMS can do even better than this with a monodisperse particle source! A more complete discussion on the kinetics is saved for section 3.4.3.

3.4 Heterogeneous reaction kinetics: monodisperse aerosol

In order to obtain reliable kinetic measurements of heterogeneous reactions, an aerosol with a monodisperse size distribution ($\sigma_g < 1.2$) must be used. In the following sections, we examined the reactions between ozone and particles composed of OL, methyl oleate (MO), and mixtures of OL with MO, myristic acid (MA), and lauric acid (LA). The results show that the reaction between OL and O_3 is significantly affected by secondary chemistry, and that accounting for the secondary losses of OL quantitatively explains the discrepancies between coated flow tube and particle measurements of the OL + O_3 reaction (see Table 3.1).

3.4.1 O_3 uptake of pure particles

OL particles were generated using a continuous nebulizer flow, and one particle size was selected with a differential mobility analyzer (DMA model 3081, TSI inc.) as described in section 2.6. Figure 3.7A shows a reaction decay for 700 nm OL particles,

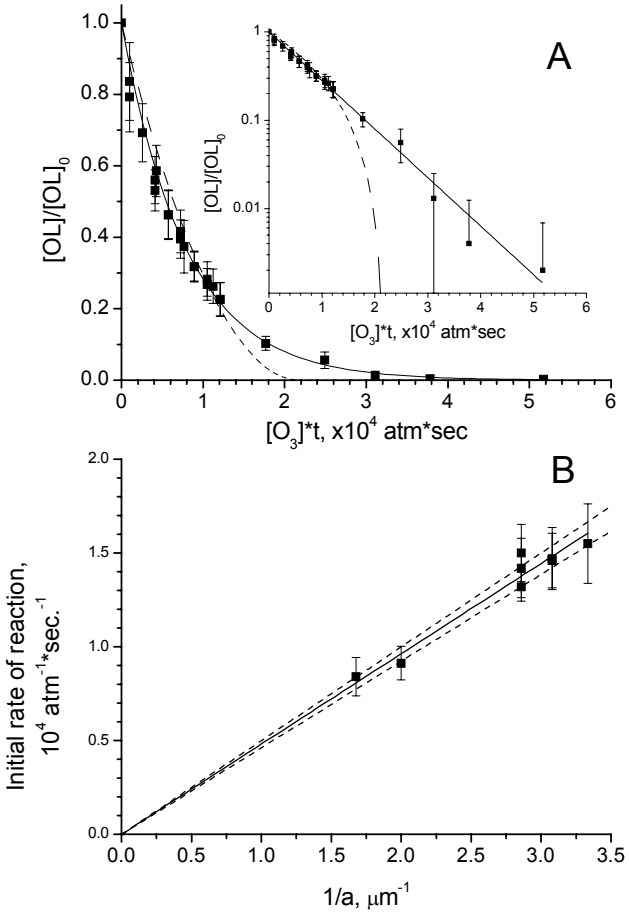

Figure 3.7. (A) Reaction of 700 nm OL particles with ozone. The solid line and dashed lines are fits to the data with exponential and quadratic functions, respectively. Both functions fit the data reasonably well, but the exponential fit gives a better overall fit suggesting that the reaction may occur at the surface. The inset illustrates the superior quality of an exponential fit to the data on a log scale. (B) Initial reaction slope as a function of particle radius. The solid line represents a linear fit to the data forcing a zero intercept, and the dashed lines represent the 95% confidence bands of this fit. Uptake coefficients calculated from this plot is $\gamma_{OL} = (1.38 \pm 0.06)\text{x}10^{-3}$. Error bars represent estimated uncertainties on the O_3 exposure.

and the solid and dashed lines represent fits to the data using exponential and quadratic functions, respectively. While the quadratic function fits the data to $[OL]/[OL]_0 = 0.2$, it overestimates the rate of reaction past this point, whereas the exponential function fits the data much better. The inset to Figure 3.7A illustrates the superior fit of an exponential function on a log scale. With the assumption that secondary chemistry and changes in physical properties of the particle are not changing, the exponential fit indicates that that the reaction is occurring at the surface, contradicting conclusions from other work (discussed in section 3.4.3). The reaction was done with several OL particle sizes (0.6 – 1.2 μm diameter), and the initial slope is plotted as a function of the size (1/a) in Figure 3.7B. The observed linear dependence of the initial slope on the inverse of particle radius (1/a) confirms that the reaction is occurring at or near the surface. The slope of the linear fit in Figure 3.7B yields $\gamma_{OL} = (1.38 \pm 0.06) \times 10^{-3}$. This is significantly higher than our measurements with a polydisperse size distribution and the coated flow tube measurements, but it is consistent with other particle measurements.

As mentioned above, SCIs formed from ozonolysis reactions can react with an acid moiety to form α-acyloxyalkyl hydroperoxides [29]. In order to measure the contribution of this secondary chemistry to the OL reaction, O_3 uptake on MO particles, the ester analogue to OL, was also measured. MO lacks an acidic proton and does not react with SCIs. Figure 3.8A shows the reaction decay for ozonolysis of MO particles (1.1 μm diameter) with quadratic (dashed line) and exponential (solid line) fits to the data. In contrast with OL particles, the quadratic function fits the MO data much better. The exponential function fits the data to $[MO]/[MO]_0 = 0.2$, but then it underestimates the reaction past this point. Additionally, there is a linear dependence between the inverse of

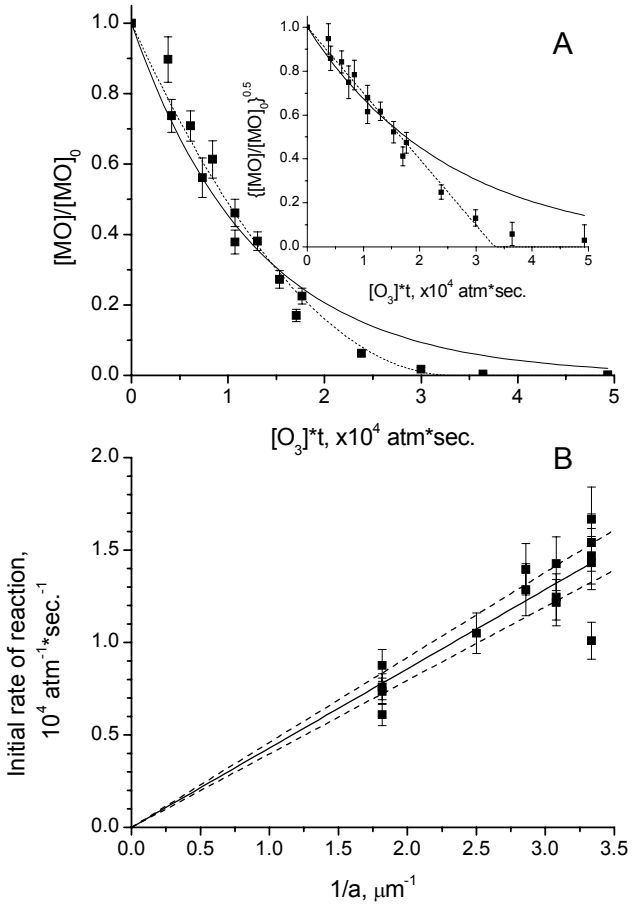

Figure 3.8. (A) Reaction of MO particles (1.1 μm diameter) with O_3. Lines represent fits to the data with exponential (solid) and quadratic (dashed) functions. The inset shows the same data on a quadratic y-scale. The exponential function underestimates the reaction below 0.2 whereas the quadratic function provides a much better fit to the data. (B) Initial reaction slope as a function of particle radius. The solid line represents a linear fit to the data forcing a zero intercept, and the dashed lines represent the 95% confidence bands of this fit. Uptake coefficients calculated from this plot is $\gamma_{MO} = (1.23 \pm 0.10)\text{x}10^{-3}$. Error bars represent estimated uncertainties on the O_3 exposure.

the particle radius (1/a) and the initial slope of the reaction. Both of these observations confirm that O_3 reacts with MO particles near the surface but in the bulk. The slope of the fit in Figure 3.8B yields $\gamma_{MO} = (1.23 \pm 0.10)\times 10^{-3}$, lower than γ_{OL}, but still higher than the coated flow tube measurements of OL ozonolysis [5, 39]. However, MO

particles may have different physical properties than OL particles such as ozone solubility or diffusion. Because of these possible differences, no direct comparison of these absolute measurements can be made to measure the contribution of secondary chemistry to OL loss.

3.4.2 Internally mixed particles

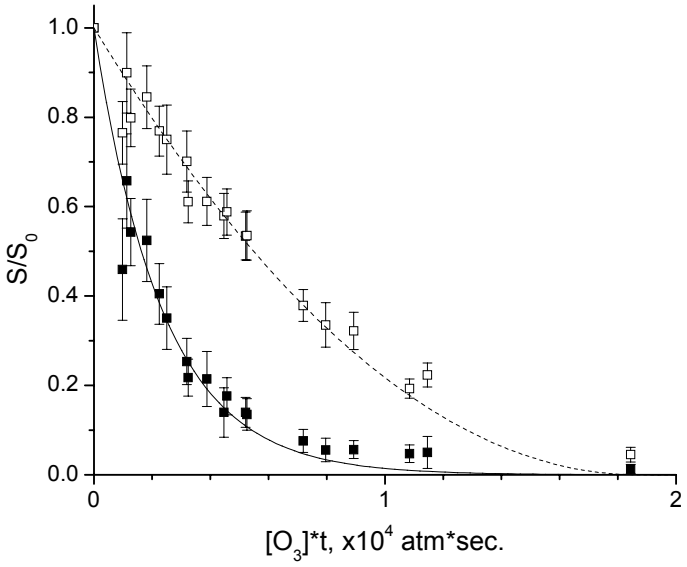

Figure 3.9. Reaction of particles composed of OL and MO (X_{OL} = 0.25) with O_3. OL (closed squares) reacts much faster than MO (open squares), consistent with a large SCI reaction with OL. Lines are fits to the data using exponential (solid) and quadratic (dashed) functions.

In order to quantitatively correct for the secondary chemistry involving the acid moiety of OL, properties such as O_3 solubility (H) and diffusion (D) must be accounted for. A convenient approach to making a more direct measurement on the secondary chemistry is to generate internally mixed particles containing OL and some other constituent that affects the SCI concentration. I have made two approaches to measuring the contribution of this secondary chemistry by either increasing or decreasing the

SCI/OL ratio. An increased SCI/OL ratio is achieved by making OL/MO particles where the MO maintains SCI production through reaction with O_3, and it simultaneously dilutes OL. A decreased SCI/OL ratio is obtained through OL/MA or OL/LA mixtures. The alkanoic acids react with SCIs, thus reducing their reaction with OL.

OL/MO particles were generated by nebulizing a known mixture of the two liquids and size selecting particles through the DMA. Figure 3.9 shows reaction decays for OL and MO in internally mixed particles (X_{OL} = 0.25). OL reacts much faster than MO, consistent with a large SCI reaction with the acidic proton. Since H and D are the same for MO and OL in internally mixed particles and the rate constants for the reactions between O_3 and both MO and OL are the same ($k_2 = 10^6$ M^{-1} s^{-1}) [37], the slopes of their reaction decays can be compared directly. The SCI contribution is determined by comparing the initial rates:

$$\frac{d[OL]/dt}{[OL]} = -k_2[O_3] - k_{SCI}[SCI] \tag{3.7}$$

$$\frac{d[MO]/dt}{[MO]} = -k_2[O_3] \tag{3.8}$$

and the ratio of these rates is:

$$1 + \frac{k_{SCI}[SCI]}{k_2[O_3]} \cong 1 + \left(\frac{k_{SCI}[SCI]_{pure}}{k_2[O_3]} \right) \frac{1}{X_{OL}} \tag{3.9}$$

In equation (3.9), [SCI] is approximated as $[SCI]_{pure}/X$, where $[SCI]_{pure}$ is the concentration of stabilized Criegee intermediate in pure OL particles and X_{OL} is the OL mole fraction. This assumption is valid since the SCI production is unaffected by X_{OL}, but the rate at which the SCI is consumed is proportional to X_{OL}. Equation (3.9) shows that a plot of the ratio of the initial rates vs. $1/X_{OL}$ should yield a linear plot where the

slope gives the overall ratio of the SCI and O_3 contributions to the OL ozonolysis reaction. Figure 3.10 shows a plot of the initial rate of reaction for OL and MO in the internally mixed particles, and the rate of OL loss increases at lower X_{OL}. The inset shows the ratio of their rates, and the line represents the linear fit to the data with a slope

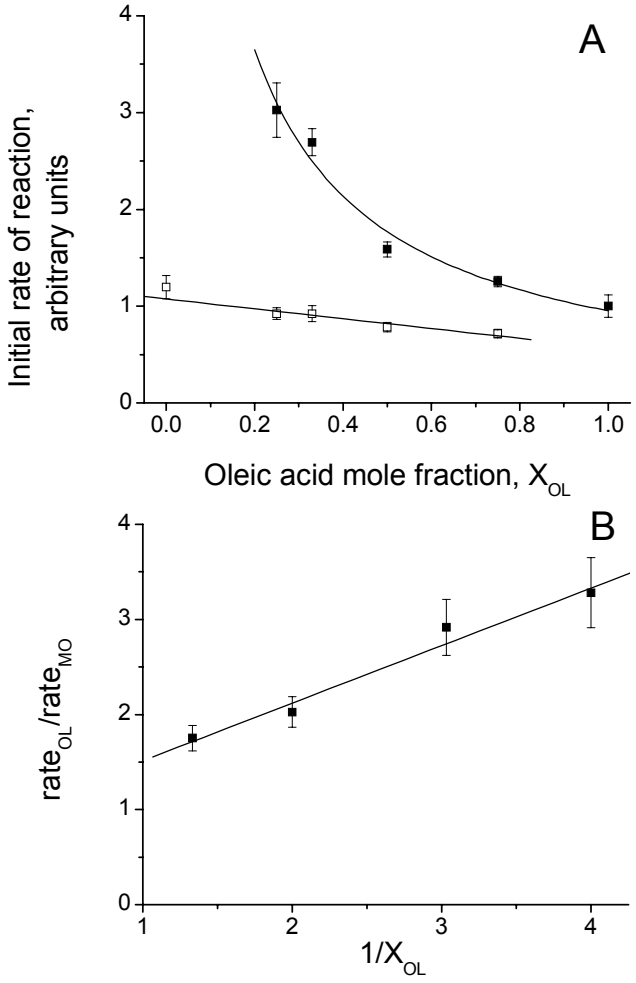

Figure 3.10. (A) Initial rates of reaction for internally mixed OL/MO particles as a function of OL mole fraction normalized to pure OL. The rate of OL significantly increases at smaller X_{OL}. (B) The ratio of the initial rates for OL and MO, and the slope of the linear fit indicates that 36% (±4%) of the observed OL loss is due to reaction with SCIs.

of 0.57. Therefore, the SCI secondary chemistry accounts for 36% (±4%) of the observed OL loss. Correcting γ_{OL} for this additional loss of OL yields $\gamma = 8.7 \times 10^{-4}$ and the reaction yield (φ) is 1.6.

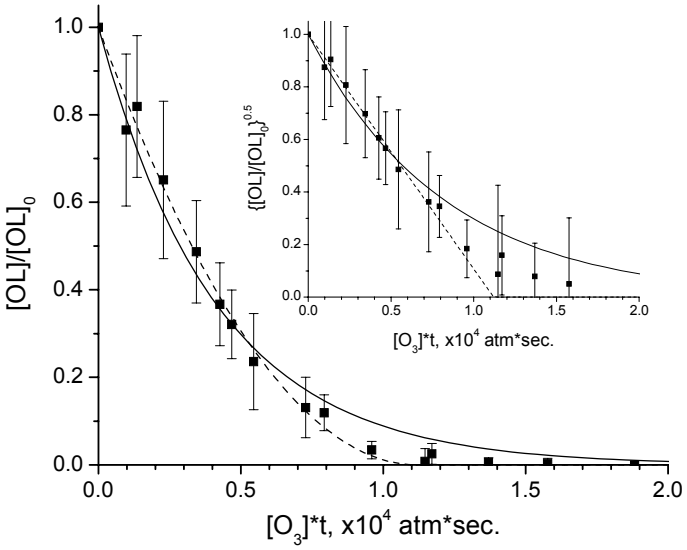

Figure 3.11. Reaction decay of OL in internally mixed particles of OL/MA (X_{OL} = 0.13). Lines represent fits to the data with exponential (solid) and quadratic (dashed) functions. The data is best described by a quadratic function which suggests these particles react near the surface. The inset shows the same data on a quadratic y-scale to illustrate the deviation from the exponential function.

The second approach to determining the contribution from SCI secondary chemistry is to make OL/MA or OL/LA internally mixed particles. This was accomplished via homogenous nucleation followed by size selection with the DMA as described in section 2.6. The resulting particles were supercooled at all compositions studied, and a discussion on phase effects on particle reactivity will be saved for Chapter 4. It is only important here to state that the particles were liquid. Figure 3.11 shows a reaction decay curve for an OL/MA mixture with X_{OL} = 0.13. Two things are apparent upon inspection of this plot. First, the rate of OL loss in the OL/MA mixture is faster

than in pure OL particles (compare to Figure 3.7A). This may seem counterintuitive at first since titrating the SCIs with MA should *reduce* OL reactivity, but the rate of observed decay for the condensed phase species for a reaction in the bulk near the particle surface should increase at lower concentrations. Secondly, at X_{OL} = 0.13, a quadratic function fits the data much better than an exponential function. This suggests that at the lower OL concentration the reaction occurs near the surface instead of at the surface (see equations (3.3) and (3.4)).

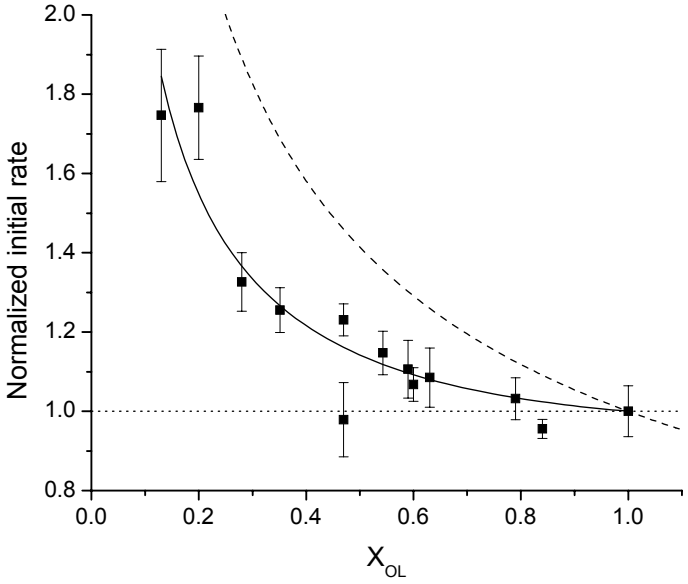

Figure 3.12. Initial rate of OL loss normalized to pure OL particles as a function fo OL mole fraction (X_{OL}). The dashed and dotted lines represent the expected dependences for a bulk reaction and a surface reaction, respectively. The solid line represents a fit to the data indicating that 38% of the OL loss is due to reaction with SCIs.

In order to get a more complete understanding of the effect MA and LA have on OL ozonolysis, particles comprised of several different compositions were reacted, and the initial slope normalized to pure OL is plotted as a function of X_{OL} in Figure 3.12. The initial slope increases at smaller X_{OL}, but there is only a 10% increase at X_{OL} = 0.5. A

bulk reaction occurring near the surface should show an inverse quadratic dependence on the initial slope with respect to concentration, and the dashed line shows the expected curve from this dependence. This line clearly overestimates the initial slope observed in the data. A surface reaction, on the other hand, should show no dependence on the initial slope with concentration, which clearly underestimates the data (dotted line in Figure 3.12). A surface reaction cannot be operative over the entire concentration range since the secondary chemistry contributes less to the OL reaction at lower X_{OL}. Neither case, however, accounts for secondary chemistry, so the data was fit to equation (3.10).

$$\text{Normalized initial rate} = \left(1 - f_{SCI}\right)\frac{1}{\sqrt{X_{OL}}} + \frac{f_{SCI}X_{OL}}{\sqrt{X_{OL}}} \tag{3.10}$$

In equation (3.10), f_{SCI} ($0 < f_{SCI} < 1$) is the fractional contribution to the observed OL loss from reaction with SCIs. The first term is the ozonolysis term, and the second term is the SCI term which decreases with decreasing X_{OL} because of the increased competition with MA or LA. The quadratic dependence in the second term is added because SCIs are produced from the ozonolysis reaction (bulk reaction for the mixtures). In the limit that the secondary chemistry is negligible ($f_{SCI} = 0$), this equation yields the expected [OL] dependence (dashed line in Figure 3.12). The solid line in Figure 3.12 shows the fit to the data using equation (3.10) yielding $f_{SCI} = 0.38 \pm 0.05$, meaning that 38% of the observed OL loss is due to reaction with SCI. This is consistent with the previous method using MO, and adds confidence to the importance of this secondary reaction.

3.4.3 Heterogeneous Kinetics Discussion

The results from the pure OL measurements show that $\gamma_{OL} = (1.38 \pm 0.06) \times 10^{-3}$, and this is consistent with other "particle uptake" measurements [12, 14], but significantly higher than O_3 uptake measurements [3, 5]. Correcting this by the 36% contribution from the SCI reaction yields $\gamma = \gamma_{OL}/\varphi = (8.8 \pm 0.5) \times 10^{-4}$, in much better agreement with coated flow tube experiments. The SCI secondary chemistry quantitatively explains the discrepancy between these two types of measurements, and these results emphasize the need to account for secondary chemistry when equating gas phase and condensed phase losses.

Morris et al. [12] also studied OL ozonolysis by monitoring particle signal using an Aerodyne aerosol mass spectrometer (AMS), and they measured $\gamma_{OL} = (1.6 \pm 0.2) \times 10^{-3}$, slightly higher than our measured value ($\gamma_{OL} = 1.38 \times 10^{-3}$). They also found that the OL reaction is best fit with a quadratic function, which is not consistent with the results described here. One possible reason for these discrepancies is that the particle generation technique used by Morris et al. left significant amounts of methanol on the particles (0.2 mole fraction). The presence of methanol can affect the surface ordering of OL [40], react with SCIs to alter the secondary chemistry [27], or change O_3 solubility and diffusion. We attempted to generate particles in a similar way by nebulizing an OL/methanol solution. These particles, like OL particles generated from nebulizing the pure liquid, exhibited an exponential reaction decay with the same initial slope. Due to the detection of both gas and condensed phases, we could not determine how much (if any) methanol remained on the particles. Therefore, we could not rule out methanol as the explanation of the higher γ_{OL} and quadratic fit to the data of Morris et al. One other

possible reason for these differences in the results from A-CIMS and AMS data is vaporization that is dependent on the O_3 exposure. The reaction between O_3 and OL produces some non-volatile products that most likely have a lower vapor pressure than OL. Since the AMS depends on flash vaporization in a vacuum chamber, it is possible that more viscous or solid (i.e. reacted) particles are vaporized less efficiently which yields an artificially faster decay in particle signal. In fact, total ion yield from OL particles in a single particle mass spectrometer with flash vaporization on a heated surface decreases with exposure to O_3. This would yield a higher γ_{OL} and might alter the shape of the decay curve.

Smith et al. [14] have also measured the heterogeneous kinetics of OL ozonolysis with a single particle mass spectrometer (SPMS) using a two-step laser ablation-ionization technique. The particles were first vaporized with a CO_2 laser and then the vapor plume was ionized with 118 nm laser light. They reported a size dependent γ_{OL}, and their smallest particles (diameter = 1.36 μm) yielded a much higher γ_{OL} (7.3×10^{-3}) than our particles (diameter = 0.65 – 1.1 μm). This is probably an experimental artifact from their vaporization technique. As the reaction proceeds, the concentration of carbonyl containing compounds increases which would absorb more of the CO_2 laser light [16]. This could lead to additional heating of the particle during vaporization which may cause more ion fragmentation and an artificially fast reaction of OL.

While the secondary chemistry quantitatively explains the discrepancy between particle and coated flow tube measurements, it is still unclear whether O_3 reacts with pure OL at the particle surface or near the surface in the bulk of the particle. The robust exponential fit for the pure OL particle decay is consistent with a surface reaction, but

could the secondary chemistry change the shape of the decay curve from a quadratic to exponential function? Any attempt to remove the secondary chemistry also changes the properties of the particle that may alter the reaction. For instance, OL is known to exist as a quasi-smectic liquid crystal that gives a remarkable amount of order at the surface [40]. This makes pure OL look more like a self-assembled monolayer than an isotropic liquid, and this ordering may facilitate a surface reaction [11]. Adding another component may disrupt the ordering which could suppress a surface reaction, and additionally, it will alter the secondary chemistry either through reaction with SCIs or dilution of OL and SCIs. Therefore, the secondary chemistry and the surface ordering cannot be decoupled from one another in any experiment of internally mixed particles.

A qualitative argument can be made for the secondary chemistry changing the shape of the decay curve from a quadratic function to a non-quadratic function. Initially, OL is the only acidic component in the particle, so there are no other carboxylic acids competing for reaction with SCIs. As the reaction proceeds, acidic products are produced (azelaic acid and 9-oxononanoic acid, see below) which will compete for the available SCIs. This will slow the secondary losses of OL at long exposures and cause the normalized OL signal to deviate above the quadratic function and become "more" exponential. I would like to emphasize that this argument only provides a qualitative reason for a deviation from a quadratic function that is in the right direction to explain an exponential dependence, but the robust exponential fit to the data begs for a more satisfying explanation.

3.5 Products from OL ozonolysis

In addition to measuring the kinetics for predicting the rate of oxidation of atmospheric organic aerosol, it is important to know what the products are from heterogeneous reactions in order to predict property changes of the particle. For instance, products with a smaller molecular weight may be more volatile than the parent organic and leave the particle, thus providing a mechanism for shortening the lifetime of organic aerosol. Additionally, adding oxygen functionality to the parent compound reduces volatility and may prolong organic aerosol lifetime. Finally, functional groups containing oxygen cause the hygroscopicity to increase which can make particles more likely to become cloud condensation nuclei (CCN) [41, 42]. Since A-CIMS offers little fragmentation, it provides a unique opportunity to measure intact molecular ions from a heterogeneous reaction which in principle can be used for measuring reaction yields. As mentioned above, O_3 adds across a carbon-carbon double bond and the resulting structure quickly decomposes (see Figure 3.1). This decomposition can form two sets of products depending on which carbon-oxygen bond breaks. In an attempt to identify and quantify the products from OL ozonolysis, we collected spectra from reacted OL particles, and the results are shown in Figure 3.13. Product peaks appear at m/z = 143, 159, 173, and 189 corresponding to protonated nonanal, nonanoic acid, 9-oxononanoic acid, and azelaic acid, respectively. These are the four expected primary products from OL ozonolysis (see Figure 3.1). Additional peaks are observed at m/z = 141, 153, 155, and 171 corresponding to loss of one or two water molecules from nonanoic acid, azelaic acid, 9-oxononanoic acid, and azelaic acid, respectively. This fragmentation, while undesirable, corroborates the previous assignments for the molecular ions, and since each fragment

has a unique parent, quantification can in principle be achieved by summing the peaks together.

Unfortunately, the three commercially available products cover a wide range of vapor pressures from nonanal (≈ 640 mTorr at 25ºC [16]) to nonanoic acid (≈ 1 mTorr at 20ºC [43]) to azelaic acid (≈ 5×10^{-8} Torr at 21-38ºC [44]), and therefore relative sensitivities of these products cannot be obtained. Azelaic acid does have sufficiently low volatility that its sensitivity can be measured relative to OL. A binary mixture of the

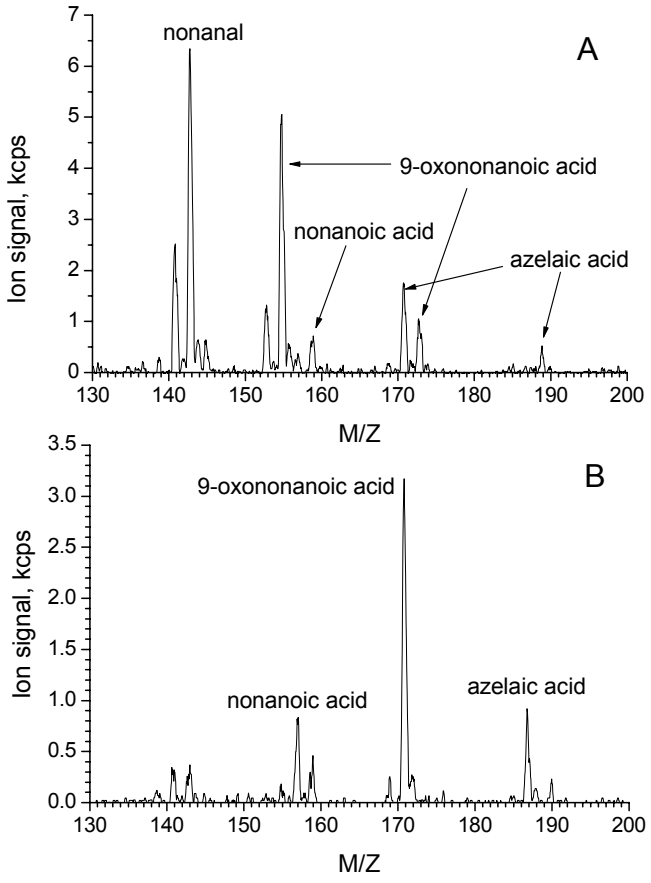

Figure 3.13. Product spectra of the reaction of OL particles with O_3 using (A) proton transfer ionization from $(H_2O)_nH^+$ and (B) proton abstraction from O_2^-. The abundance of the aldehyde products is significantly higher than the SCI rearrangement products.

two acids was heated until mixed, and the warm mixture was nebulized to make an aerosol. The internally mixed aerosol was sent into the A-CIMS to measure signals at m/z = 283 and 189, and this gave a relative sensitivity for azelaic acid to OL of 1.3 ± 0.4. This calibration does not include the azelaic acid fragment peaks (m/z = 171 and 153) which would increase its detection efficiency. The better detection of azelaic acid is probably caused by a combination of a quadrupole transmission bias and perhaps a faster proton transfer reaction rate constant for azelaic acid. In order to measure a yield for azelaic acid, the injector was pulled back to react > 95% of the OL in the flow tube to minimize the contribution of a gas phase reaction in the vaporizer or ion tube to the azelaic acid signal. Using the above sensitivity of azelaic acid, its yield is 0.12 ± 0.04. This low yield is consistent with a significant reaction between SCIs and OL.

Since relative sensitivities of the other products cannot be obtained, we will assume that the products are ionized and transported through the quadrupole with the same efficiency as azelaic acid. These are valid approximations because all the products are in a narrow mass range (m/z = 143 – 189) which will give more uniform transmission through the quadrupole (see Chapter 2), and the difference in proton transfer rate constants between carboxylic acids and aldehydes is probably small. For instance, the proton transfer rate constants for acetaldehyde and acetic acid are 3.6×10^{-9} cm^3/molecule/second and 3.0×10^{-9} cm^3/molecule/second, respectively [45]. With these assumptions the signals for each product ion and its fragments (if any) were summed and compared. The nonanal/ azelaic acid signal ratio was ≈ 7 giving a nonanal yield of 0.84. Because of the broad assumptions, this nonanal yield only represents an estimate. Similarly, yields for nonanoic acid and 9-oxononanoic acid are estimated to be 0.17 and

0.83, respectively. The low yields of the SCI rearrangement products (nonanoic acid and azelaic acid) are not surprising since they are involved in additional reactions such as those with carboxylic acid functional groups [29].

As a complimentary experiment, reaction products were measured using negative ionization with O_2^-, as the primary ion. O_3 will dominate the negative ion chemistry if present, so for this ion scheme, the reaction was done off-line in a 500 mL flask. Reacted particles were swept out with a small flow of N_2 and analyzed with A-CIMS, and because the extent of OL reaction is not known, absolute yields cannot be obtained. O_2^- does not ionize aldehydes, so it is a more direct comparison between 9-oxononanoic acid and the two SCI rearrangement products since only the carboxylic acid moieties are involved in ionization. Panel B in Figure 3.13 shows the spectrum of the reacted particles with the intense peaks at m/z = 157, 171, and 187 corresponding to the proton abstraction ions of nonanoic acid, 9-oxononanoic acid, and azelaic acid, respectively. Only a small peak at m/z = 141 is observed for nonanal. The peak intensities from the acidic products can be directly compared since the mechanism of ionization is the same and there is no significant fragmentation. The 9-oxononanoic acid signal is approximately three fold higher than the other primary product peaks, corroborating the results from the proton transfer ionization measurements. The lower yield of SCI rearrangement products is expected since they do react with OL to form α-acyloxyalkyl hydroperoxides [29]. These products, however, are not observed in the mass spectrum. The most likely reason for this is that the peroxide bond is unstable at the elevated temperatures in the vaporizer and ionization region. In fact, we have monitored H_2O_2 with the vaporizer and ion tube cold and hot, and the signal significantly decreases at elevated temperature (data not shown).

Nevertheless, the kinetic analysis suggests that these products are being made. There are also at least two other alternative fates for the SCIs. One is a self reaction that produces two aldehydes [31], and the other is a recently proposed reaction of SCIs with a carbon-carbon double bond [9]. The self reaction (Figure 3.14) provides a well established mechanism consistent with our observation of increased aldehyde yield relative to the SCI rearrangement products [31]. The second mechanism (Figure 3.15) also generates additional aldehyde (nonanal or 9-oxononanoic acid) as well as a ketone product that would be 16 amu higher than OL (m/z = 299). Indeed, in Figure 3.16, we see a rise in a peak at m/z = 299 after OL ozonolysis providing positive evidence for this mechanism. If the relative sensitivity between this product and OL is similar, then this mechanism is minor and cannot explain the large apparent yield of aldehyde products. Additionally, the SCI – double bond reaction plays a minor role compared with the SCI – carboxylic acid reaction since the kinetics of OL in the binary mixtures discussed in section 3.4.2 reconciles particle and coated flow tube experiments.

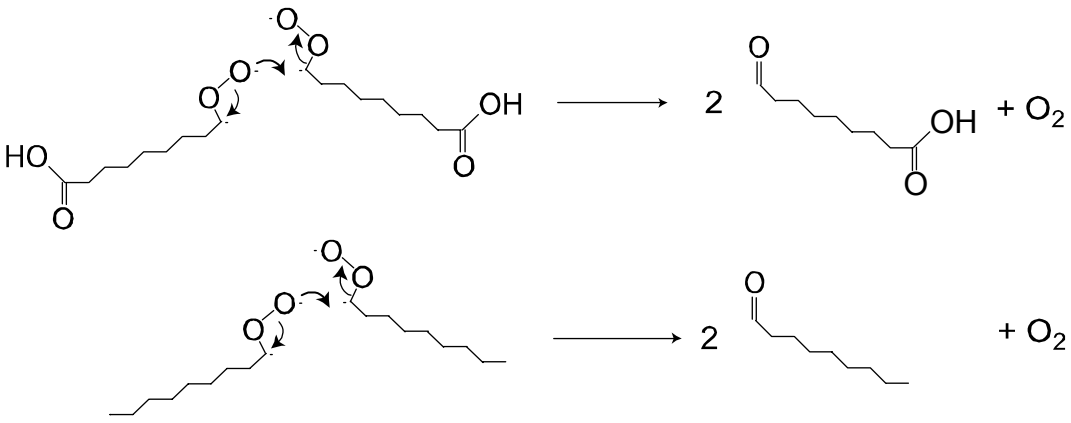

Figure 3.14. Proposed reaction mechanism for SCI self reaction to explain the large yields of nonanal and 9-oxononanoic acid relative to the SCI rearrangement products. An additional possibiltiy is reaction between two different SCIs to form both nonanal and 9-oxononanoic acid.

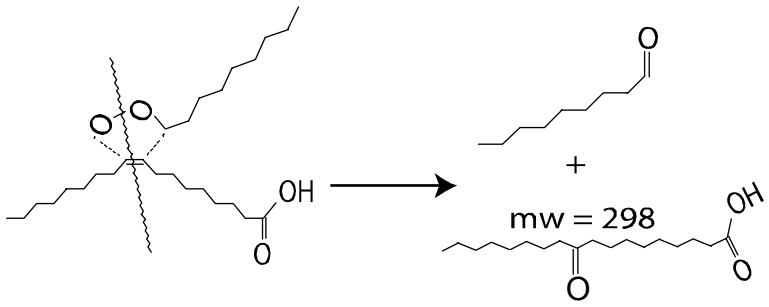

Figure 3.15. Mechanism proposed to explain the appearance of a product at m/z = 299. The SCI adds across the double bond and this complex decomposes yielding an aldehyde and a ketone.

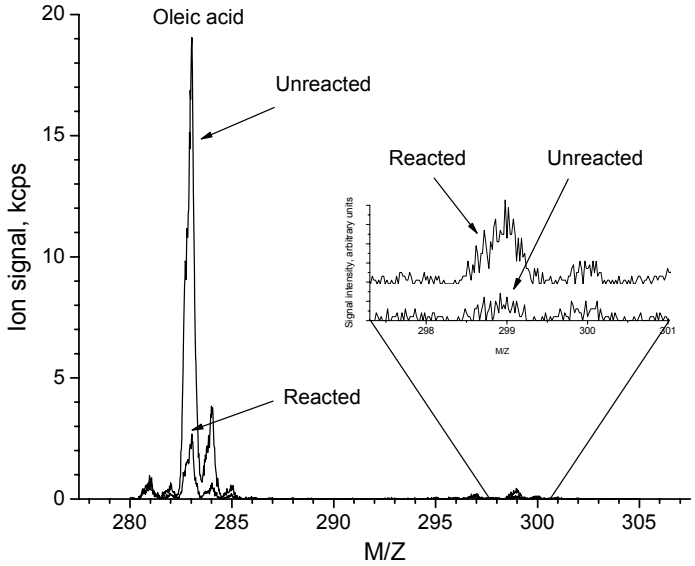

Figure 3.16. Spectra of reacted and unreacted OL particles. The OL signal (m/z = 283) decreases and a peak at m/z = 299 increases. This corresponds to an expected product (9-oxooctadecanoic acid) from the reaction between SCI's and the double bond of OL.

In addition to OL ozonolysis, we detected the expected products from ozonolysis of LO, OLA, and OD. Table 3.2 shows the detected peaks and their product names. OLA and OD yield all four expected primary products from the ozonolysis reaction where the primary ozonide decomposes by breaking either C-O bond. Since LO has two double bonds, there are eight possible primary products from its reaction with O_3. We

have detected 7 of the expected products with proton transfer ionization listed in Table 3.2. The eighth product, dodecenedioic acid, was not observed, and this may be because it is a SCI rearrangement product which would give it a low yield. Additionally, it has a double bond, so its reaction with O_3 would lower its yield even more.

Table 3.2. Products detected using A-CIMS from reactions of O3 with OLA, LO, and OD. Products were ionized with proton transfer (PT), and some products fragmented with the loss of water (WL) while formaldehyde associated with water. ND = not detected.

	Product name	MW, amu	Products peaks
OLA	nonanal	142	PT
	9-hydroxynonanal	158	PT, WL
	nonanoic acid	158	PT, WL
	9-hydroxynonanoic acid	172	PT, WL
LO	hexanal	100	PT
	hexanoic acid	116	PT, WL
	nonenal	140	PT
	nonenoic acid	156	PT, WL
	9-oxononanoic acid	172	PT, WL
	azelaic acid	188	PT, WL, 2-WL
	9-oxododecenoic acid	212	PT, WL
	dodecenedioic acid	228	ND
OD	formic acid	46	PT
	formaldehyde	30	PT+H_2O
	heptadecanal	254	PT
	heptadecanoic acid	270	PT

3.5.1 Product volatility

Since A-CIMS detects aerosol components, it is not obvious whether products are partitioning to the gas or condensed phases. Nonanal has a high vapor pressure, and some recent studies have identified it as a major gas phase product with a yield of (≈ 0.5) [5]. In order to determine the partitioning of ozonolysis products, particles were reacted

off line in a 500 mL flask, and they were either sampled into the vaporizer or directed off-axis. The off line reaction was necessary because particles directed off-axis will have a longer resonance time in the flow tube which would change the exposure of an on-line reaction. Since gas phase products have a much higher diffusion rate than particles, they will be sampled into the vaporizer and detected whether particles are directed on- or off-axis. Figure 3.17 shows a plot of integrated signal from nonanal (m/z = 143), nonanoic acid (m/z = 159), 9-oxononanoic acid (m/z = 173), azelaic acid (m/z = 189), oleic acid

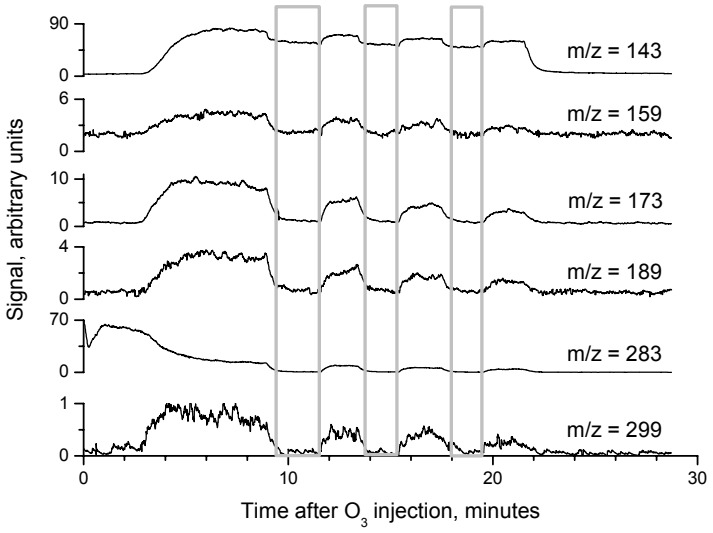

Figure 3.17. Integrated A-CIMS signals from OL and its ozonolysis products in an off line reaction after ozone injection (t = 0 minutes). The delay in OL signal loss and product signal rises after O_3 injection is caused by a lag in the O_3 flow reaching the reaction flask. The gray boxes indicate when the injector was directed off axis and the particle flow was removed at 22 minutes for a background measurement.

(m/z = 283), and 9-oxohexadecanoic acid (m/z = 299) where the particles were alternately directed on and off axis. Products with expected low volatility (azelaic acid and 9-oxononanoic acid) and OL provide positive controls for the experiment. Their signals return to background levels when the particles are directed off-axis (shaded areas), verifying that no particles are entering the vaporizer. While nonanoic acid has a

relatively high vapor pressure (≈ 1 mTorr at 20ºC), it is found primarily in the condensed phase. Nonanal, on the other hand, shows a large gas phase signal (off-axis signal), but the drop from the on-axis signal indicates that a sizeable fraction of nonanal remains on the particles. Both of these observations are consistent with previous studies. Nonanal has been observed as a gas phase product from O_3 reacting with a surface coated with OL [5], and it has also been detected on reacted OL particles [46]. It is impossible to determine the fraction of nonanal on the particles since there is contribution to the gas phase nonanal signal from O_3 reacting with OL on the walls of the flask and reacted particles that have deposited on the walls of the flask and injector. Nevertheless, these results show that nonanal partitions to both the gas and particle phases on the time scale of our experiment (minutes).

The significant partitioning of nonanal to the condensed phase is a little surprising, but other products such as azelaic acid, 9-oxononanoic acid, or α-acyloxyalkyl hydroperoxide (not observed) could reduce the effective nonanal vapor pressure. This trapping may act to lengthen particle lifetime by retaining mass that would otherwise partition to the gas phase. One other possible reason for the significant retention of nonanal in the condensed phase is the total organic concentration used in the experiment. Gas phase partitioning is anti-correlated to the total organic aerosol concentration [47], and these experiments employed rather high concentrations (≈ 200 $\mu g/m^3$) whereas ambient levels are much lower (1-10 $\mu g/m^3$) [33]. This may cause an artificially low gas phase partitioning of nonanal to be observed in our experiments and the experiments of LaFranchi et al [46].

3.6 Conclusions and Atmospheric Implications

Heterogeneous oxidation of organic aerosol has been examined in detail through the reaction of O_3 with particles composed of unsaturated organics of which OL has been the focus. Heterogeneous kinetics were measured with both polydisperse and monodisperse size distributions, and while the polydisperse results gave reasonable answers, it was systematically low. A monodisperse particle distribution greatly simplifies kinetic analysis, but the uptake coefficient for OL was systematically higher than coated flow tube measurements. This high γ was found to be caused by SCIs reacting with the carboxylic acid moiety of OL. This secondary chemistry is significant and accounts for 37% of the observed OL loss. Correcting γ_{OL} for this additional loss reduces γ_{OL} from 1.38×10^{-3} to 8.7×10^{-4} which is in good agreement with coated flow tube measurements. From these kinetic measurements, ambient OL lifetime would be a few hours at atmospheric concentrations of O_3 ($\approx$ 100 ppb). This is not consistent with field measurements which first of all detect OL, and secondly, estimate that OL has a lifetime of several days. However, the kinetic measurements made here are for particles comprised of one or two liquid components, and other components may change properties that slow the reaction such as viscosity, phase, solubility, etc. Some of these effects will be examined in more detail in chapter 4.

Products from ozonolysis reactions are more heavily oxidized than the precursor which may change hygroscopicity and the particles ability to act as cloud condensation nuclei (CCN). While no hygroscopic or CCN activity measurements were made in this work, others have measured these properties for ozonolysis reactions and seen an increase in the water uptake of reacted OL particles [41, 42]. Our results are consistent

with increased water uptake because more oxygenated organics (higher O/C ratio) will be more hygroscopic than their precursors. Gas-particle partitioning of OL ozonolysis products was also measured, and nonanal was the only product that significantly evaporated from the particles. The incomplete evaporation of nonanal may be a result of either a reduction in the vapor pressure caused by nonvolatile and solid products or the high organic aerosol concentrations employed in these experiments. More work needs to be done to determine the cause of the condensed phase partitioning of nonanal observed in these experiments.

References

1. Hearn, J.D. and G.D. Smith, *A chemical ionization mass spectrometry method for the online analysis of organic aerosols.* Analytical Chemistry, 2004. **76**(10): p. 2820-2826.

2. Hearn, J.D. and G.D. Smith, *Reactions and mass spectra of complex particles using Aerosol CIMS.* International Journal of Mass Spectrometry, 2006. **258**(1-3): p. 95-103.

3. Moise, T. and Y. Rudich, *Reactive Uptake of Ozone by Aerosol-Associated Unsaturated Fatty Acids: Kinetics, Mechanism, and Products.* Journal of Physical Chemistry A, 2002. **106**: p. 6469-6476.

4. Zahardis, J., B.W. LaFranchi, and G.A. Petrucci, *Direct observation of polymerization in the oleic acid-ozone heterogeneous reaction system by photoelectron resonance capture ionization aerosol mass spectrometry.* Atmospheric Environment, 2006. **40**(9): p. 1661-1670.

5. Thornberry, T. and J.P.D. Abbatt, *Heterogeneous reaction of ozone with liquid unsaturated fatty acids: detailed kinetics and gas-phase product studies.* Phys. Chem. Chem. Phys., 2004. **6**: p. 84-93.

6. Nash, D.G., M.P. Tolocka, and T. Baer, *The uptake of O-3 by myristic acid-oleic acid mixed particles: evidence for solid surface layers.* Physical Chemistry Chemical Physics, 2006. **8**(38): p. 4468-4475.

7. Asad, A., B.T. Mmereki, and D.J. Donaldson, *Enhanced uptake of water by oxidatively processed oleic acid.* Atmospheric Chemistry and Physics, 2004. **4**(8): p. 2083-2089.

8. Katrib, Y., et al., *Density changes of aerosol particles as a result of chemical reaction.* Atmospheric Chemistry and Physics, 2005. **5**: p. 275-291.

9. Katrib, Y., et al., *Products and mechanisms of ozone reactions with oleic acid for aerosol particles having core-shell morphologies.* Journal of Physical Chemistry A, 2004. **108**(32): p. 6686-6695.

10. Knopf, D.A., L.M. Anthony, and A.K. Bertram, *Reactive uptake of O-3 by multicomponent and multiphase mixtures containing oleic acid.* Journal of Physical Chemistry A, 2005. **109**(25): p. 5579-5589.

11. Hearn, J.D., A.J. Lovett, and G.D. Smith, *Ozonolysis of oleic acid particles: evidence for a surface reaction and secondary reactions involving Criegee intermediates.* Physical Chemistry Chemical Physics, 2005. **7**(3): p. 501-511.

12. Morris, J.W., et al., *Kinetics of submicron oleic acid aerosols with ozone: A novel aerosol mass spectrometric technique.* Geophysical Research Letters, 2002. **29**(9): p. -.

13. Hearn, J.D. and G.D. Smith, *Kinetics and product studies for ozonolysis reactions of organic particles using aerosol CIMS.* Journal of Physical Chemistry A, 2004. **108**(45): p. 10019-10029.

14. Smith, G.D., et al., *Reactive uptake of ozone by oleic acid aerosol particles: Application of single-particle mass spectrometry to heterogeneous reaction kinetics.* Journal of Physical Chemistry A, 2002. **106**(35): p. 8085-8095.

15. Zahardis, J. and G.A. Petrucci, *The oleic acid-ozone heterogeneous reaction system: products, kinetics, secondary chemistry, and atmospheric implications of a model system – a review.* Atmospheric Chemistry and Physics, 2006. **6**(6): p. 11093-11179.

16. *CRC Handbook of Chemistry and Physics*. 76 ed, ed. D.R. Lide. 1995, Boca Raton, FL: CRC Press, Inc.

17. Rogge, W.F., et al., *Sources of Fine Organic Aerosol .1. Charbroilers and Meat Cooking Operations.* Environmental Science & Technology, 1991. **25**(6): p. 1112-1125.

18. Rogge, W.F., et al., *Sources of Fine Organic Aerosol .2. Noncatalyst and Catalyst-Equipped Automobiles and Heavy-Duty Diesel Trucks.* Environmental Science & Technology, 1993. **27**(4): p. 636-651.

19. Rogge, W.F., et al., *Sources of fine organic aerosol. 9. Pine, oak and synthetic log combustion in residential fireplaces.* Environmental Science & Technology, 1998. **32**(1): p. 13-22.

20. Rogge, W.F., et al., *Sources of Fine Organic Aerosol .6. Cigarette-Smoke in the Urban Atmosphere.* Environmental Science & Technology, 1994. **28**(7): p. 1375-1388.

21. Zozom, J., et al., *Microwave Detection of the Primary Ozonide of Ethylene in the Gas-Phase.* Chemical Physics Letters, 1987. **140**(1): p. 64-70.

22. Kohlmiller, C.K. and L. Andrews, *Infrared-Spectrum of the Primary Ozonide of Ethylene in Solid Xenon.* Journal of the American Chemical Society, 1981. **103**(10): p. 2578-2583.

23. Rickard, A.R., et al., *OH yields in the gas-phase reactions of ozone with alkenes.* Journal of Physical Chemistry A, 1999. **103**(38): p. 7656-7664.

24. Horie, O. and G.K. Moortgat, *Decomposition Pathways of the Excited Criegee Intermediates in the Ozonolysis of Simple Alkenes.* Atmospheric Environment Part a-General Topics, 1991. **25**(9): p. 1881-1896.

25. Baker, J., et al., *Reactions of stabilized Criegee intermediates from the gas-phase reactions of O-3 with selected alkenes.* International Journal of Chemical Kinetics, 2001. **34**(2): p. 73-85.

26. Tobias, H.J. and P.J. Ziemann, *Kinetics of the gas-phase reactions of alcohols, aldehydes, carboxylic acids, and water with the C13 stabilized Criegee intermediate formed from ozonolysis of 1-tetradecene.* Journal of Physical Chemistry A, 2001. **105**(25): p. 6129-6135.

27. Tobias, H.J. and P.J. Ziemann, *Thermal Desorption Mass Spectrometric Analysis of Organic Aerosol Formed from Reactions of 1-Tetradecene and O3 in the Presence of Alcohols and Carboxylic Acids.* Environmental Science and Technology, 2000. **34**(11): p. 2105-2115.

28. Ziemann, P.J., *Formation of alkoxyhydroperoxy aldehydes and cyclic peroxyhemiacetals from reactions of cyclic alkenes with O-3 in the presence of alcohols.* Journal of Physical Chemistry A, 2003. **107**(12): p. 2048-2060.

29. Rebrovic, L., *The Peroxidic Species Generated by Ozonolysis of Oleic Acid or Methyl Oleate in a Carboxylic Acid Medium.* Journal of the American Oil Chemists Society, 1992. **69**(2): p. 159-165.

30. Yin, H.Y., D.L. Hachey, and N.A. Porter, *Structural analysis of diacyl peroxides by electrospray tandem mass spectrometry with ammonium acetate: bond homolysis of peroxide-ammonium and peroxide-proton adducts.* Rapid Communications in Mass Spectrometry, 2000. **14**(14): p. 1248-1254.

31. Bailey, P.S., *Ozonation in Organic Chemistry*. Vol. 1. 1978, New York: Academic Press.

32. Ziemann, P.J., *Aerosol products, mechanisms, and kinetics of heterogeneous reactions of ozone with oleic acid in pure and mixed particles.* Faraday Discussions, 2005. **130**: p. 469-490.

33. Finlayson-Pitts, B.J. and J.N.J. Pitts, *Chemistry of the Upper and Lower Atmosphere*. 2000, San Diego, CA: Academic Press. 969.

34. Worsnop, D.R., et al., *A chemical kinetic model for reactive transformations of aerosol particles.* Geophysical Research Letters, 2002. **29**(20): p. -.

35. Hearn, J.D. and G.D. Smith, *Measuring rates of reaction in supercooled organic particles with implications for atmospheric aerosol.* Physical Chemistry Chemical Physics, 2005. **7**(13): p. 2549-2551.

36. Houston, P.L., *Chemical Kinetics and Reaction Dynamics*. 2001, New York, NY: McGraw-Hill.

37. Giamalva, D.H., D.F. Church, and W.A. Pryor, *Kinetics of Ozonation .4. Reactions of Ozone with Alpha-Tocopherol and Oleate and Linoleate Esters in Carbon-Tetrachloride and in Aqueous Micellar Solvents.* Journal of the American Chemical Society, 1986. **108**(21): p. 6646-6651.

38. Atkinson, R., *Gas-phase tropospheric chemistry of volatile organic compounds .1. Alkanes and alkenes.* Journal of Physical and Chemical Reference Data, 1997. **26**(2): p. 215-290.

39. Moise, T. and Y. Rudich, *Uptake of Cl and Br by organic surfaces - a perspective on organic aerosols processing by tropospheric oxidants.* Geophysical Research Letters, 2001. **28**(21): p. 4083-4086.

40. Iwahashi, M., et al., *Self-diffusion, dynamical molecular conformation, and liquid structures of n-saturated and unsaturated fatty acids.* Journal of Physical Chemistry B, 2000. **104**(26): p. 6186-6194.

41. Demou, E., et al., *Uptake of water by organic films: the dependence on the film oxidation state.* Atmospheric Environment, 2003. **37**(25): p. 3529-3537.

42. Broekhuizen, K.E., et al., *Formation of cloud condensation nuclei by oxidative processing: Unsaturated fatty acids.* Journal of Geophysical Research-Atmospheres, 2004. **109**(D24): p. -.

43. Daubert, T.E. and R.P. Danner, *Physical and thermodynamic properties of pure chemicals : data compilation*. 1989, New York, NY: Hemisphere.

44. Chattopadhyay, S. and P.J. Ziemann, *Vapor pressures of substituted and unsubstituted monocarboxylic and dicarboxylic acids measured using an improved thermal desorption particle beam mass spectrometry method.* Aerosol Science and Technology, 2005. **39**(11): p. 1085-1100.

45. Zhao, J. and R.Y. Zhang, *Proton transfer reaction rate constants between hydronium ion (H3O(+)) and volatile organic compounds.* Atmospheric Environment, 2004. **38**(14): p. 2177-2185.

46. LaFranchi, B.W., J. Zahardis, and G.A. Petrucci, *Photoelectron resonance capture ionization mass spectrometry: a soft ionization source for mass spectrometry of particle-phase organic compounds.* Rapid Communications in Mass Spectrometry, 2004. **18**(21): p. 2517-2521.

47. Robinson, A.L., et al., *Rethinking organic aerosols: Semivolatile emissions and photochemical aging.* Science, 2007. **315**(5816): p. 1259-1262.

CHAPTER 4

EFFECTS OF SOLID CONSTITUENTS ON ORGANIC AEROSOL REACTIVITY[1]

4.1 Introduction

Organic matter comprises a large fraction of tropospheric aerosol, and sources of organic material include cooking [1-3], vegetative emissions, biomass burning [4, 5], and automobile exhaust [6]. Reactive gases, such as ozone or the hydroxyl radical, can chemically transform organic particles [7]. Volatile products will leave the particle, possibly reducing particle size or changing particle density [8], and more oxygenated products may lead to more hygroscopic particles that can act as cloud condensation nuclei [9, 10]. It is important to understand the kinetics and mechanisms of these chemical processes to predict their importance in atmospheric processes, and as a model for organic aerosol, the reaction of oleic acid (OL) with ozone has been the focus of several recent studies [8, 10-26].

Oleic acid is an 18-carbon carboxylic acid with a double bond, and it is one of the major emissions from charbroiling meat [1]. It has been found on atmospheric particles, and its reaction with ozone has become a benchmark for studying organic heterogeneous reactions [26]. Ambient measurements have indicated that the lifetime of oleic acid in atmospheric particles is on the order of days [1, 23]. However, extrapolating laboratory results of pure OL particle reactivity to ambient conditions (submicron particles and 100

[1] Hearn, J.D. and G.D. Smith, *Measuring rates of reaction in supercooled organic particles with implications for atmospheric aerosol.* Physical Chemistry Chemical Physics, 2005. **7**(13): p. 2549-2551. Reproduced in part with permission of the publisher.

ppb of ozone) [7] predicts a lifetime of only a few minutes (see Chapter 3). One possible reason for this discrepancy is that ambient particles contain many different compounds that could inhibit or compete with the reaction of ozone with oleic acid whereas laboratory generated particles generally have only one or two components.

Alkanoic acids comprise the largest fraction of organic emission from meat-cooking [1], and since these compounds are solid in the bulk at room temperature, they may greatly affect the reactivity of oleic acid generated from this source. In fact, recent work by Ziemann has shown that OL can be "trapped" by solid alkanoic acids [22]. This reduction in the reactivity lengthens the predicted lifetime of ambient oleic acid. Knopf et al. [19] have also investigated ozone reactions with binary mixtures of oleic acid and solid alkanoic acids by coating the inner walls of a flow tube and monitoring the gas phase ozone concentration. They saw a decrease in reactivity by an order of magnitude when solid alkanoic acid was present, and they also measured ozone uptake on a mixture that closely resembled meat cooking aerosol. From this they predicted a lifetime of 2 hours for ambient OL which is much longer than the predictions based on measurements of pure OL (a few minutes), but it is still shorter than what ambient measurements predict [1, 23].

In order to more fully understand the role of solid constituents in organic particle reactivity, we use binary mixtures of alkanoic acids and either oleic acid or methyl oleate (the methyl ester of oleic acid) as simple proxies for meat cooking aerosol and docosane and oleic acid as a simple proxy for diesel exhaust. Our findings suggest that some mixed particles exist as supercooled liquid droplets whereas others contain solid domains that inhibit heterogeneous reaction. Additionally, in stearic acid mixtures, methyl oleate

is more reactive than oleic acid suggesting that oleic acid has a stronger interaction with stearic acid that aids in its trapping. Oleic acid/docosane mixtures exhibit some aberrant behavior that suggests the formation of a solid surface layer that protects the interior of the particle from ozone. This surface layer, however, is only operative over a narrow range of compositions. Finally, we reacted meat cooking aerosol with O_3 to determine the reactivity of particles that are more representative of ambient aerosol and found that part of the OL reacted quickly while a significant fraction was unreactive with O_3.

4.2 Materials and Methods

Internally mixed particles were generated by homogenous nucleation as described in section 2.6. A monodisperse size distribution was selected from the polydisperse aerosol by an electrostatic classifier (TSI model 3080), and the polydisperse size distribution was sufficiently narrow that multiply charged particles were absent from the exiting flow. Oleic acid mole fractions in the mixtures were determined by comparing the ion signals from the two components and correcting for their relative sensitivities. To measure the relative detection sensitivities of the components in the mixtures, internally mixed aerosols were generated by making a known mixture by mass and nebulizing the heated mixture into a flask. Polydisperse particles were then swept out of the flask with a flow of nitrogen (10-20 sccm) and sampled into the A-CIMS. The relative detection sensitivities were then used to determine the composition of the particles generated via homogenous nucleation. The relative sensitivities for oleic acid and the other alkanoic acids were routinely 1.00 (±0.15) (i.e. for the same number of molecules, the same mass spectrometer signal was observed). For oleic acid and docosane, the relative sensitivities

for their hydride abstraction peaks were lower ($S_{OL}/S_{DO} \approx 0.5$) which was probably because half of the oleic acid signal was detected as the NO adduct.

Particles were vaporized, ionized, and detected as described in Chapter 2. For the alkanoic acid mixtures, protonated water clusters were used for proton transfer ionization. NO^+ was used as the primary ion for the docosane mixture experiments since alkanes are not ionized with proton transfer ionization. Oleic acid was observed as m/z = 283 and 281 with proton transfer ionization ($H^+(H_2O)_n$) and hydride abstraction ionization (NO^+), respectively. The NO^+ addition peak was also observed, but it was not used for any of the kinetic analysis.

A phase diagram for the binary mixture of oleic acid and docosane was measured using a differential scanning calorimeter (model DSC 7, Perkin Elmer). An empty aluminum pan was placed in the reference furnace, and the instrument was scanned with a constant temperature rate (5ºC/min.). The heat flow was measured during the temperature scan, and the temperature at the peak of the heat flow was used as the temperature of the phase transition.

Gases were purchased from National Welders with the following purities: N_2 (99.99%), O_2 (99.5% through polonium, 99.99% for ozone generation), and NO (99.5%). Ozone was generated and stored as described in section 3.2. Oleic acid (90%), stearic acid (95%), palmitic acid (99%), myristic acid (99%), lauric acid (99%), and methyl oleate (99%), were purchased from Sigma Aldrich and used without further purification. Docosane (98%) was purchased from Fluka.

4.3 Effect of alkanoic acids on heterogeneous kinetics

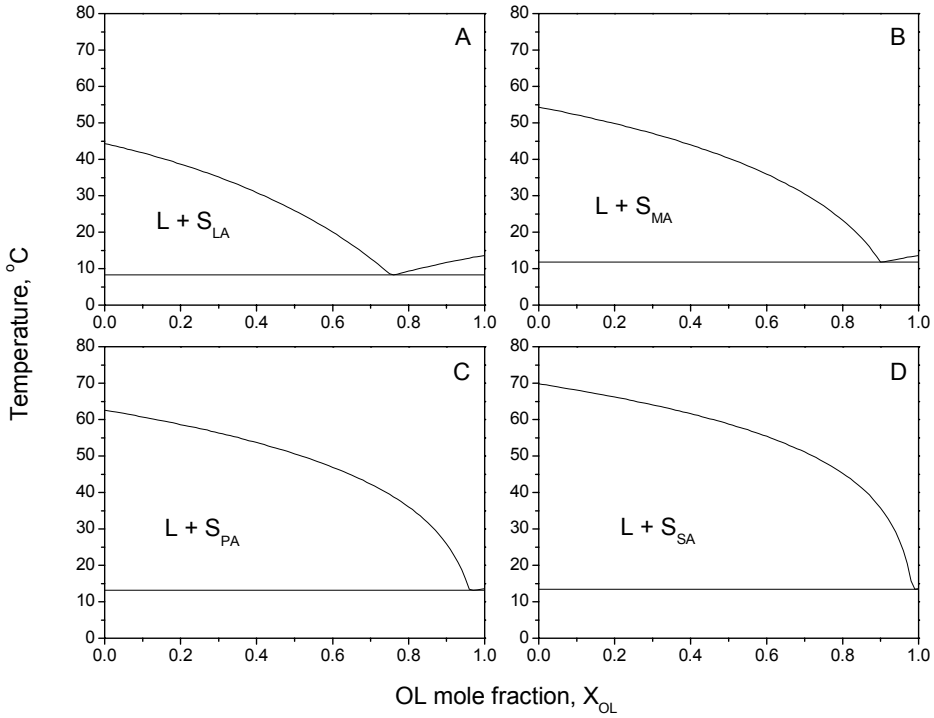

Figure 4.1. Phase diagrams for OL/alkanoic acid mixtures taken from Inoue et al. for (A) OL/LA, (B) OL/MA, (C) OL/PA, and (D) OL/SA binary mixtures [27, 28].

As a simple proxy for meat cooking aerosol, particles with a mean diameter of 700 nm containing oleic acid (OL) and either stearic acid (SA), palmitic acid (PA), myristic acid (MA), or lauric acid (LA) were reacted with ozone. The bulk phase diagrams have been measured previously by Inoue et al., and their results are presented in Figure 4.1 [27, 28]. All of the OL/alkanoic acid mixtures have a biphasic region consisting of a liquid mixture and solid alkanoic acid, and at room temperature, the liquidous curve crossing decreases in OL mole fraction from SA>PA>MA>LA. In the sections that follow, I will show that alkanoic acids can increase or decrease OL reactivity with O_3 depending on their initial phase. OL reactivity in these binary mixtures

will then be contrasted with the reactivity of methyl oleate/SA mixtures to provide additional insight on the trapping mechanism.

4.3.1 Reaction kinetics of mixed particles

Selected decay curves for OL/SA and OL/MA mixtures are shown in Figure 4.2, and mixtures of OL/PA and OL/LA were similar to OL/SA and OL/MA, respectively. Two characteristics of the OL/SA and OL/MA decay curves warrant comment. First of all, the OL/SA mixtures show a significant slowing in the initial rate of reaction at low X_{OL} whereas the OL/MA mixtures show an increase in the initial rate. Second, the two lowest X_{OL} reaction decays for the OL/SA mixtures (X_{OL} = 0.27 and 0.12) appear to plateau leaving some or all of the OL unreacted at the highest exposure. We estimate that the OL in these trapped domains react at least 2 orders of magnitude slower than the untrapped domains. The lowest OL concentration (X_{OL} = 0.12) in the OL/SA mixtures actually shows an increase in the OL signal during the reaction. This may be due to a slight change in the OL sensitivity as the injector is pulled back, but this is only approximately a 5% shift in the signal. In contrast to the OL/SA mixtures, the OL/MA mixtures all react to completion.

Figure 4.3 shows the initial rate of reaction (panel A) and the fraction of trapped OL (panel B) for all mixtures studied. The plot of the initial rate of reaction clearly demonstrates the difference between the OL/SA and OL/PA mixtures and the OL/MA and OL/LA mixtures. A significant decrease in the initial rate of reaction is observed in the OL/SA and OL/PA mixtures, whereas the OL/MA and OL/LA mixtures show an increase in reactivity. Similarly, the OL/SA and OL/PA mixtures show significant trapping of OL at the lower X_{OL}, and the OL/MA and OL/LA mixtures trap no OL.

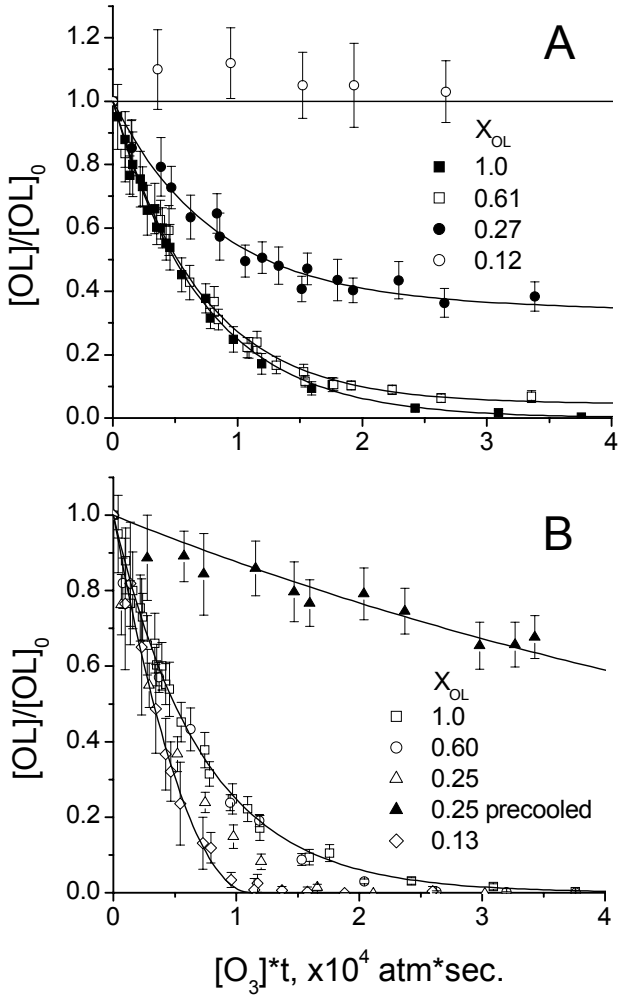

Figure 4.2. Reaction decays for (A) OL/SA mixtures and (B) OL/MA mixtures. SA slows the initial rate of reaction and eventually prevents the OL from reacting. MA causes an increase in reactivity, but when the particles are pre-cooled (closed triangles) the initial rate of reaction decreases by a factor of 12. Lines are drawn to guide the eye.

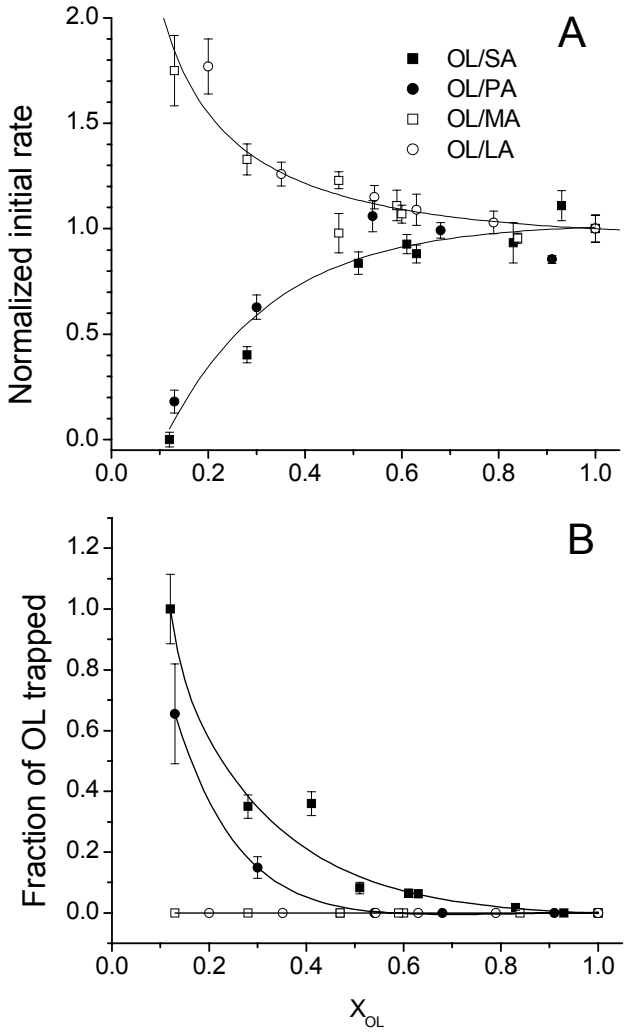

Figure 4.3. Summary of OL/alkanoic acid mixtures showing (A) the initial rate of reaction and (B) the fraction of OL trapped as a function of OL mole fraction. MA and LA cause an increase in the initial reactivity and trap no OL, but SA and PA do cause a decrease in OL reactivity and trap significant amounts of OL. Lines are drawn to guide the eye.

4.3.2 Initial reactivity and phase

The increase in reactivity of the OL/MA and OL/LA mixtures is unexpected since the phase diagram predicts that solid MA acid is present at $X_{OL} < 0.84$ (see Figure 4.1). In fact, resent results from Knopf et al. has shown an order of magnitude decrease in the

reactivity of ozone with OL when solid MA or LA was present [19]. We would then predict, according to the phase diagrams, to see a dramatic decrease in particle reactivity at $X_{OL} \leq 0.98$, 0.94, 0.84, and 0.58 for OL/ SA, PA, MA, and LA mixtures, respectively (see Figure 4.1). However, no such decrease in reactivity is observed for any of the mixtures at the predicted concentrations. Instead, we see a significant decrease in reactivity of OL/SA and OL/PA particles at $X_{OL} < 0.5$, far below the solubility limit of SA or PA in OL, and OL/MA and OL/LA mixtures react as if they had no solid present at all. The kinetics suggests that the mixed particles are supercooled liquid droplets and have not achieved thermodynamic equilibrium on the timescale of these experiments (particle age ≈ 1 minute).

Since the reactivity is not a direct measure of the phase of the particle constituents, we measured IR spectra of unreacted OL/MA and OL/SA internally mixed particles. These particles were generated by nebulizing a heated bulk mixture of the two components into a 10 cm long FTIR absorption cell. The IR spectrum was measured and the results are plotted in Figure 4.4. The two spectra are very similar but with two distinct differences. A peak at 1711 is shifted by 8.7 cm^{-1} to the red in the OL/SA mixture. This red shift is due to a change in the carbonyl stretch in solid SA. Additionally, peaks at 1180-1320 cm^{-1} show much more structure in the OL/SA mixture than in the OL/MA mixture. The resolved peaks in the OL/SA mixture are caused by increased ordering in solid SA. These results are consistent with previous observations of solid and liquid alkanoic acids [29] and provide an independent measure of the phase of the particles. We conclude from the FTIR spectra that OL/SA mixtures contain solid domains and the OL/MA mixtures are liquid.

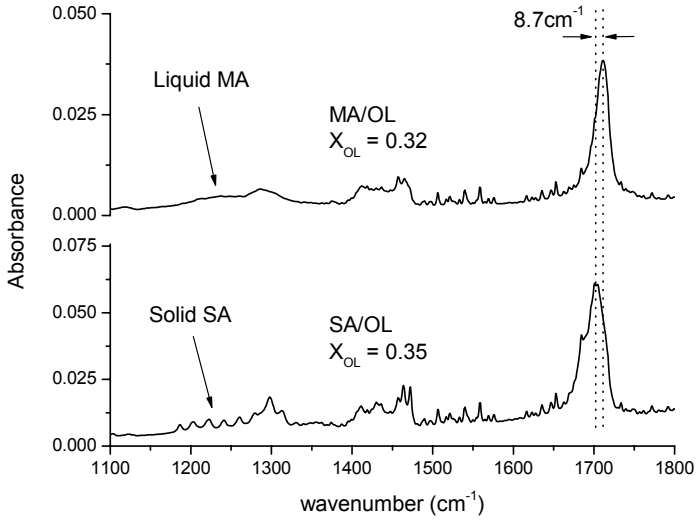

Figure 4.4. FTIR spectra of OL/MA and OL/SA particles. The structure observed from 1180 - 1320 cm^{-1} and the 8.7 cm^{-1} shift in the 1710 cm^{-1} band show that the OL/SA mixture is solid and the OL/MA mixture is liquid.

To test our conclusion that the OL/MA particles are indeed supercooled, we sent the particles through a cold trap (T = 0°C) and warmed them back to room temperature prior to reaction with O_3 in the flow tube. Cooling the particles increases the rate of nucleation and decreases the chance that the particles will remain supercooled [30]. The results are plotted in Figure 4.2B (solid triangles), and the initial rate of reaction of OL in the pre-cooled particles decreases by a factor of 12 relative to particles that were not pre-cooled. This corroborates the conclusion from kinetic analysis and the FTIR results that OL/MA particles are supercooled. The degree of supercooling can be estimated from the phase diagram (Figure 4.1) and the onset of the slowing of the initial rate (Figure 4.3). All OL/MA and OL/LA particles appear to be liquid since the initial rates of reaction for these mixtures do not decrease. The limits of supercooling for these mixtures are at least 31ºC and 17ºC for the OL/MA and OL/LA mixtures, respectively. OL/SA and OL/PA particles, on the other hand, do show significant slowing of the initial slope at $X_{OL} < 0.5$.

Investigation of the phase diagrams for these mixtures shows that the mixtures are supercooled by at most 32ºC and 34ºC for the OL/PA and OL/SA mixtures, respectively.

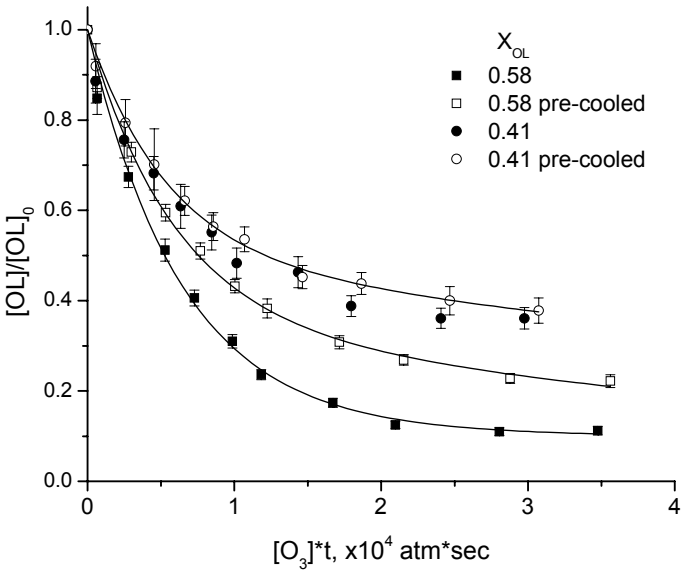

Figure 4.5. Reaction decay curves for OL/SA mixtures that were either pre-cooled to 0°C (open symbols) or kept at room temperature (closed symbols). At X_{OL} = 0.41 (circles), room temperature and pre-cooled particles have the same reactivity, but cooling particles with X_{OL} = 0.58 (squares) reduces particle reactivity. Lines are drawn to guide the eye.

To further corroborate our supercooling hypothesis of the OL/SA mixtures, we generated particles containing OL and SA and either cooled the particles to 0ºC and then warmed them to room temperature or kept them at room temperature before reacting the particles with ozone at 20ºC. Cooling the particles to 0ºC increases the rate of nucleation, so we would expect a larger fraction of the particles to contain solid domains. These solid domains will affect the reactivity of the particle, and there should be a change in the reactivity if the particles were initially supercooled. Figure 4.5 shows decay curves for particles with a composition of X_{OL} = 0.58 and 0.41 that were either cooled or not cooled before the reaction. Cooling the 58% mixture slows the reaction down, and in contrast to this mixture, the 41% mixture shows no significant difference between the cooled and

uncooled particles. These results are consistent with the hypothesis that the 58% mixture can be supercooled to room temperature whereas the 41% mixture cannot.

In addition to the slowing of the initial rate of reaction, there appears to be OL "trapped" by the solid alkanoic acids. The plateaus in the OL/SA reaction decay curves indicate that another kinetic regime exists in the particles where OL diffusion and/or O_3 solubility/ diffusion are much lower which slows the reaction. Particles containing OL and PA show similar behavior, and Figure 4.3B shows the fractional amount of OL left at long O_3 exposure as a function of OL mole fraction. This plot shows that for the same composition a larger fraction of OL is trapped in the OL/SA mixtures than in the OL/PA mixtures. This is consistent with the fact that for the same OL mole fraction, more SA than PA will precipitate out of solution, and SA, therefore, can trap a larger fraction of OL.

4.3.3 Effect of stearic acid on methyl oleate

It is unclear whether the trapping observed in the OL/SA and OL/PA mixtures is caused by the formation of a morphological feature such as a solid alkanoic acid shell or through the formation of a metastable solid. In order to better understand the mechanism of trapping, we reacted particles composed of stearic acid and methyl oleate (MO), the methyl ester of OL. MO lacks an acidic hydrogen and will interact less strongly with SA through hydrogen bonding thereby perhaps decreasing the probability of forming a metastable solid. Reaction decays of MO/SA mixtures are shown in Figure 4.6, and the results are in contrast to the OL/SA mixtures (see Figure 4.2A). All of the MO/SA mixtures react quickly and to completion. There is a slight decrease (≈ 25%) in reactivity

at $X_{MO} < 0.5$ in stark contrast to the OL/SA results which shows no detectable reaction at $X_{OL} = 0.12$.

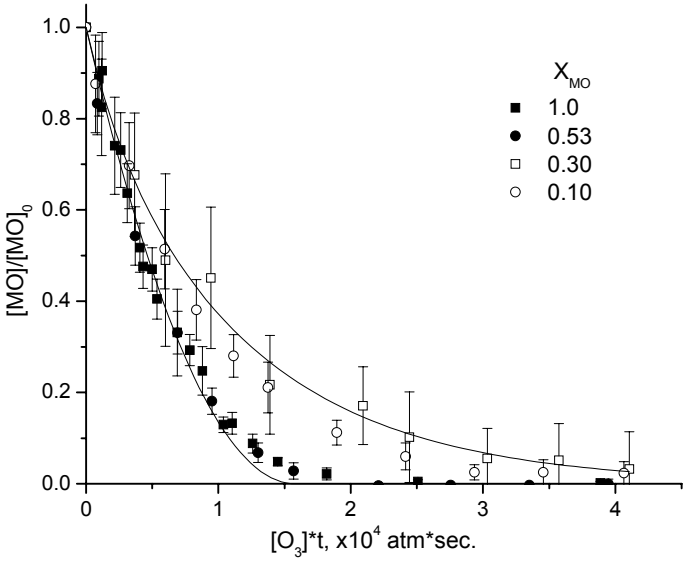

Figure 4.6. Reaction of MO/SA mixtures with O_3. Addition of SA slows the rate of reaction, but MO still reacts to completion. Lines are drawn to guide the eye.

To investigate this contrast between OL and MO more completely, a ternary mixture containing OL, MO, and SA (mole fractions 7:28:65) was generated via homogenous nucleation and reacted with ozone. Figure 4.7 shows the reaction decays for all three components in the aerosol, and the results are more consistent with the formation of a metastable solid. OL initially reacts quickly, but then it reaches a plateau with 70% OL remaining. MO, on the other hand, reacts quickly and to completion. If a solid SA shell was formed to inhibit the reaction of OL with O_3, we expect the reaction of MO with O_3 to also be inhibited. It seems unlikely, based on steric hindrance (no pun intended), that a solid SA shell would be permeable to MO and not to O_3. Instead, we believe a metastable solid is formed in which OL is trapped, and MO partitions to the liquid portions of the particle.

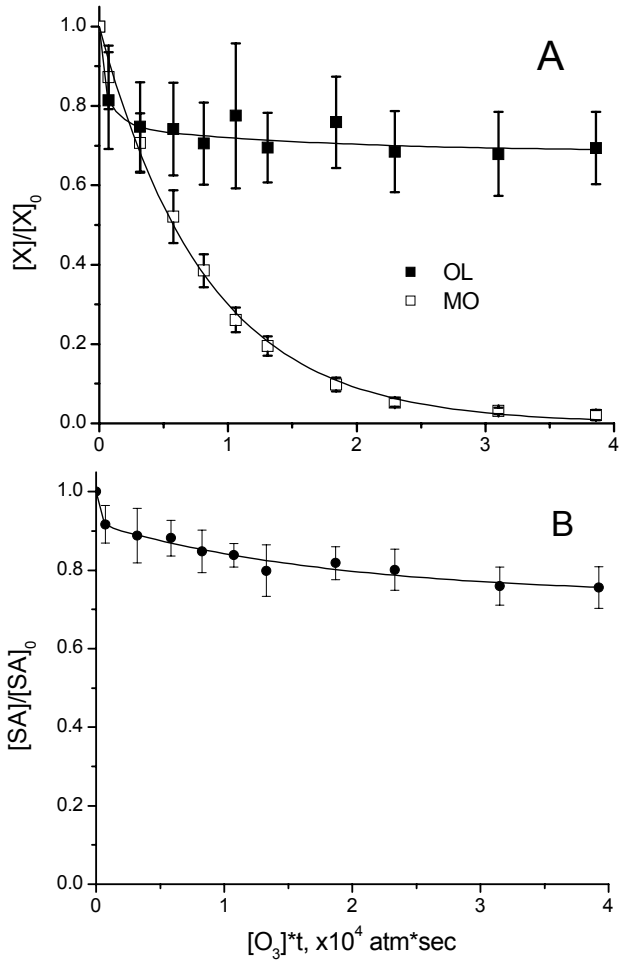

Figure 4.7. Reaction of internally mixed particles containing OL:MO:SA (7:28:65). (A) MO reacts quickly and to completion (open symbols), but OL is trapped (closed symbols). (B) SA reacts with the SCIs from the reaction of MO and O_3.

One other possible explanation is that the particles are not internally well mixed. This can be ruled out based on two pieces of evidence. First, OL is efficiently trapped, so it must be well mixed with SA, and second SA reacts significantly (see Figure 4.7B) with SCIs produced from the ozonolysis reaction. The magnitude of the OL reaction is large enough to generate enough SCIs to react away at most 3% of the SA signal, but a 25%

depletion is observed. This suggests that SA is well mixed with MO since the magnitude of the MO reaction is large enough to react up to 40% of the SA away.

Why, then, is OL trapped in the metastable solid and MO not? The only chemical difference between these two molecules is that MO has a methyl ester group where OL has a carboxylic acid group. At room temperature, OL exists almost exclusively (> 99%) as a dimer through hydrogen bonding of the carboxylic acid moieties [31, 32], and is therefore twice as long as the monomer. Also, when the vapors condense to form particles, heterodimers may form between OL and SA or PA [33]. MO, on the other hand, is not expected to form dimers since it lacks the acid group. These properties of OL may facilitate the formation of a metastable solid with SA or PA since SA and PA also exist as dimers and the OL dimer unit or the OL-SA or OL-PA heterodimer unit may pack between the SA and PA dimers more easily than the MO monomer. The smaller MO monomer may not pack between the alkanoic acid dimer units easily, preventing it from getting trapped in a metastable solid. Therefore, it appears as if the acid moiety of OL and/or the size of the dimer unit must aid in the trapping of OL.

Knopf et al. saw increased ozone reactivity as a function of film age when solid MA was present [19] which would be consistent with the formation of a metastable solid. Over time, the solid would relax to the thermodynamic equilibrium of liquid OL/MA solution and solid MA, and as the OL partitioned to the liquid domains, the reactivity would increase. Ziemann has also reacted polydisperse OL/PA (10:90) particles with ozone, and he saw two kinetic regimes. The particles initially reacted very quickly, and then reached a plateau once 30-40% of the OL was left [22]. This qualitatively agrees

with our data, though we see twice as much OL trapped, possibly a result of the particle generation technique (evaporation of solvent vs. homogenous nucleation).

4.4 Oleic acid – docosane mixtures

The binary OL – alkanoic acid mixtures were used as simple proxies for meat cooking aerosol. The presence of solid alkanoic acid slows down the initial rate of the OL ozonolysis reaction, and it can effectively stop the reaction on the timescale of our experiments. However, automobile and diesel emissions have much higher alkane concentrations [6], so in an effort to better understand the reactivity of such particles we measured the reactivity of model particles composed of OL and docosane (DO). Docosane is a saturated linear hydrocarbon that has been identified in diesel exhaust [6], and it shows some aberrant effects on OL reacitivy.

4.4.1 OL/DO phase diagram

In order to have a complete understanding of the effects DO has on OL reactivity, we measured the phase diagram using a differential scanning calorimeter. Figure 4.8 shows a plot of the heat flow as a function of temperature for two different OL/DO mixtures. Scans were done with a constant temperature ramp (+5°C/min.) while measuring the heat flow. Two peaks are observed in the plots. The lower temperature peak corresponds to the melting of OL, and the higher temperature peak corresponds to the melting of DO. Scans like this were measured for 11 different OL/DO mixtures ($0 < X_{DO} < 1$), and as demonstrated in Figure 4.8A, the OL melting point remains fixed, and the DO melting point changes with mole fraction.

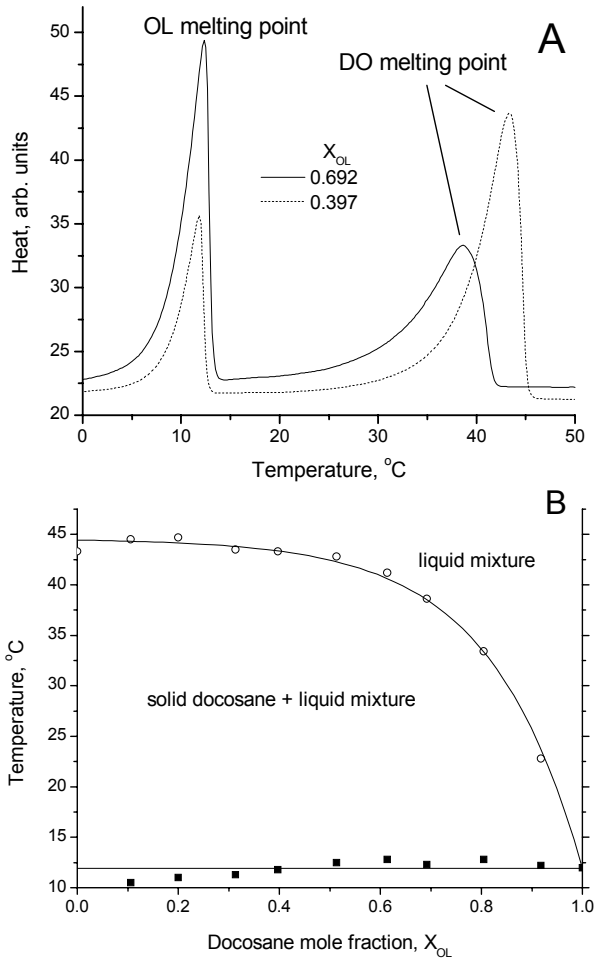

Figure 4.8. (A) DSC measurements for 2 OL/DO mixtures showing two peaks for the melting of OL and DO. (B) Phase diagram for the binary mixture of OL/DO showing a biphasic region composed of solid DO and a liquid mixture and a liquid mixture region above the liquidous line.

The phase diagram for bulk mixtures of OL/DO is plotted in Figure 4.8B. This is very similar to the phase diagrams for oleic acid-alkanoic acid mixtures [27, 28, 34] where a liquid mixture exists above the liquidous line and a biphasic mixture composed of the liquid solution and solid DO exists below it. At temperatures below 12ºC, the mixture is solid. I would like to emphasize that the phase diagram represents the

thermodynamic equilibrium and particles may not have sufficient time to reach equilibrium during the timescale of these experiments (particle age ≈ 1 minute), but this provides a reference point for analysis of the data presented below.

4.4.2 OL/DO mixture reactivity

Figure 4.9A shows the reaction decay of OL in OL/DO mixtures, and these mixtures show a drastically different reactivity than the alkanoic acid mixtures. Particles composed of mostly OL (X_{OL} = 0.97) react quickly and to completion. At X_{OL} = 0.87, DO does not affect the initial slope, but a large fraction of OL (40%) is trapped. At X_{OL} = 0.63, very little OL reacts at all, and at X_{OL} = 0.32, OL reactivity is restored to a level slower than pure OL. This restoration of OL reactivity is unexpected since the phase diagram predicts more solid DO as X_{OL} is decreased. However, as pointed out above, the phase diagram is for thermodynamic equilibrium, and particles may not have reached equilibrium on the timescale of these experiments.

Results from additional experiments are shown in panels B and C of Figure 4.9. Panel B shows the initial rate of reaction as a function of OL mole fraction, and it is clear that the observations from the decay curves (panel A) are reproducible. Panel C shows the fraction of OL that is trapped as a function of X_{OL}. The data at $X_{OL} \leq 0.55$ has 100% uncertainty on the lower error bars because the OL signal was still decreasing at the highest exposure, so these represent upper bounds on the amount of trapped OL. The initial rate of reaction is unaffected by the presence of DO when $X_{OL} > 0.8$, whereas the fraction of trapped OL increases almost linearly from 0 to 100% from $0.7 < X_{OL} < 1.0$. This suggests that the products from the ozonolysis of OL induce trapping of OL, but the products alone are not sufficient to trap OL as pure OL particles react to completion. DO

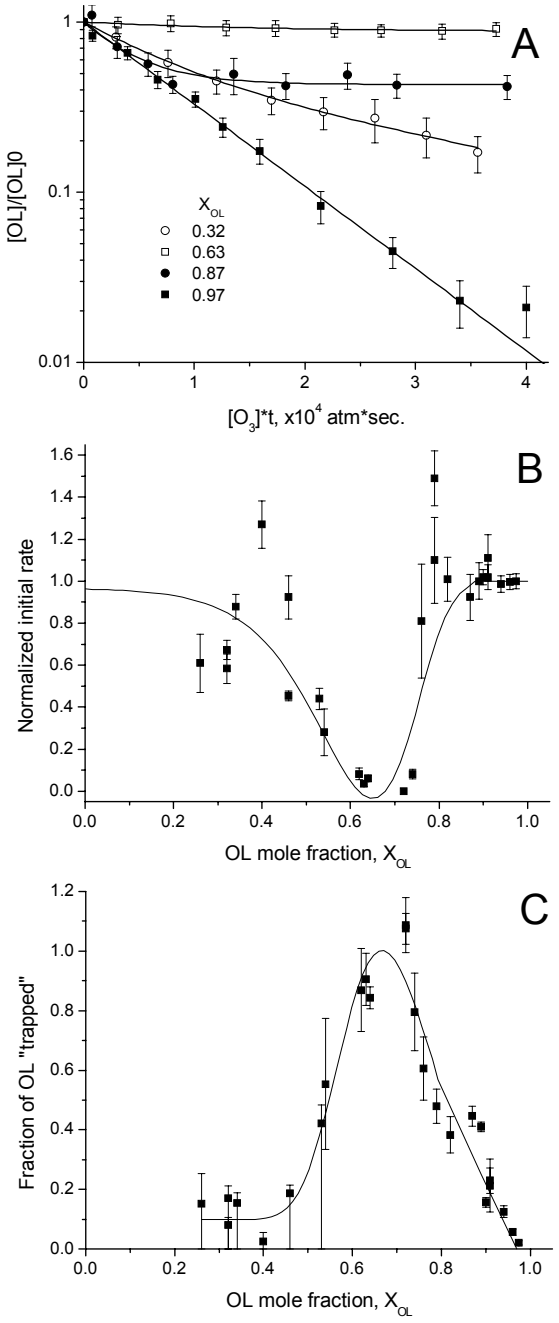

Figure 4.9. Reaction of OL/DO particles showing (A) selected reaction decay curves, (B) initial rate of reaction as a function of X_{OL}, and (C) fraction of OL trapped as a function of X_{OL}. Initial reactivity decreases and then increases and the fraction trapped increases and decreases as more DO is added. Lines are drawn to guide the eye.

may facilitate nucleation of solid OL ozonolysis products (e.g. azelaic acid and 9-oxononanoic acid). At $X_{OL} < 0.6$, the initial reactivity is partially restored and the trapping is reduced if not absent. This unexpected behavior indicates that the bulk phase diagram does not accurately describe the particles. Particles composed of MO/DO exhibited the same behavior as OL suggesting that the mechanism of trapping in these particles is different than in the alkanoic acid mixtures (data not shown).

In addition to these kinetic measurements, particles were pre-cooled and warmed back up to room temperature before reaction as described in section 4.3.2. Figure 4.10 shows the reaction decays for OL/DO particles with $X_{OL} = 0.72$ that were either not cooled (20°C) or precooled to 15°C, 11.5°C, or 0°C before reaction. Particles not cooled (20°C) or pre-cooled to 15°C showed no reactivity to O_3 over the exposure range of our experiment. Surprisingly, reactivity was restored in particles cooled to 11.5 and 0°C, and OL in these particles reacted to completion. Figure 4.10B shows the initial rate as a function of the pre-cooling temperature to illustrate the restoration of reactivity.

Figure 4.11 shows the reaction of OL/DO particles with $X_{OL} = 0.89$ (panel A) and 0.40 (panel B) that were pre-cooled to 0°C or kept at 20°C. At $X_{OL} = 0.89$, the particles that were not cooled show fast initial reactivity followed by an abrupt halt in the reaction, consistent with a product-induced trapping of OL. Particles that were pre-cooled show slower initial reactivity, and unlike the un-cooled particles, OL continues to react to the largest O_3 exposure. At $X_{OL} = 0.40$, there is no significant difference between the particles that were pre-cooled and those that were not, and this is consistent with the presence of solid DO in these particles at room temperature (20°C).

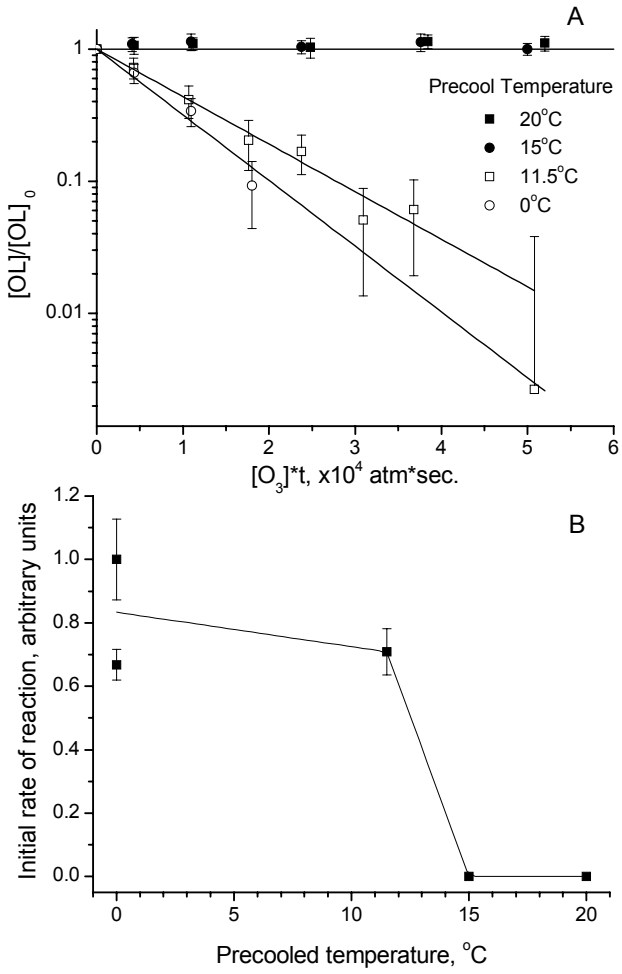

Figure 4.10. Reaction of OL/DO particles (X_{OL} = 0.72) pre-cooled to different temperatures before reaction. (A) The reaction decays of OL where OL is trapped in particles cooled to > 15°C and available for reaction when the particles are cooled to < 11.5°C. (B) The normalized initial rate of reaction as a function of pre-cooling temperature. Lines are drawn to guide the eye.

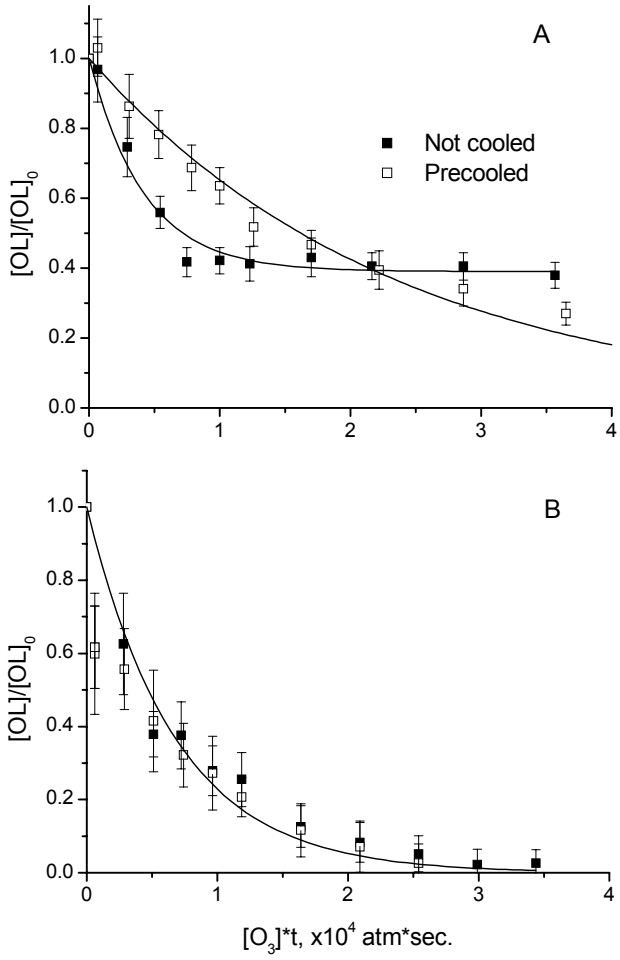

Figure 4.11. Reaction decay curves for OL/DO mixtures with an OL mole fraction of (A) 0.89 and (B) 0.40 that were either pre-cooled to 0°C (open squares) or kept at room temperature (closed squares). At $X_{OL} = 0.89$, particles that were pre-cooled show slower initial reactivity, but there is no indication that the reaction has stopped. There is no difference between the room temperature and pre-cooled particles in the $X_{OL} = 0.40$ particles. Lines are drawn to guide the eye.

4.4.3 OL/DO discussion

There are at least two, possibly three, operative mechanisms that explain the OL/DO results. First, notice that the initial rate of reaction is constant at $X_{OL} > 0.8$ and the fraction of OL trapped increases linearly over this range. The fast initial reactivity along with the precooling results suggest the particles are initially liquid at $X_{OL} > 0.8$, but this is inconsistent with the observed trapping. Over this composition range, we conclude

that the particles are initially liquid, but the products from the reaction induce nucleation of solid domains that trap the unreacted OL. This would only require a modest degree of supercooling (≈ 15°C) which is consistent with the results from the OL/alkanoic acid mixtures and observations of bulk alkanes [14, 35, 36]. When these particles are pre-cooled, DO is precipitated out of solution before the reaction and while the reactivity is reduced, OL is not trapped. Apparently, simultaneous precipitation of the ozonolysis products and DO is required for efficient trapping of OL.

Second, in the composition range between $0.6 < X_{OL} < 0.75$, there is little or no observed reaction. The products could induce nucleation here also, but two pieces of evidence suggest that products are not initiating nucleation. (1) There is very little reaction to generate a large amount of products, and (2) the initial rate of reaction is not consistent with liquid particles. Another possible explanation for the reactivity of this composition range is that DO is forming a surface frozen layer that is impenetrable to both O_3 and OL. Surface freezing of single component alkanes and binary mixtures of alkanes has been observed for many years [37-39], and recently it has been shown that long chain alcohols exhibit this behavior [40, 41]. It is conceivable, then, that particles composed of OL/DO behave in a similar way. Surface frozen layers in binary mixtures require a minimum amount of the solid component ($X_{\text{solid component}} \approx 0.3$) before a frozen surface can form, and it is only operative over a narrow range of compositions at a given temperature. Additionally, surface frozen layers are only formed by cooling a mixture, so further cooling to initiate bulk crystallization and subsequent warming would not reform the frozen surface.

These characteristics of surface freezing corroborate the conclusion that a surface frozen layer forms in OL/DO particles over a narrow composition range at room temperature ($0.6 < X_{OL} < 0.75$) which stops the OL + O_3 reaction. Cooling particles in this composition range restores reactivity because solid domains in the particle are formed and the surface frozen layer does not reform when the particles are warmed back to room temperature. The results from MO/DO mixtures (data not shown) corroborate this conclusion since the formation of a solid surface layer would affect MO and OL reactivity equally.

Third, at $X_{OL} < 0.6$ the particles enter into the biphasic region of the phase diagram and the surface frozen layer is lost. This restores particle reactivity because the surface frozen layer is lost. Bulk solid DO may slow OL or O_3 diffusion, so the initial reactivity does not necessarily recover completely. Cooling particles within this composition range (e.g. Figure 4.11B) does not affect their reactivity because their phase is unaffected.

4.5 Reactivity of Hamburger Aerosol

While the binary mixtures discussed above provide some helpful insight into the reactivity of biphasic particles, they do not completely address how real particles will react. Binary mixtures are still a long way from accurately representing real particles that have hundreds of components. Since OL is a primary condensed phase meat cooking emission [1, 2] one relevant test is to react meat cooking aerosol with O_3. Meat cooking aerosol was generated by frying ground beef in a glass beaker above a Bunsen burner flame. The aerosol was sampled into an evacuated 500 mL flask and stored. A small flow of N_2 (≈ 10 sccm) swept out the particles into the injector flow (190 sccm) and into

the flow tube for reaction with O_3. The reaction was monitored as described in section 3.3 since the particle signal was slowly decaying over time. Figure 4.12A shows a mass spectrum of the meat cooking aerosol where the large peak at m/z = 283 corresponds to protonated OL. Other major emissions from meat cooking at m/z = 257, 255, 229, 187, 173, 159, and 145 were detected and correspond to palmitic acid, palmitoleic acid, myristic acid, decanoic acid, octanoic acid, nonanoic acid, and pentanoic acid, respectively. Groups of peaks can be seen every ≈ 14 amu, indicative of functionalized organics with additional $-CH_2-$ groups.

Figure 4.12B shows the normalized signal at m/z = 283 as a function of O_3 exposure showing a fast kinetic regime followed by a slow kinetic regime where approximately 30% of the signal at m/z = 283 is not reactive. Since the concentration of OL is unknown in these particles and the size distribution is polydisperse, the reaction can only be used for qualitative analysis. However, it does show that in "real" particles, part of the OL can be effectively trapped by other components in the particles. This non-reactive OL will have a lifetime of several hours to days in a polluted atmosphere (100 ppb). The top x-axis in Figure 4.12B shows the equivalent reaction time of these particles in a polluted atmosphere, and it shows that the untrapped OL reacts away in 0.4 hours whereas no detectable decrease is observed beyond this time.

The 30% remaining signal at m/z = 283 could be a contribution from another component. In fact, 5-tetradecyldihydro-2(3H)-furanone (m.w. = 282 amu) has been measured from meat cooking emissions [1], but it would only account for 2% of the signal at m/z = 283. There also could be unidentified contribution to the signal, but we expect OL to be the dominant contributor to m/z = 283.

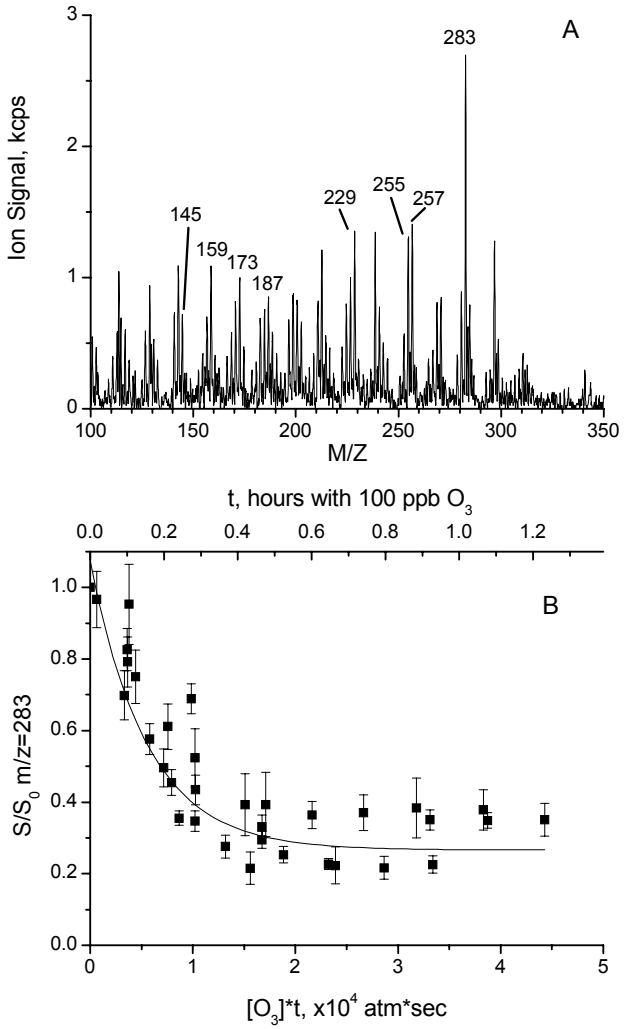

Figure 4.12. (A) Mass spectrum of hamburger aerosol using proton transfer ionization. Labeled peaks are identified in the text. (B) Reaction of hamburger aerosol with O_3 showing the normalized decay of oleic acid (m/z = 283). Part of the OL reacts quickly, and the remaining 30% is trapped by solid components in the particles. The top x-axis shows the corresponding reaction time in a polluted atmosphere (100 ppb O_3). The line is drawn to guide the eye.

4.6 Conclusion and Atmospheric Implications

Atmospheric particles are multicomponent mixtures, and this complicates kinetics of heterogeneous reactions. Here we have taken a step toward understanding reactivity of internally mixed particles representative of meat cooking emissions (alkanoic acid mixtures) and diesel exhaust (docosane mixtures). Trapping of particle constituents can be achieved through the addition of a solid alkanoic acid component to the particle, but it can be prevented through supercooling. We have found that organic particles containing alkanoic acids can be supercooled by as much as 34ºC. Supercooled organic particles have not yet been observed in the atmosphere, but they may exist since some particles are generated from condensation of heated organic vapor (e.g. meat cooking), similar to what we have used here to generate our particles. However, since supercooled particles would be much more reactive than their solid counterparts, and since oleic acid has a relatively long lifetime in the atmosphere (days), it is likely that if these particles are supercooled, they will quickly solidify.

The results from the OL/DO mixtures does not appear to be consistent with the bulk phase diagram, and caution should be employed when extrapolating from bulk thermodynamic measurements to particle phases. The aberrant behavior of the OL/DO mixtures is attributed to reaction-induced nucleation and surface freezing. A frozen surface layer protects the interior of the particle from oxidation by O_3, but this layer only exists over a narrow range of compositions and temperature. Once the frozen surface layer is compromised by either cooling the particles or increasing the concentration of DO, reactivity is restored suggesting that bulk solid DO alone does not efficiently trap OL. Therefore, morphological effects may play a role in particle reactivity, and these

features of particles are not adequately described by bulk phase diagrams. While these conclusions about OL/DO mixtures are consistent with the results obtained here, they still need to be verified by an independent measure of particle morphology and phase.

In addition to these simple proxies for organic aerosol, we reacted meat cooking emissions with O_3 and found that a significant amount of OL (≈ 30%) is non-reactive with O_3, consistent with solid constituents trapping OL. Most of the OL was reactive with O_3, and this suggests that in the atmosphere there will be a fast reaction that oxidizes a significant portion of the particle, but much of the particle is protected. Upon nucleation of the solid constituent (either through pre-cooling or reaction), we have observed changes in oleic acid reactivity of more than one order of magnitude.

References

1. Rogge, W.F., et al., *Sources of Fine Organic Aerosol .1. Charbroilers and Meat Cooking Operations.* Environmental Science & Technology, 1991. **25**(6): p. 1112-1125.

2. He, L.Y., et al., *Measurement of emissions of fine particulate organic matter from Chinese cooking.* Atmospheric Environment, 2004. **38**(38): p. 6557-6564.

3. McDonald, J.D., et al., *Emissions from charbroiling and grilling of chicken and beef.* Journal of the Air & Waste Management Association, 2003. **53**(2): p. 185-194.

4. Rogge, W.F., et al., *Sources of fine organic aerosol. 9. Pine, oak and synthetic log combustion in residential fireplaces.* Environmental Science & Technology, 1998. **32**(1): p. 13-22.

5. Simoneit, B.R.T., et al., *Levoglucosan, a tracer for cellulose in biomass burning and atmospheric particles.* Atmospheric Environment, 1999. **33**(2): p. 173-182.

6. Rogge, W.F., et al., *Sources of Fine Organic Aerosol .2. Noncatalyst and Catalyst-Equipped Automobiles and Heavy-Duty Diesel Trucks.* Environmental Science & Technology, 1993. **27**(4): p. 636-651.

7. Finlayson-Pitts, B.J. and J.N.J. Pitts, *Chemistry of the Upper and Lower Atmosphere*. 2000, San Diego, CA: Academic Press. 969.

8. Katrib, Y., et al., *Density changes of aerosol particles as a result of chemical reaction.* Atmospheric Chemistry and Physics, 2005. **5**: p. 275-291.

9. Demou, E., et al., *Uptake of water by organic films: the dependence on the film oxidation state.* Atmospheric Environment, 2003. **37**(25): p. 3529-3537.

10. Broekhuizen, K.E., et al., *Formation of cloud condensation nuclei by oxidative processing: Unsaturated fatty acids.* Journal of Geophysical Research-Atmospheres, 2004. **109**(D24): p. -.

11. Moise, T. and Y. Rudich, *Reactive Uptake of Ozone by Aerosol-Associated Unsaturated Fatty Acids: Kinetics, Mechanism, and Products.* Journal of Physical Chemistry A, 2002. **106**: p. 6469-6476.

12. Smith, G.D., et al., *Aerosol uptake described by numerical solution of the diffusion - Reaction equations in the particle.* Journal of Physical Chemistry A, 2003. **107**(45): p. 9582-9587.

13. Zahardis, J., B.W. LaFranchi, and G.A. Petrucci, *Direct observation of polymerization in the oleic acid-ozone heterogeneous reaction system by photoelectron resonance capture ionization aerosol mass spectrometry.* Atmospheric Environment, 2006. **40**(9): p. 1661-1670.

14. Thornberry, T. and J.P.D. Abbatt, *Heterogeneous reaction of ozone with liquid unsaturated fatty acids: detailed kinetics and gas-phase product studies.* Phys. Chem. Chem. Phys., 2004. **6**: p. 84-93.

15. Nash, D.G., M.P. Tolocka, and T. Baer, *The uptake of O-3 by myristic acid-oleic acid mixed particles: evidence for solid surface layers.* Physical Chemistry Chemical Physics, 2006. **8**(38): p. 4468-4475.

16. Asad, A., B.T. Mmereki, and D.J. Donaldson, *Enhanced uptake of water by oxidatively processed oleic acid.* Atmospheric Chemistry and Physics, 2004. **4**(8): p. 2083-2089.

17. Zahardis, J., B.W. LaFranchi, and G.A. Petrucci, *Photoelectron resonance capture ionization-aerosol mass spectrometry of the ozonolysis products of oleic acid particles: Direct measure of higher molecular weight oxygenates.* Journal of Geophysical Research-Atmospheres, 2005. **110**(D8): p. -.

18. Katrib, Y., et al., *Products and mechanisms of ozone reactions with oleic acid for aerosol particles having core-shell morphologies.* Journal of Physical Chemistry A, 2004. **108**(32): p. 6686-6695.

19. Knopf, D.A., L.M. Anthony, and A.K. Bertram, *Reactive uptake of O-3 by multicomponent and multiphase mixtures containing oleic acid.* Journal of Physical Chemistry A, 2005. **109**(25): p. 5579-5589.

20. Hearn, J.D. and G.D. Smith, *Measuring rates of reaction in supercooled organic particles with implications for atmospheric aerosol.* Physical Chemistry Chemical Physics, 2005. **7**(13): p. 2549-2551.

21. Hearn, J.D., A.J. Lovett, and G.D. Smith, *Ozonolysis of oleic acid particles: evidence for a surface reaction and secondary reactions involving Criegee intermediates.* Physical Chemistry Chemical Physics, 2005. **7**(3): p. 501-511.

22. Ziemann, P.J., *Aerosol products, mechanisms, and kinetics of heterogeneous reactions of ozone with oleic acid in pure and mixed particles.* Faraday Discussions, 2005. **130**: p. 469-490.

23. Morris, J.W., et al., *Kinetics of submicron oleic acid aerosols with ozone: A novel aerosol mass spectrometric technique.* Geophysical Research Letters, 2002. **29**(9): p. -.

24. Hearn, J.D. and G.D. Smith, *Kinetics and product studies for ozonolysis reactions of organic particles using aerosol CIMS.* Journal of Physical Chemistry A, 2004. **108**(45): p. 10019-10029.

25. Smith, G.D., et al., *Reactive uptake of ozone by oleic acid aerosol particles: Application of single-particle mass spectrometry to heterogeneous reaction kinetics.* Journal of Physical Chemistry A, 2002. **106**(35): p. 8085-8095.

26. Zahardis, J. and G.A. Petrucci, *The oleic acid-ozone heterogeneous reaction system: products, kinetics, secondary chemistry, and atmospheric implications of a model system – a review.* Atmospheric Chemistry and Physics, 2006. **6**(6): p. 11093-11179.

27. Inoue, T., et al., *Solid-liquid phase behavior of binary fatty acid mixtures 2. Mixtures of oleic acid with lauric acid, myristic acid, and palmitic acid.* Chemistry and Physics of Lipids, 2004. **127**(2): p. 161-173.

28. Inoue, T., et al., *Solid-liquid phase behavior of binary fatty acid mixtures 1. Oleic acid stearic acid and oleic acid behenic acid mixtures.* Chemistry and Physics of Lipids, 2004. **127**(2): p. 143-152.

29. Zhang, J.J., et al., *Thermal studies on the solid-liquid phase transition in binary systems of fatty acids.* Thermochimica Acta, 2001. **369**(1-2): p. 157-160.

30. Kelton, K.F., *Crystal Nucleation in Liquids and Glasses.* Solid State Physics-Advances in Research and Applications, 1991. **45**: p. 75-177.

31. Iwahashi, M., et al., *Self-Association of Cis-9-Octadecen-1-Ol in the Pure Liquid-State and in Decane Solutions as Observed by Viscosity, Self-Diffusion, Nuclear-Magnetic-Resonance, Electron-Spin-Resonance, and near-Infrared Spectroscopic Measurements.* Journal of Physical Chemistry, 1995. **99**(12): p. 4155-4161.

32. Iwahashi, M., et al., *Dissociation of Dimeric Cis-9-Octadecenoic Acid in Its Pure Liquid-State as Observed by near-Infrared Spectroscopic Measurement.* Journal of Physical Chemistry, 1993. **97**(13): p. 3129-3133.

33. Clague, D. and A. Novak, *Far Infrared Spectra of Homogeneous and Heterogeneous Dimers of Some Carboxylic Acids.* Journal of Molecular Structure, 1970. **5**(1-2): p. 149-&.

34. Inoue, T., et al., *Solid-liquid phase behavior of binary fatty acid mixtures 3. Mixtures of oleic acid with capric acid (decanoic acid) and caprylic acid (octanoic acid).* Chemistry and Physics of Lipids, 2004. **132**(2): p. 225-234.

35. Hotta, Y., R. Hiraoka, and T. Yamaoka, *Effect of particle size and polarity of long-chain molecules in polymeric films on the supercooling temperature.* High Performance Polymers, 1997. **9**(4): p. 369-383.

36. Sirota, E.B., *Supercooling and transient phase induced nucleation in n-alkane solutions.* Journal of Chemical Physics, 2000. **112**(1): p. 492-500.

37. Sloutskin, E., et al., *Surface freezing of chain molecules at the liquid-liquid and liquid-air interfaces.* Faraday Discussions, 2005. **129**: p. 339-352.

38. Sloutskin, E., et al., *Surface freezing in n-alkane solutions: The relation to bulk phases.* Physical Review E, 2001. **6403**(3): p. -.

39. Tkachenko, A.V. and Y. Rabin, *Theory of surface freezing of alkanes.* Physical Review E, 1997. **55**(1): p. 778-784.

40. Sloutskin, E., et al., *Surface freezing in binary mixtures of chain molecules. II. Dry and hydrated alcohol mixtures.* Physical Review E, 2003. **68**(3): p. -.

41. Sloutskin, E., et al., *Surface and bulk phase behavior of dry and hydrated tetradecanol : octadecanol alcohol mixtures.* Journal of Chemical Physics, 2002. **116**(18): p. 8056-8066.

CHAPTER 5

A RELATIVE RATES APPROACH TO MEASURING HETEROGENEOUS REACTION KINETICS[1]

5.1 Introduction

In Chapter 3, A-CIMS was used to investigate the reactions between ozone and particles composed of oleic acid or methyl oleate as representative reactions of unsaturated organics [1, 2]. However, many organic molecules lack a double bond and will not be reactive with ozone [3], so their chemical lifetimes will be dependent on other reactive gases such as the hydroxyl radical (OH). In fact, OH is the primary oxidant in the troposphere [4], so it is imperative to understand how quickly radical-initiated reactions chemically transform organic particles to have a more complete model of particle evolution.

Some work has been done on radical-initiated heterogeneous oxidation of organic surfaces and particles [5-10]. Uptake measurements show that OH and Cl reactions are fast ($\gamma > 0.1$) [5, 6, 10], but this is only the gas phase radical loss on organic surfaces. These measurements, while important, do not necessarily describe the rate of loss of the condensed phase species. Auto-oxidation reactions involving unsaturated or substituted organic molecules are known to proceed through radical chain mechanisms [11], so the rate of oxidation of an organic particle could be much higher than the OH or Cl uptake

[1] Hearn, J.D. and G.D. Smith, A mixed-phase relative rates technique for measuring aerosol reaction kinetics. Geophysical Research Letters, 2006. **33**(17): p. L17805. Reproduced in part with permission of the publisher.

coefficients predict. Radical-initiated oxidation is propagated through peroxy or alkoxy radicals abstracting a hydrogen atom and forming another alkyl radical. The propagation step is rather slow for hydrogen abstraction from a secondary carbon [12], but if tertiary carbons, carbon-carbon double bonds, or functional groups are present, radical chains can be much longer [11].

For a complete picture of oxidation of organic aerosol, reliable kinetic data on the condensed phase species is needed. Absolute rate measurements are cumbersome because the gas phase reactant concentration and reaction time need to be accurately known. This is not a problem for ozone initiated reactions because ozone can be generated in high, measurable concentrations, but radical concentrations are difficult to measure. To circumvent these problems we have developed a mixed phase relative rates approach to measuring heterogeneous reaction kinetics, similar to gas phase relative rates measurements. In this approach, a gas phase reference compound that reacts with the gas phase reactant (O_3, OH, or Cl) is used as a "clock" for the reaction. The normalized reaction decay of the gas phase reference compound can be related to the exposure using the rate law as long as the rate constant for the reaction is known. This removes the need for an independent measure of the gas phase reactant concentration and the reactant time, and radicals can have a transient concentration in the flow tube.

A-CIMS is well suited for mixed phase relative rates measurements because it detects both gas and condensed phase species simultaneously. As a verification of this technique, we measured the rate of loss of methyl oleate (MO) normalized to the ozone-particle collision rate (γ_{MO}) using a gas phase reference compound (2-methyl-2-butene). These results are compared with the absolute measurements made in Chapter 3, and this

approach proves to be reliable in measuring heterogeneous reactions. Then we used this technique to measure the heterogeneous kinetics of OH and Cl radicals with particles composed of bis-(ethylhexyl) sebacate (dioctyl sebacate, DOS), and the evidence strongly suggests the presence of radical chain mechanisms.

5.2 Materials and Methods

Monodisperse particles (geometric standard deviation < 1.2) for radical-initiated reactions were generated by heterogeneous nucleation as described in section 2.6. For the ozonolysis experiments, methyl oleate particles were generated by direct nebulization of the pure organic and size selected with a differential mobility analyzer as described in section 2.6. Particle diameters were 100-200 nm for radical-initiated reactions and 750 – 950 nm for ozonolysis reactions. The mixed phase relative rates experiments were carried out at atmospheric pressure in a glass flow tube, and the generated aerosol particles, gas phase reference compound, and gas phase reactant were introduced into the front of the flow tube with a total flow of 2 slpm resulting in an average reaction time of approximately 3 seconds (see Figure 5.1). Ozone was generated, stored, and measured as described in section 3.2. Chlorine radicals were generated by photodissociation of Cl_2 ($[Cl_2] \approx 10^{14}$ molecule/cm^3) in the flow tube using 355 nm light (third harmonic) [13] from a 10 Hz pulsed Nd:YAG laser (Quanta-Ray PRO-250, Spectra-Physics). The Cl radical concentration (and thus the exposure) was varied by increasing the power of the laser to a maximum of 100 mJ/pulse over 3-4 minutes allowing rapid collection of entire decay traces. OH was generated according to reactions (5.1) and (5.2) by photodissociation of O_3 into $O(^1D)$ and O_2 with the fourth harmonic from a 10 Hz pulsed

Nd:YAG laser (λ = 266 nm) [14, 15]. $O(^1D)$ reacted with water in the flow tube to generate 2 OH radicals:

$$O_3 + h\nu \rightarrow O(^1D) + O_2 \quad (5.1)$$

$$O(^1D) + H_2O \rightarrow 2OH \quad (5.2)$$

Unfortunately, there are additional reactions in this scheme for OH production that deplete the OH concentration and generate byproducts such as HO_2 and H_2O_2:

$$OH + OH \rightarrow H_2O_2 \quad (5.3)$$

$$OH + O_3 \rightarrow HO_2 + O_2 \quad (5.4)$$

However, OH is regenerated through reaction of HO_2 with O_3:

$$HO_2 + O_3 \rightarrow OH + 2O_2 \quad (5.5)$$

This approach to generating OH is similar to previously published work [16], and the OH concentration was also varied by changing the laser power to a maximum of 1.2 mJ/pulse. Because of the reactive nature of OH and Cl radicals, high concentrations cannot be achieved or maintained with a point source (microwave cavity, corona discharge, etc.). Therefore, the laser light was aligned along the axis of the flow tube so that radical generation was maintained for the entire length. This experimental set-up produced an exposure over two orders of magnitude larger than a point source would have achieved.

Gases and chemicals used were Acetone (Certified ACS grade, Fisher Scientific), bis (2-ethylhexyl) sebacate (DOS, > 97%, Fluka, further purified in the laboratory), hexanal (98%, Aldrich), methyl oleate (99%, Aldrich), 2-methyl-2-butene (95%, Acros), hexanes (99.6%, J. T. Baker), N_2 (99.99%, National Welders), O_2 (99.99%, National Welders), and Cl_2 (UHP grade, Airgas). Flows were measured and maintained using

mass flow controllers (MKS). DOS was purified of semivolatile impurities by heating a small aliquot of liquid and evacuating the sample to less than 10 mTorr.

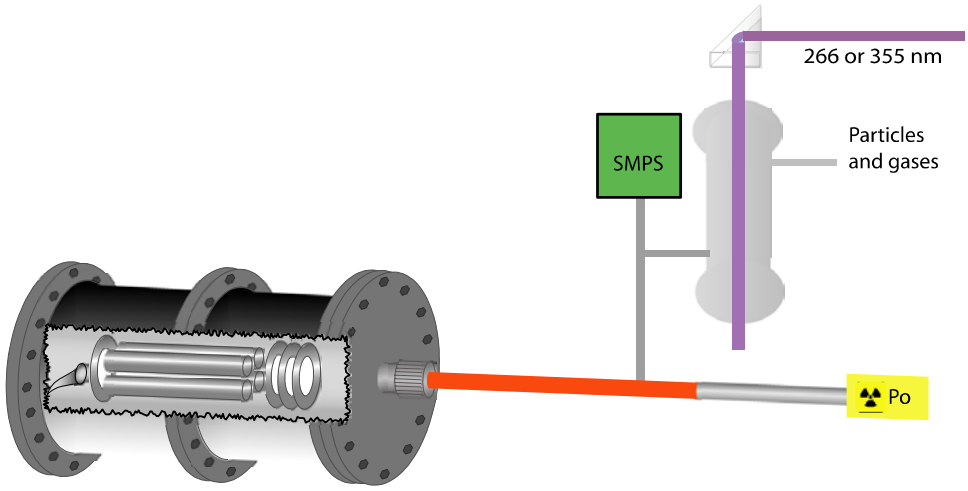

Figure 5.1. Schematic of experimental set-up for relative rate measurements.

5.3 Results

In the following sections, I will first verify that the mixed phase relative rates approach can be used to measure heterogeneous reaction kinetics, then I will use this technique to measure kinetics of radical-initiated oxidation of DOS particles by OH and Cl radicals. The technique proves to be quantitative in both the measurement of the initial rate of reaction and distinguishing exponential and quadratic functional fits to the data (see section 3.1).

5.3.1 Mixed phase relative rates of methyl oleate ozonolysis

In order to verify the mixed phase relative rates approach, we first reacted particles composed of methyl oleate (MO) with O_3 and measured the kinetics of the reaction using 2-methyl-2-butene (MB) as the gas phase reference compound. Gas phase

ozonolysis reactions are known to produce OH which could complicate the kinetics, so gas phase hexanes were added to the flow tube to scavenge the OH radicals. Since hexanes lack a functional group, they were not detectable with proton transfer ionization and did not affect the ion chemistry. Particles and gases were mixed just prior to injection into the front of the flow tube to ensure efficient mixing. Particles in these experiments did not stay confined to the center of the flow tube, otherwise the particles would see a shorter reaction time than the gas phase reference which would diffuse much more rapidly toward the walls and sample the slower laminar flow velocities in the flow tube.

The second order rate constant for MB has been measured previously (k_{MB} = (4.1 ± 0.5)$\times 10^{-16}$ cm^3/molecule/second) [17], and we used it here as a clock for the ozone exposure. The ozone exposure can be calculated from the normalized MB loss according to equations (5.6) and (5.7).

$$\frac{d[MB]}{dt} = -k_{MB}[O_3][MB] \tag{5.6}$$

$$O_3\ Exposure = \int_0^t [O_3](t)dt = -\frac{1}{k_{MB}} \ln\left(\frac{[MB]}{[MB]_0}\right) \tag{5.7}$$

All the reactants were mixed and introduced at the front of the flow tube, and ion signals for both MO and MB were measured simultaneously as the O_3 concentration was gradually increased to react both components away. A representative reaction decay is shown in Figure 5.2. The bottom x-axis shows the natural log of the normalized MB signal during the reaction, and the top x-axis shows the O_3 exposure calculated from equation (5.7). The dashed and solid lines are fits to the data using exponential and quadratic functions, respectively. While the exponential function fits the data reasonably

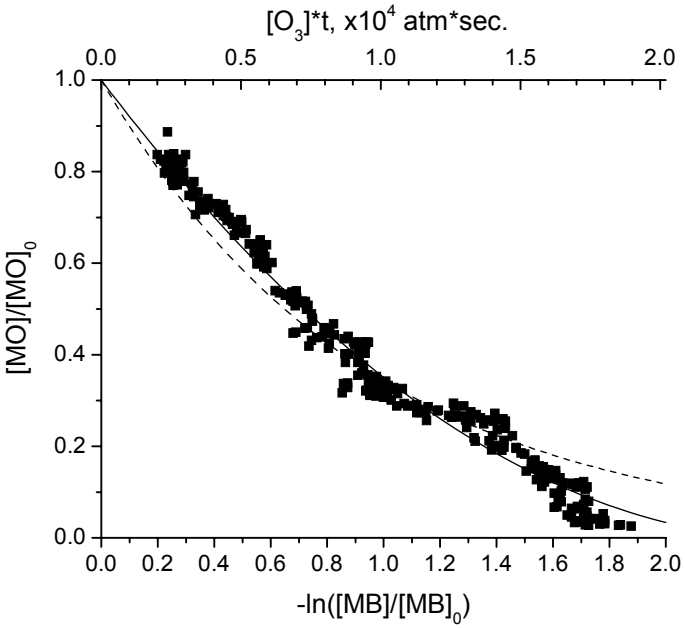

Figure 5.2. Reaction of 950 nm MO particles with O_3 with MB as the gas phase reference compound. The top x-axis is the O_3 exposure calculated from the MB reaction with $k_{MB} = 4.10 \times 10^{-16}$ cm^3/molecule/sec. The solid and dashed lines represent fits to the data using quadratic and exponential functions, respectively.

well ($R^2 = 0.94$), it overestimates the reaction at short exposure and underestimates the reaction at long exposure. The quadratic function does a much better job in describing the data ($R^2 = 0.98$) and indicates that the reaction occurs in the bulk and is limited by O_3 diffusion into the particle. This agrees with the results obtained from the absolute rate measurements in Chapter 3. From the initial slope of the reaction, γ_{MO}, the MO uptake coefficient can be calculated from rearranging equation (3.2) to give equation (5.8).

$$\gamma_{MO} = \gamma \times \varphi = \left[\frac{d\left(\left[MO\right]/\left[MO\right]_0\right)}{d\left(\left[O_3\right](t)\right)} \right] \frac{4RT}{\bar{c}} \frac{a}{3} \left[MO\right]_0 \qquad (5.8)$$

In equation (5.8), $[O_3](t)$ is the ozone exposure, $\bar{c}$ is the mean speed of ozone ($\bar{c}$ = 362 m/sec), R is the gas constant (R = 0.082 atm K^{-1} M^{-1}), T is the temperature (T = 293

K), a is the particle radius, γ is the O_3 uptake coefficient, and φ is the "reaction yield". The kinetics of MO ozonolysis was measured with the relative rates approach in 22 different experiments with three different particle diameters (750, 850, and 950 nm), and $\gamma_{MO} = (1.12 \pm 0.36) \times 10^{-3}$. This is in excellent agreement with the absolute measurements from Chapter 3 with an uptake coefficient (γ_{MO}) of $(1.23 \pm 0.10) \times 10^{-3}$. The relative rates approach is accurate in both measuring uptake coefficients (initial rate or reaction) and resolving the functional form for the heterogeneous reaction.

5.3.2 OH reaction with bis (2-ethylhexyl) sebacate

OH is the primary oxidant in the troposphere, and its reaction with organic surfaces has been measured to be fast ($\gamma_{OH} > 0.1$) [5], but this only provides a lower bound on the rate of oxidation of organic particles. We used particles composed of bis (2-ethylhexyl) sebacate (DOS) as a simple proxy for organic aerosol and measured the heterogeneous reaction kinetics of OH initiated oxidation with hexanal as the gas phase reference compound. DOS was chosen because it is a liquid at room temperature with a low vapor pressure and it lacks a carbon-carbon double bond, so it is not reactive with O_3. Particles, O_3, water vapor, and N_2 (no O_2 added) were introduced into the beginning of the flow tube and the laser light was alternately blocked and passed at various laser powers. The reaction signals (light on) were normalized to the unreacted signals (light off) before and after each measurement. A reaction decay of DOS particles (mass weighted diameter = 142 nm) is shown in Figure 5.3 where the natural log of the normalized hexanal signal is proportional to the OH exposure. The top x-axis shows the OH exposure calculated from the hexanal reaction using the hexanal + OH reaction rate constant ($k = (2.86 \pm 0.13) \times 10^{-11}$ cm^3/molecule/second) [18].

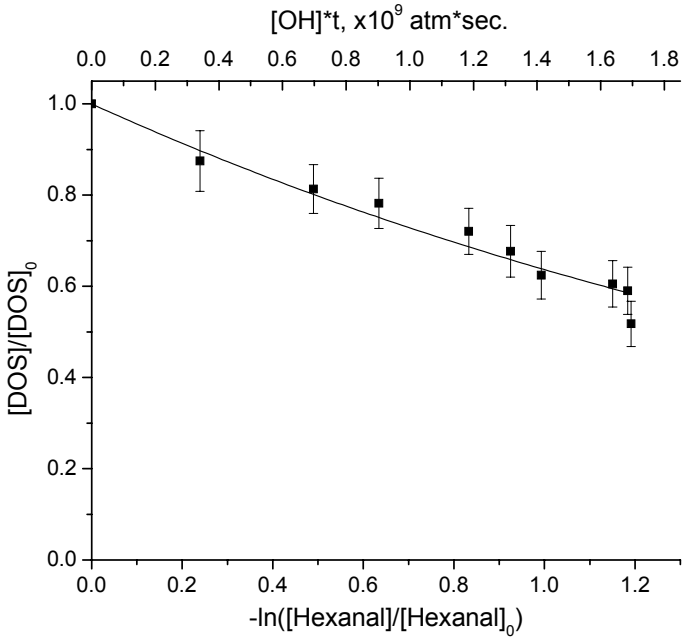

Figure 5.3. Reaction of DOS particle with OH radicals using hexanal as the gas phase reference compound. The top x-axis is the OH exposure calculated from the hexanal reaction with $k = 2.86 \times 10^{-11}$ cm^3/molecule/sec. The line represents an exponential fit to the data as a measure of the initial rate of reaction.

From the initial slope of the reaction and equation (5.8), we calculate the DOS uptake coefficient to be $\gamma_{DOS} = 2.0$ (+0.6/-0.1). The uneven error bars reflect the fact that gas phase diffusion ($\Gamma_g = 0.42$) might be partially limiting the reaction, so the reactive uptake coefficient is actually higher than what we measure. For radical reactions, the products from the reaction are just as reactive with OH as DOS, so the increased competition at large exposures makes determining an operative case impossible from the shape of the decay curve. Additionally, the particles in Figure 5.3 are only 50% reacted at the highest exposure, and there is little difference among linear, quadratic, and exponential functions over such a small range. It is clear, however, that the OH initiated oxidation of DOS particles is fast, and the fact that $\gamma_{DOS} > 1$ indicates that multiple DOS

molecules are reacted away per OH collision, suggesting that secondary chemistry is significant.

Although there was no O_2 added to the flow tube, it is a product of the photodissociation of O_3 [19], so the concentration of O_2 is not negligible. Gas phase alkyl radicals react with O_2 or O_3, and DOS is expected to follow similar reaction pathways. Both of these reactions can potentially propagate a radical chain mechanism that could yield a higher than unity uptake coefficient.

In addition to secondary chemistry increasing the observed rate of loss of DOS, other reactive gas phase species could be reacting with the particles. Side reactions in the generation of OH produce HO_2, which could react with the DOS particles. However, kinetic modeling suggests that OH and HO_2 concentrations are approximately the same, and HO_2 is unreactive to gas phase organics. For instance, the rate constant for HO_2 + propane ($k = 1.6\times10^{-25}$ cm^3/molecule/sec.) [20] is 13 orders of magnitude slower than the reaction between OH and propane ($k = 1.12\times10^{-12}$ cm^3/molecule/sec.) [21], so if HO_2 reactivity with organic particles is similar, it will not contribute significantly to the observed loss of DOS. We conclude that the increased rate of loss of DOS is due to a radical chain mechanism involving O_2 or O_3 reaction with the DOS radicals. Since $0.1 < \gamma_{OH} < 1$, the radical chain length is then between 2 and 20.

5.3.3 Cl reaction with bis (2-ethylhexyl) sebacate

Kinetics of the heterogeneous reaction of chlorine radicals with particles composed of Bis(2-ethylhexyl)-sebacate (DOS) were also measured. Acetone was chosen as the gas phase reference compound and its reaction rate with chlorine was provided by Wine and coworkers ($k = 2.09 \times10^{-12}$ cm^3/molecule/sec.) [22]. The reaction was varied by

adjusting the laser intensity while monitoring mass spectrometer signals at m/z = 427 ($DOS+H^+$) and 59 ($acetone+H^+$). A representative reaction decay of DOS is plotted in Figure 5.4 where the exposure (top axis) is calculated from the acetone reaction (bottom axis). The slope of the reaction decay was determined by fitting the initial part of the reaction on a log-log plot with a linear function allowing the intercept to float (see inset). There is no obvious reason for the reaction to follow an exponential decay since there will be significant competition for the chlorine radicals among DOS and the products as the reaction proceeds. However, an exponential function does a reasonable job describing the data, so it was used as an empirical measure of the slope.

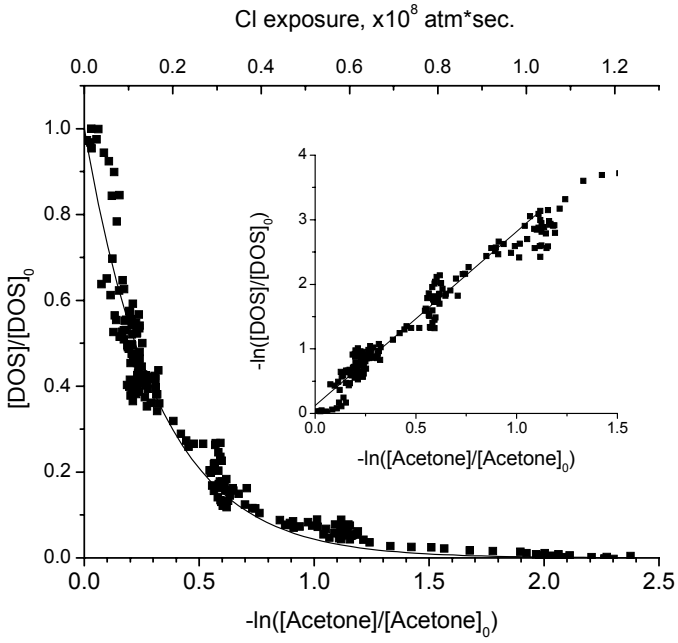

Figure 5.4. Reaction of DOS particles with Cl radicals using acetone as the gas phase reference compound. The Cl exposure (top axis) was calculated from the acetone reaction ($k = 2.09 \times 10^{-12}$ cm^3/molecule/sec.). Uptake coefficients were calculated from the slope of the log-log plot shown in the inset.

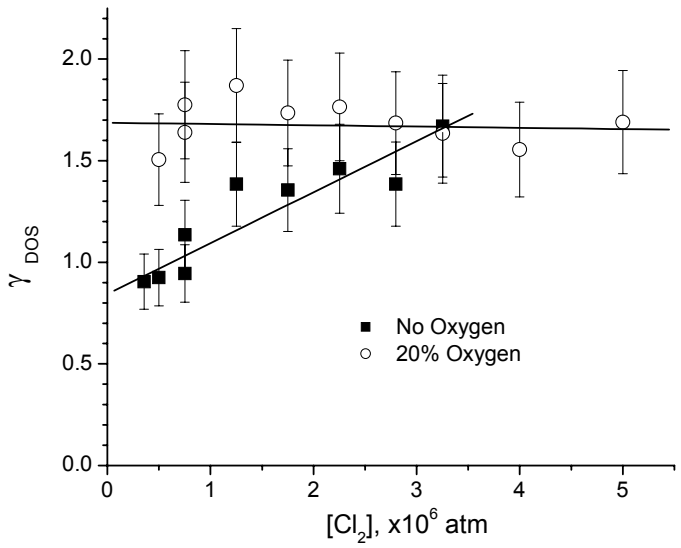

Figure 5.5. Uptake coefficients measured for the reaction between Cl and DOS particles as a function of Cl_2 concentration. Measurements made with 20% O_2 show no dependence on $[Cl_2]$ whereas in the absence of O_2 γ_{DOS} decreases with decreasing $[Cl_2]$. The lines represent linear fits to the data, and the ratio of their intercepts gives the O_2 chain length.

The Cl uptake coefficient can be related to the slope of the DOS reaction according to equation (5.8) by replacing MO and O_3 with DOS and Cl, respectively. Cl-initiated reactions were monitored in the presence and absence of 20% O_2 and at varying concentrations of Cl_2, and the results are plotted in Figure 5.5. DOS particles reacted in the absence of O_2 show a clear trend that is proportional to $[Cl_2]$, and a simple radical chain mechanism can be written for the chlorine only reaction where the chain is propagated via reaction (5.10) and terminated in reaction (5.11).

$$RH+Cl \xrightarrow{k_1} R+HCl \qquad (5.9)$$

$$R+Cl_2 \xrightarrow{k_2} RCl+Cl \qquad (5.10)$$

$$R+R \xrightarrow{k_3} Products \qquad (5.11)$$

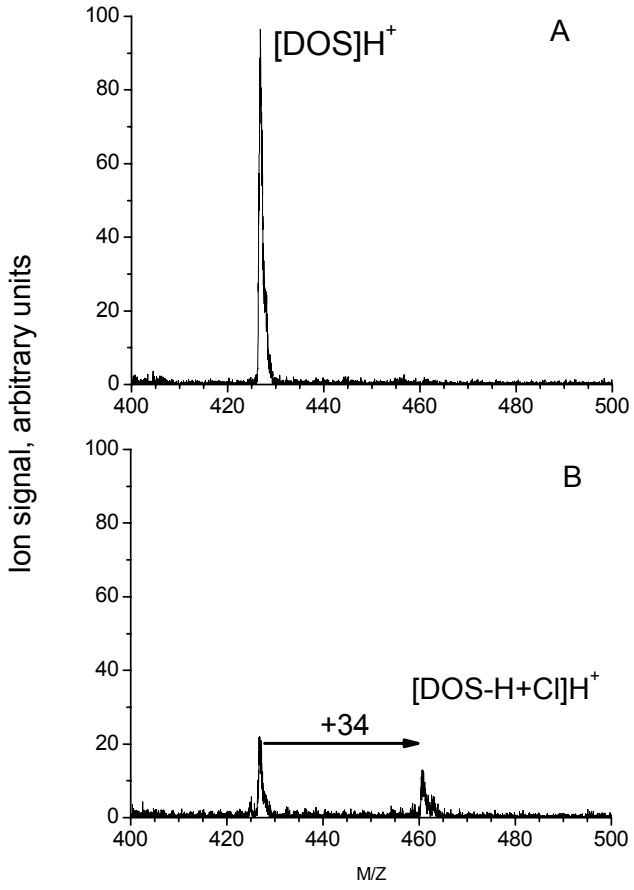

Figure 5.6. Mass spectra of (A) unreacted and (B) reacted DOS particles with Cl in the absence of O_2. A product appears at 34 mass units higher than DOS corresponding to the chloride product.

Figure 5.6 shows mass spectra of unreacted (A) and reacted (B) DOS particles with product peaks appearing at m/z = 461 and 463, corresponding to the chloride product which provides evidence for reaction (5.10). As the chlorine concentration is decreased, the propagation step will become less important, and in the limit that $[Cl_2]$ approaches 0, γ_{DOS} will approach γ_{Cl}. From a linear extrapolation of the data in Figure 5.5 the chlorine uptake coefficient (γ_{Cl}) is 0.84 which is in agreement with other Cl uptake measurements (> 0.1) [6]. The short resonance time in the flow tube (2 seconds)

prevents us from measuring the reaction at lower [Cl_2] which would help determine if a linear extrapolation is valid. It is clear that γ_{DOS} will continue to decrease as [Cl_2] is lowered, but a linear extrapolation may overestimate γ_{Cl}.

The presence of 20% O_2 removes the dependence of γ_{DOS} on [Cl_2]. This is expected since O_2 is going to dominate the secondary chemistry, and alkyl radicals will quickly react with O_2 to form peroxy radicals instead of reacting with Cl_2 to form organic chlorides:

$$R + O_2 \xrightarrow{k_4} RO_2 \tag{5.12}$$

Interestingly, γ_{DOS} is 1.7, greater than the upper limit of γ_{Cl} = 1, which indicates that secondary chemistry is consuming additional DOS molecules. From the above estimation of γ_{Cl} = 0.84, the "reaction yield" (φ) is 2, which is really a lower limit on φ since a linear extrapolation may overestimate γ_{Cl}. Thus for every Cl reaction, at least 2 DOS molecules are reacted away.

5.4 Discussion of radical-initiated reactions

Figure 5.7 shows the radical-initiated reaction mechanism for propagating a radical chain in the presence of O_2. Peroxy radicals can abstract a hydrogen from another organic molecule, and while this reaction is slow ($k = 10^{-3} - 1\ M^{-1}\ sec.^{-1}$), significant radical chains are observed for organics with tertiary or substituted carbons. DOS has two tertiary carbons, but the short reaction time and the high peroxy radical concentrations employed in these experiments ($[ROO\bullet] \approx 10^{-4}$ M) make the peroxy radical self-reaction favored over the hydroperoxide formation. Using approximate rate constants for the self-reaction ($k_{sr} \approx 10^7\ M^{-1}\ sec.^{-1}$) and hydrogen abstraction ($k_{ha} \approx 1\ M^{-1}\ sec.^{-1}$) [12] to calculate lifetimes for peroxy radicals yields 1 msec. and 1 sec., respectively. While

these lifetimes are crude estimates, they do provide reasonable doubt that the peroxy radical is propagating a radical chain. However, the peroxy radical self-reaction does not necessarily lead to termination products. It can also generate alkoxy radicals which are more reactive than peroxy radicals and can more easily abstract a hydrogen atom from another organic molecule to propagate a radical chain ($k_{alkoxy} \approx 10^6$ M^{-1} $sec.^{-1}$) [12]. Alkoxy radicals are also involved in chain terminating reactions, but reactions that do not terminate the chain may also be active. For instance, beta-scission, reaction with O_2, and isomerization do not consume another DOS molecule, but they do produce other radicals that may react with DOS. In any case, based on these broad assumptions, alkoxy radicals are propagating the radical chain in our flow tube reactions.

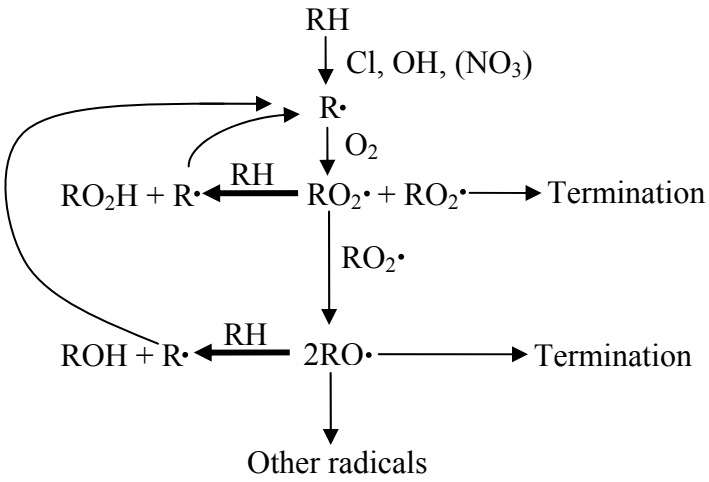

Figure 5.7. Radical-initiated reaction mechanism that explains the radical chain mechanism in the presence of O_2. The bold arrows show the propagation steps.

Using the value of γ_{DOS} measured above, the lifetime of a 200 nm DOS particle in the atmosphere will be approximately half a day. This is fast enough to chemically transform the particle before its removal from the atmosphere through wet deposition (4-5 days) and could have implications on the processes organic particles are involved in.

At ambient levels, however, OH and Cl radical concentrations (≈ 10^6 and 10^4 radicals/cm^3, respectively) [4] are much lower than what was used in these flow tube experiments (≈ 10^{11} radicals/cm^3). Since the total radical concentration is orders of magnitude lower, the importance of the peroxy radical self-reaction will be reduced relative to the propagation reaction (hydroperoxide formation) in the atmosphere. Of course, this will also reduce the rate of conversion from peroxy radicals to the more reactive alkoxy radicals, but the peroxy radical can still propagate a radical chain. In fact, hydrogen atom abstraction by peroxy radicals is the operative reaction in the auto-oxidation of liquid organics [11]. This suggests that ambient particles could be oxidized more quickly than predicted from these experiments. In addition, peroxy radicals quickly react with NO ($k \approx 9 \times 10^{-12}$ cm^3/molecule/sec.) to generate an organic nitrate or an alkoxy radical and NO_2 [21], and even in non-urban continental areas NO concentrations are large enough to competitively react with peroxy radicals (2-12 ppb) [23]. This provides another mechanism for generating the more reactive alkoxy radicals.

5.5 Summary

In summary, we have shown that a mixed phase relative rates approach to studying heterogeneous kinetics is valid by measuring the kinetics of the reaction between MO particles and O_3. The results obtained quantitatively agree with absolute kinetic measurements. We have used this technique to measure the rate of Cl and OH initiated oxidation of liquid organic particles. Both radical-initiated reactions show evidence for the presence of a radical chain, and in the case of Cl initiated oxidation, we estimated that the chain length is at least 2 in the presence of O_2. The radical chain in the OH reaction is propagated either by O_2 or O_3 and is also greater than 2 and could be as

large as 20. Radical-initiated oxidation of organic aerosol is a sufficiently fast process to be important in chemically transforming organic particles in the atmosphere, and it may be faster than predicted from these results.

References

1. Hearn, J.D., A.J. Lovett, and G.D. Smith, *Ozonolysis of oleic acid particles: evidence for a surface reaction and secondary reactions involving Criegee intermediates.* Physical Chemistry Chemical Physics, 2005. **7**(3): p. 501-511.

2. Hearn, J.D. and G.D. Smith, *Kinetics and product studies for ozonolysis reactions of organic particles using aerosol CIMS.* Journal of Physical Chemistry A, 2004. **108**(45): p. 10019-10029.

3. Rogge, W.F., et al., *Sources of Fine Organic Aerosol .2. Noncatalyst and Catalyst-Equipped Automobiles and Heavy-Duty Diesel Trucks.* Environmental Science & Technology, 1993. **27**(4): p. 636-651.

4. Finlayson-Pitts, B.J. and J.N.J. Pitts, *Chemistry of the Upper and Lower Atmosphere*. 2000, San Diego, CA: Academic Press. 969.

5. Cooper, P.L. and J.P.D. Abbatt, *Heterogeneous interactions of OH and HO2 radicals with surfaces characteristic of atmospheric particulate matter.* Journal of Physical Chemistry, 1996. **100**(6): p. 2249-2254.

6. Moise, T. and Y. Rudich, *Uptake of Cl and Br by organic surfaces - a perspective on organic aerosols processing by tropospheric oxidants.* Geophysical Research Letters, 2001. **28**(21): p. 4083-4086.

7. Molina, M.J., et al., *Atmospheric evolution of organic aerosol.* Geophysical Research Letters, 2004. **31**(22): p. L22104.

8. Eliason, T.L., J.B. Gilman, and V. Vaida, *Oxidation of organic films relevant to atmospheric aerosols.* Atmospheric Environment, 2004. **38**(9): p. 1367-1378.

9. Esteve, W., H. Budzinski, and E. Villenave, *Relative rate constants for the heterogeneous reactions of OH, NO2 and NO radicals with polycyclic aromatic hydrocarbons adsorbed on carbonaceous particles. Part 1: PAHs adsorbed on 1-2 mu m calibrated graphite particles.* Atmospheric Environment, 2004. **38**(35): p. 6063-6072.

10. Bertram, A.K., et al., *The reaction probability of OH on organic surfaces of tropospheric interest.* Journal of Physical Chemistry A, 2001. **105**(41): p. 9415-9421.

11. Walling, C., *Autoxidation*, in *Active Oxygen in Chemistry*, C.S. Foote, et al., Editors. 1995, Chapman & Hall: New York. p. 24-65.

12. Howard, J.A. and J.C. Scaiano, *Radical Reaction Rates in Liquids*. Numerical Data and Functional Relationships in Science and Technology, ed. H. Fischer. Vol. 13d. 1984, Berlin: Springer-Verlag Berlin-Heidelberg.

13. Hubinger, S. and J.B. Nee, *Absorption-Spectra of Cl-2, Br-2 and Brcl between 190-Nm and 600-Nm.* Journal of Photochemistry and Photobiology a-Chemistry, 1995. **86**(1-3): p. 1-7.

14. Molina, L.T. and M.J. Molina, *Absolute Absorption Cross Sections of Ozone in the 185 to 350 nm Wavelength Range.* Journal of Geophysical Research, 1986. **91**(D13): p. 14501-14508.

15. Matsumi, Y., et al., *Quantum yields for production of O(1D) in the ultraviolet photolysis of ozone: Recommendation based on evaluation of laboratory data.* Journal of Geophysical Research, 2002. **107**(D3): p. 1-12.

16. Chen, L., et al., *New technique for generating high concentrations of gaseous OH radicals in relative rate measurements.* International Journal of Chemical Kinetics, 2003. **35**(7): p. 317-325.

17. Witter, M., et al., *Gas-phase ozonolysis: Rate coefficients for a series of terpenes and rate coefficients and OH yields for 2-methyl-2-butene and 2,3-dimethyl-2-butene.* International Journal of Chemical Kinetics, 2002. **34**(6): p. 394-403.

18. D'Anna, B., et al., *Kinetic study of OH and NO3 radical reactions with 14 aliphatic aldehydes.* Physical Chemistry Chemical Physics, 2001. **3**(15): p. 3057-3063.

19. O'Keeffe, P., et al., *Kinetic energy analysis of O(3P0) and O2(b1sigma+g) fragments produced by photolysis of ozone in the Huggins bands.* Journal of Chemical Physics, 1999. **110**(22): p. 10803-10809.

20. Tsang, W., *Chemical Kinetic Data-Base for Combustion Chemistry .3. Propane.* Journal of Physical and Chemical Reference Data, 1988. **17**(2): p. 887-952.

21. Atkinson, R., *Gas-phase tropospheric chemistry of volatile organic compounds .1. Alkanes and alkenes.* Journal of Physical and Chemical Reference Data, 1997. **26**(2): p. 215-290.

22. Wine, P., *Personal Communication*. 2006.

23. Hameed, S. and J. Dignon, *Global Emissions of Nitrogen and Sulfur-Oxides in Fossil-Fuel Combustion 1970-1986.* Journal of the Air & Waste Management Association, 1992. **42**(2): p. 159-163.

CHAPTER 6

CHEMICAL AND PHYSICAL CHANGES OF RADICALLY OXIDIZED ORGANIC PARTICLES[1]

6.1 Introduction

In Chapter 5, radical initiated oxidation of DOS particles was measured and it was fast enough to cause significant oxidation of organic aerosol before removal from the atmosphere through wet or dry deposition. While there has been some other work done on radical initiated oxidation of organic aerosol [1-8], there is still a lot to be learned before we understand how radical initiated reactions chemically transform organic particles. Among the work that has been done, there are conflicting results on the products formed. In particular, Molina and coworkers saw that OH completely volatilized organic self assembled monolayers after an average of only three OH collisions per molecule [4]. Other studies have shown little or no volatilization of liquid organic particles after radical initiated oxidation, but instead higher molecular weight products dominated the reactions [5, 6]. The reason for these discrepancies has not yet been determined.

A general radical initiated reaction mechanism is shown in Figure 6.1. Cl radicals, like OH radicals, react with saturated organic molecules to abstract a hydrogen atom leaving an organic radical which, in the presence of O_2, will quickly react to form a peroxy radical. Peroxy radicals can form alcohol and ketone products or alkoxy radicals

[1] John D. Hearn, Lindsay H. Renbaum, Xi Wang, and Geoffrey D. Smith. Chemical and physical changes of radically oxidized organic particles. To be submitted to Journal of Physical Chemistry A. Reproduced in part with permission by the publisher.

and O_2 through a self reaction, and either peroxy or alkoxy radicals can abstract a hydrogen atom from another organic molecule to propagate a radical chain mechanism. Alkoxy radicals can also decompose to produce smaller molecular weight products, produce larger molecular weight peroxides through self reaction, isomerize, or react with O_2 [9, 10].

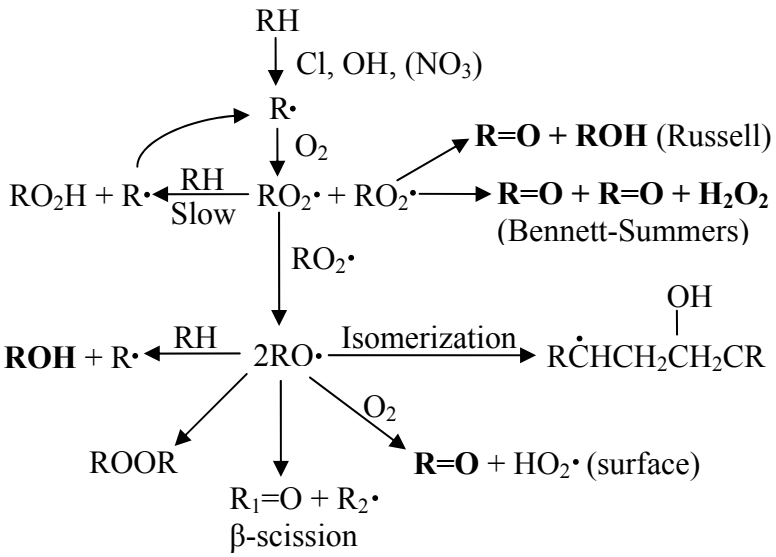

Figure 6.1. Reaction mechanism for radical initiated oxidation of a hydrocarbon. Detected products are shown in bold.

In an attempt to better understand the chemical and physical changes caused by radical initiated oxidation of liquid organic particles we reacted chlorine radicals with particles composed of bis (2-ethylhexyl) sebacate (dioctyl sebacate, DOS). DOS was chosen as a simple proxy for organic aerosol because it is a liquid at room temperature with sufficiently low vapor pressure to neglect gas phase chemistry. Chlorine radical was chosen as the gas phase radical because it can be maintained at higher concentrations than OH, and the chemistry of generating Cl is much more simple ($Cl_2 + h\nu \rightarrow 2Cl$). We measure the products on-line with an aerosol chemical ionization mass spectrometer (A-

CIMS) and off-line with an electrospray ionization Fourier transform mass spectrometer. Physical changes (size and volatility) were measured with a scanning mobility particle sizer (SMPS). The results show that the primary products are ketone and alcohol, the products stay in the condensed phase, and the products exhibit lower volatility than DOS.

6.2 Materials and Methods

Monodisperse particles were generated via heterogeneous nucleation as described in section 2.6, and Cl radical initiated reactions were carried out at atmospheric pressure as described in section 5.2. The flow exiting the flow tube was split with 0.3 standard liters per minute (slpm) being sent to the SMPS for size distribution measurements and the remaining flow being sent to the mass spectrometer and exhaust. Gases used were N_2 (99.99%, National Welders), O_2 (99.5%, National Welders), Cl_2 (UHP grade, Airgas), and NO (99.5%, National Welders). Flows were measured and maintained using mass flow controllers (MKS). Bis (2-ethylhexyl) sebacate (> 97%, Fluka) was purified from semivolatile impurities by heating and pumping to less than 10 mTorr, and Pentavac 5 (Duniway) was used without further purification.

6.3 Radical initiated chemical changes

The reaction between bis (2-ethylhexyl) sebacate (DOS) and Cl radicals was monitored on-line with A-CIMS and off-line with FTMS. These two techniques provide complementary evidence for product assignments, and the A-CIMS results are used to estimate product yields. The most abundant products are ketones and alcohols, and I make attempts to determine the operative mechanisms for their production.

6.3.1 A-CIMS data

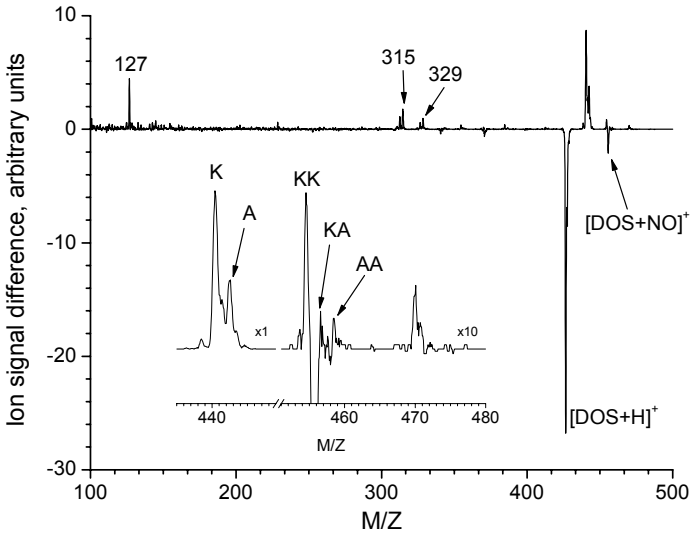

Figure 6.2. Difference spectrum for the reaction of DOS particles with Cl radicals. The negative peaks are from the DOS reaction and positive peaks are products. The inset shows a zoomed in portion of the spectrum. K = ketone product, A = alcohol product.

DOS particles (diameter ≈ 200 nm) were reacted with Cl radicals in the presence of 20% O_2. One-hundred scans were averaged with the laser blocked (no reaction), and one-hundred scans were averaged with the light on. Figure 6.2 shows the difference spectrum (reaction spectrum – no reaction spectrum), where the negative peaks are depleted from reaction, and the positive peaks are products from the reaction. The two most prominent negative peaks at m/z = 427 and 456 correspond to $[DOS+H]^+$ and $[DOS+NO]^+$, respectively. Higher molecular weight product peaks appear at m/z = 441, 443, 455, 457, 459, and 470. These correspond to first generation ketone and alcohol products, second generation ketone-ketone, ketone-alcohol, and alcohol-alcohol products, and first generation ketone product ionized with NO^+, respectively. These are the expected products from peroxy radical self reactions and some of the reactions involving alkoxy radicals. Three prominent lower molecular weight products appear at m/z = 127,

315, and 329. These are attributed to ion fragments from other products, and this will be discussed in further detail below.

The yields of these products were measured with A-CIMS as a function of DOS reaction. DOS particles were reacted to a maximum of 30% because additional reaction will result in significant amounts of multi-generational products. Figure 6.3 shows the yields for first and second generation products as a function of DOS reaction. At very small reaction, there is considerable scatter in the product yields because there is a larger error on the small DOS and product signal changes. It is clear, however, that the product yields become less scattered at higher DOS reaction. The most abundant product is the first generation ketone product with a yield of 0.39 (± 0.08) followed by the first generation alcohol product with a yield of 0.14 (± 0.03). The second generation products have yields of 0.019 (± 0.012), 0.012 (± 0.010), and 0.007 (± 0.006) for the ketone-ketone, ketone-alcohol, and alcohol-alcohol products, respectively at $[DOS]/[DOS]_0$ = 0.71. The peak at m/z = 459 (alcohol-alcohol product) could also come from the peroxy radical reaction with DOS to form an organic peroxide.

The calculations of these yields are based on the following three assumptions: (1) the ionization rate constants are the same for the products and DOS, (2) ion fragmentation is negligible, and (3) the quadrupole transmission efficiency is uniform. The first assumption is necessary because standards for the products are not commercially available for calibration with A-CIMS. It is valid since oxygenated organics are ionized at roughly the same rate as one another. Oxygenated organics with a permanent dipole are ionized via proton transfer from H_3O^+ with bimolecular rate constants of (2-4) $\times 10^{-9}$ cm^3/sec., and organics that lack a permanent dipole or oxygen

containing functional groups can have slightly slower rate constants but still fast ($k > 1.5\times10^{-9}$ cm^3/sec.) [11]. We crudely measured the proton transfer rate constant between protonated water clusters and DOS and obtained a rate constant of $k = 3.8\times10^{-9}$ cm^3/sec. (see Chapter 2). This compares well with the proton transfer rate constants for organics with permanent dipoles, so perhaps the local dipole moments in DOS increase the predicted proton transfer reaction rate constant. Therefore, we expect the products and DOS to be ionized with the same efficiency.

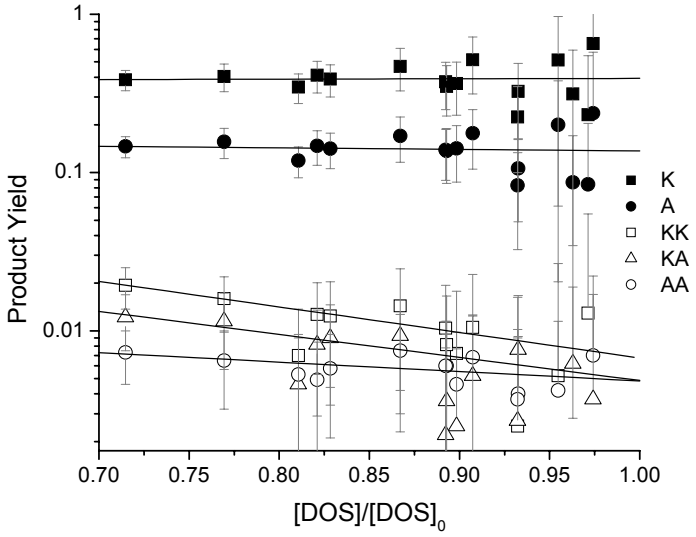

Figure 6.3. Product yields for first and second generation products as a function of DOS reaction. K = ketone, A = alcohol. The second generation products increase at the higher DOS reaction. Lines are drawn to guide the eye.

Second, product ion fragmentation can occur which would decrease the observed product yields because some of the ion signal would be in fragment peaks. Since ion fragmentation does happen in chemical ionization (see Chapter 2) we measured the signals from the product peaks of reacted DOS particles as a function of the ion tube temperature, and Figure 6.4 shows the results. Signals from DOS and first and second

generation products decrease with increasing ion tube temperature. On the other hand, the peak at m/z = 315 first increases and then decreases as the temperature is increased, and the peak at m/z = 127 increases with increasing temperature. These results suggest that the lower molecular weight peaks are ion fragments and not direct products from the radical initiated oxidation of DOS. To illustrate the effect that a higher ion tube temperature has on fragmentation, Figure 6.5 shows spectra of unreacted DOS with the ion tube heated to 145°C (A) and 360°C (B). When the ion tube temperature is lower, more than 95% of the DOS ion signal is in the $[M+H]^+$ peak (the lower molecular weight peaks are background organics and protonated water clusters). At the higher temperature, DOS looses the fragments shown in Figure 6.5 to yield a prominent peak at m/z = 185.

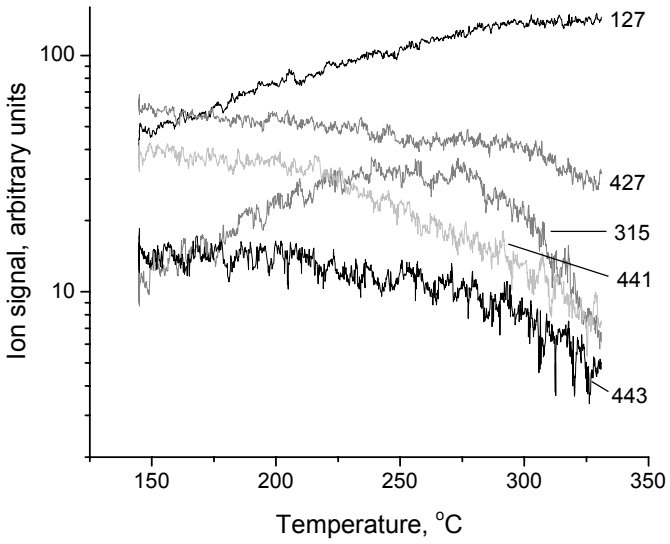

Figure 6.4. Ion signals of DOS (m/z = 427) and product peaks as a function of ion tube temperature. The larger molecular weight peaks decrease in intensity at higher temperature and the peak at m/z = 127 increases.

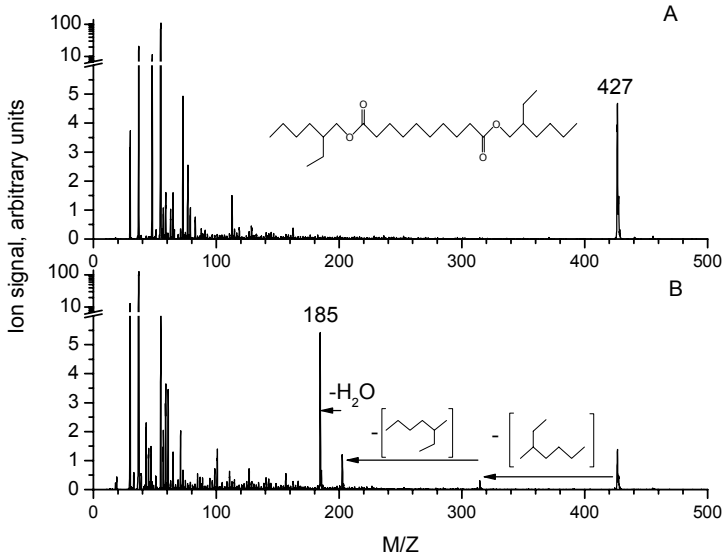

Figure 6.5. Spectra of unreacted DOS with the ion tube temperature at (A) 145°C and (B) 360°C. The higher ion tube temperature fragments DOS to m/z = 185 by loss of the indicated groups.

In addition to fragmentation decreasing the observed yield of alcohol and ketone products, some of their ion signal could be coming from the fragmentation of larger products. For instance, protonated hydroperoxides are known to fragment by loosing neutral water [12, 13], which in the case of the DOS reaction would appear at m/z = 441. However, the water loss peak from protonated cumene hydroperoxide observed by Rondeau et al. was less than 10% of the protonated signal [12]. If there is similar fragmentation of a DOS peroxide (m/z = 459) its contribution to the signal at m/z = 441 would be insignificant.

Third, quadrupole mass spectrometers are known to have mass discrimination [14, 15] but over a small range of masses, this is a small effect. The transmission efficiencies of DOS and the first and second generation products are therefore very close. However, the ion fragment at m/z = 127 is significantly different, so we measured the transmission

efficiency of hexanal (m/z = 101) and DOS (m/z = 427) as described in section 2.5 to approximate the relative transmission efficiency of m/z = 127. DOS was transmitted with approximately 50% efficiency relative to hexanal, and correcting this peak gives a yield of 0.05 (± 0.03) for m/z = 127 at the lower ion tube temperature (145ºC).

If, in addition to ion fragmentation, there is contribution to the signal at m/z = 127 from products, they may be in the gas phase since A-CIMS detects both condensed phase and gas phase organics. A filter (0.3 μm pore size) was placed at the exit of the flow tube to remove the particles to test for gas phase products. The mass spectrum was monitored with the light on and off, and no products were observed to penetrate the filter. This confirms that the low molecular weight products (m/z = 127 and 315) are not volatile. This is unexpected for the product at m/z = 127 since such a small organic would have a high vapor pressure (e.g. nonanal vapor pressure = 650 mTorr at 22ºC) [16], but as mentioned above, the signal at m/z = 127 is at least due in part to ion fragmentation. This filter experiment, therefore, suggests that none of the ion signal at m/z = 127 is due to a primary product. This does not mean that no volatile products are made since there may be products such as water, CO_2, or H_2O_2 that are not detectable with proton transfer ionization.

6.3.2 FT-ICR MS data

In addition to analyzing reacted particles on-line with A-CIMS, glass slides were coated with DOS particles and reacted with Cl radicals. The slides were coated by placing them in a small chamber and nebulizing DOS particles into the chamber. Particles settled onto the glass slides providing a thin, non-uniform coating. The slides were placed in a 1 inch i.d. flow tube, and the laser light was aligned to pass parallel to

the coated face of the slides and a mixture of N_2 (80%), O_2 (20%), and Cl_2 ($\approx 10^{16}$ molecules/cm^3) was flowed through the tube. A glass slide was removed before reaction, and one was removed after 40 minutes of reaction. The slide was then washed with 1.5 mL of methanol and analyzed with electrospray ionization Fourier transform mass spectrometry (ESI-FTMS, Bruker). While this method does not provide real-time analysis of the reaction, it does give accurate mass measurements [17].

Figure 6.6 shows a spectrum of reacted DOS. First-, second-, and third-generation products are labeled in Figure 6.6A, and a zoomed in spectrum of first-generation oxidation products is shown in Figure 6.6B to illustrate the resolution obtained with FTMS. Unfortunately, quantification with ESI-FTMS in multi-component mixtures is cumbersome [18], but it does provide impressive mass accuracy. Table 6.1 shows the accurate mass measurements for the detected product peaks, the calculated mass for the different product ions, and their relative error. All the product assignments agree with the calculated mass within a 10 ppm error, corroborating the assignments in the A-CIMS spectrum in Figure 6.2. In addition to the expected ketone and alcohol products, the FTMS spectrum shows chloride products. This is probably caused by the high concentration of Cl_2 used in this experiment. The aerosol experiments used much lower concentrations ($\approx 10^{14}$ molecules/cm^3) which would decrease the importance of this channel.

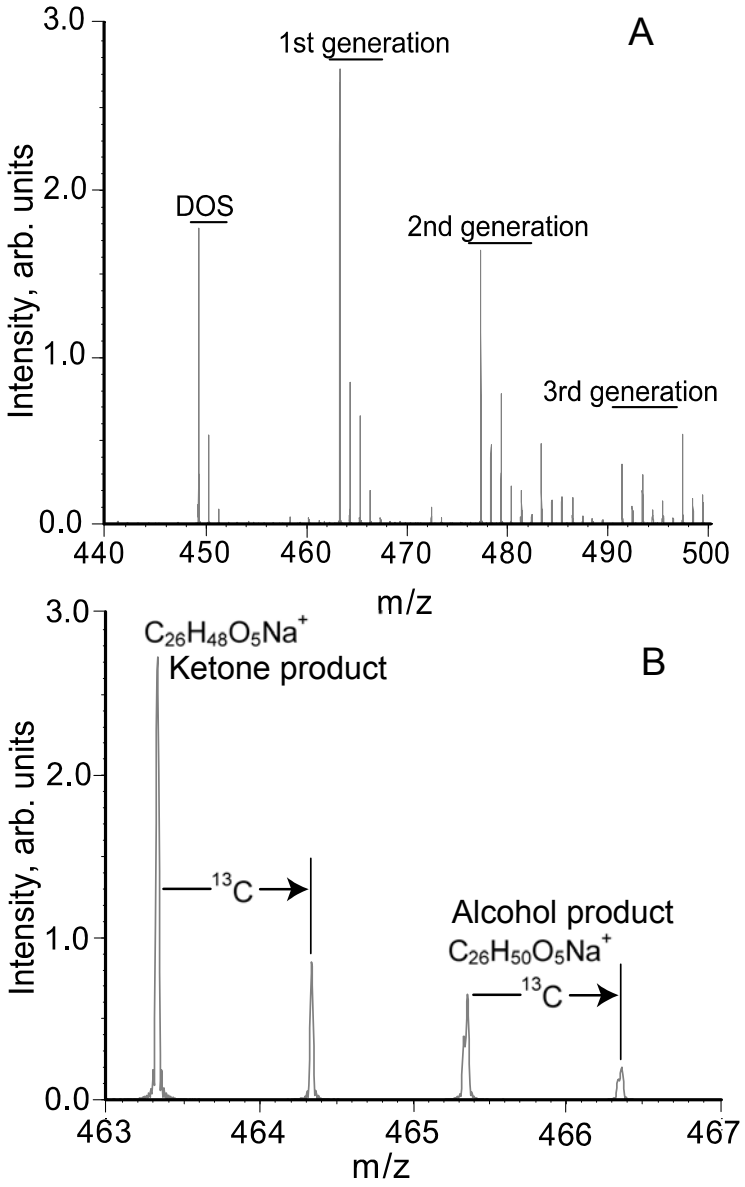

Figure 6.6. ESI-FTMS spectrum of a reacted DOS film showing (A) 1st, 2nd, and 3rd generation oxidation products and (B) a zoomed in spectrum of the first generation products.

Table 6.1. FTMS results showing the calculated and measured masses for the molecular formulas shown. All assignments agree to the calculated mass within a 7 ppm error.

		Mass, amu		
Identity	Molecular formula	Calculated	Measured	Error, ppm
DOS	$C_{26}H_{50}O_4Na^+$	449.3601	449.3610	2.00
K	$C_{26}H_{48}O_5Na^+$	463.3394	463.3402	1.73
A	$C_{26}H_{50}O_5Na^+$	465.3550	465.3565	3.22
K-K	$C_{26}H_{46}O_6Na^+$	477.3187	477.3192	1.05
K-A	$C_{26}H_{48}O_6Na^+$	479.3343	479.3355	2.50
A-A	$C_{26}H_{50}O_6Na^+$	481.3500	481.3516	3.32
Cl	$C_{26}H_{49}ClO_4Na^+$	483.3212	483.3216	0.83
K-K-K	$C_{26}H_{44}O_7Na^+$	491.2979	491.2984	1.02
K-K-A	$C_{26}H_{46}O_7Na^+$	493.3136	493.3156	4.05
K-A-A	$C_{26}H_{48}O_7Na^+$	495.3292	495.3310	3.63
Cl-K	$C_{26}H_{47}ClO_5Na^+$	497.3004	497.3009	1.01
Cl-A	$C_{26}H_{49}ClO_5Na^+$	499.3161	499.3195	6.81

In addition to the low molecular weight product peaks in the FTMS spectrum there were peaks at high molecular weight (m/z > 850). These could be ion clusters from the ionization source or products from the reaction. Reaction of two alkoxy radicals can yield an organic peroxide [19]. Unfortunately, the mass of the peroxide (m/z = 905.6897) is identical to the mass of the ketone product – alcohol product ion dimer. In order to determine whether the peak detected at m/z = 905.6897 is the ion dimer or the peroxide product, we isolated the product ion and fragmented it with either infrared radiation multi-photon dissociation (IRMPD) or collisional activated dissociation. Both fragmentation methods gave the same results, and Figure 6.7 shows the IRMPD results. If the peak at m/z = 905.6897 is the peroxide, then the most labile bond is the O-O peroxide bond (30-40 kcal/mol) and it should fragment to give a peak at m/z = 464.3472 [20]. While there is a peak close to what is expected, it is 1.0054 mass units higher than the ketone product (m/z = 463.3383) and it only corresponds to the ^{13}C isotope peak of

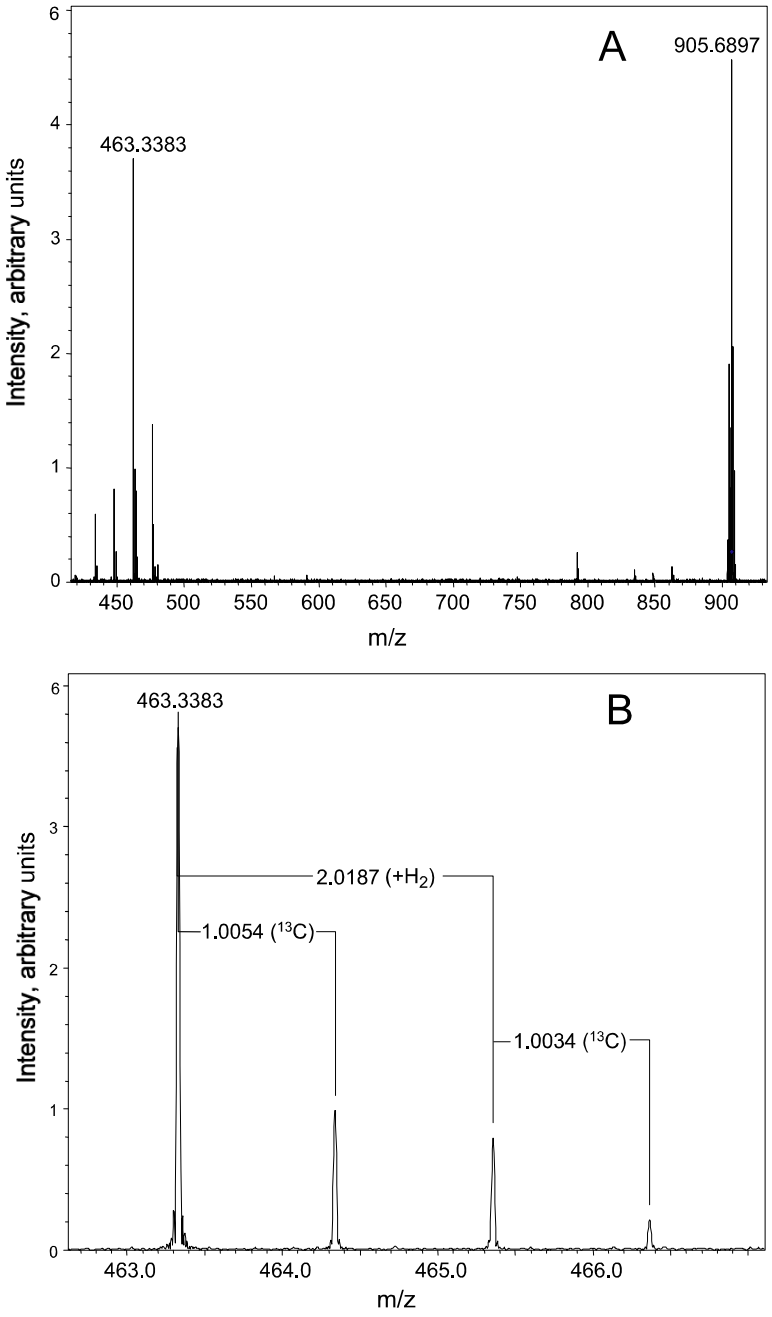

Figure 6.7. (A) IRMPD spectrum of the peak at m/z = 905.6897 from the DOS + Cl reaction showing fragment peaks from m/z = 430 to 480. (B) Zoomed in spectrum of the fragment peaks around m/z = 464. The peak at m/z = 464.3437 is the carbon 13 isotope peak of the ketone product (m/z = 463.3383) and not the expected fragment from a peroxide (m/z = 464.3472).

the first generation ketone product ($^{13}C - {}^{12}C = 1.0034$ amu). The addition of a hydrogen atom would make a peak 1.0094 mass units larger than the ketone, and this is a large enough difference with what was measured to rule out the peroxide fragment. In fact, all the product ions from the fragmentation of m/z = 905.6897 are closed shell products that were detected in Figure 6.6 leading to the conclusion that this large molecular weight peak is ion dimers not the peroxide product.

6.3.3 Oxygen dependent reaction

The results from above show that the yield of ketone product is larger than the alcohol yield, and if the termination reaction of two secondary peroxy radicals only produces pairs of alcohol and ketone products (Russell mechanism), their ratio would be one. Fortunately, there are other ways of making both alcohols and ketones, and the reaction between alkoxy radicals and O_2 to form a ketone and HO_2 is of particular interest. While this reaction has not been observed in the condensed phase, it does occur in gas phase reactions [21] and may be operative in the heterogeneous oxidation of DOS particles. Furthermore, it is the only reaction that should show a dependence on $[O_2]$. To investigate this, we measured the ketone and alcohol yields as a function of $[O_2]$; if this reaction is important there should be a strong dependence of the ketone yield on $[O_2]$. Figure 6.8A shows the results from this experiment, and the ketone yield drops by over a factor of 2 as the O_2 concentration is dropped. This large drop in ketone yield strongly suggests that alkoxy radicals are reacting with O_2 to generate ketones. Upon closer inspection of Figure 6.8A, it is clear that the alcohol yield also drops slightly as the O_2 concentration is dropped, but this drop is not nearly as large as the drop in ketone yield.

Figure 6.8B shows the ketone/alcohol product yield ratio as a function of [O_2] to demonstrate the significance of the drop in ketone yield.

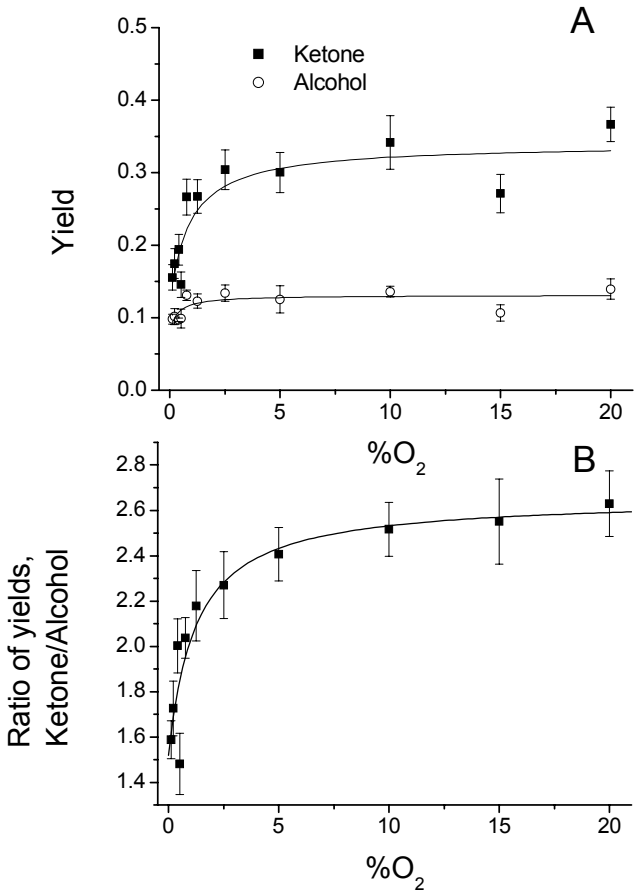

Figure 6.8. (A) O_2 concentration dependence on ketone and alcohol yields and (B) the ratio of the ketone/alcohol yields as a function of O_2 concentration. The lines in (A) and (B) are fits to the data using the Langmuir isotherm.

The slight drop in alcohol product yield is probably due to the reaction between alkyl radicals and peroxy or alkoxy radicals. As the O_2 concentration is lowered, the rate of conversion from alkyl to peroxy radical is slowed, increasing the steady state concentration of alkyl radicals. This, however, will affect both ketone and alcohol yields.

The dependence of the ketone/alcohol ratio on [O_2] is attributed to the reaction between alkyl radicals and O_2. The ratio of the ketone and alcohol yields provides a convenient way of canceling the pre-peroxy radical chemistry out since the alcohol product has no known [O_2]-dependent channel. In addition, any variations of the particle concentration will be canceled with this approach. Interestingly, Figure 6.8B does not show a linear dependence of the yield ratio on [O_2] which would be expected for competitive reactions according to the rate law. Instead, the yield resembles the Langmuir adsorption isotherm for a surface reaction where either the surface sites or the gas phase reactant are limiting the reaction [22]. At large [O_2] the surface sites are saturated so the yield is independent of [O_2], and at small [O_2] the surface sites are in excess so the reaction depends on [O_2] linearly. A traditional Langmuir isotherm has an intercept at 0, but since there are other reactions that can produce the ketone product, the intercept might not be 0. In addition, the data in Figure 6.8 are the yields and yield ratios of the alcohol and ketone products, not their rates of production. Since product yields and rates of production are proportional to each other, it is valid to plot their yields. Therefore, the data in Figure 6.8 were fit to equation (6.1) which is based on the Langmuir isotherm. R is the ketone/alcohol yield ratio, the intercept (ϕ) is the ratio of the ketone to alcohol yields from reactions not dependent on [O_2], ϕ_{O_2} is the ratio of the [O_2]-dependent ketone yield with the alcohol yield, and A is an empirical parameter.

$$R = \phi + \frac{\phi_{O_2} A[O_2]}{1 + A[O_2]} \tag{6.1}$$

The line in Figure 6.8B shows the best fit, and the alkoxy radical + O_2 reaction (ϕ_{O_2}) accounts for 42% of the ketone production. Unfortunately, the lower ketone yield

at low [O_2] is not accompanied by an increase in the yield of another observed product. While this is unsatisfying, the total detected product yield is approximately 0.6 at 20% O_2, so A-CIMS is blind to 40% of the reaction. The yields of these undetected products may be increasing at the lower [O_2] and may be products from other alkoxy radical reactions.

6.3.4 Hydrogen peroxide production

Not only can additional ketone be produced through the alkoxy radical reaction with O_2, but the peroxy radical self-reaction can proceed via the Bennett and Summers mechanism to form two ketone products and H_2O_2 [23]. A simple test to determine if this reaction is occurring is to measure the H_2O_2 yield. Unfortunately, H_2O_2 is not detectable with proton transfer [24], it is not stable enough to survive the elevated temperatures of the vaporizer and ion tube, and it is reactive to Cl ($k = 4\times10^{-13}$ cm^3/sec.) [25]. To circumvent these problems, we changed the ion chemistry, inlet and chemical ionization tubes, and the flow tube pressure. NO^+ was used as the primary ion since NO^+ ionizes H_2O_2 through association to form the $[H_2O_2+NO]^+$ ion at m/z = 64 [24]. Additionally, the vaporizer was replaced with ¼ inch tubing and the ion tube was not heated (i.e. T = 293 K). Since ¼-inch tubing is not very restrictive, the flow tube was evacuated to ≈ 50 Torr. This reduced the resonance time in the flow tube for gas phase species and minimized the reaction between Cl and H_2O_2. The inner walls of a glass flow tube were then coated with halocarbon wax to minimize the background reactions with the walls [2, 3].

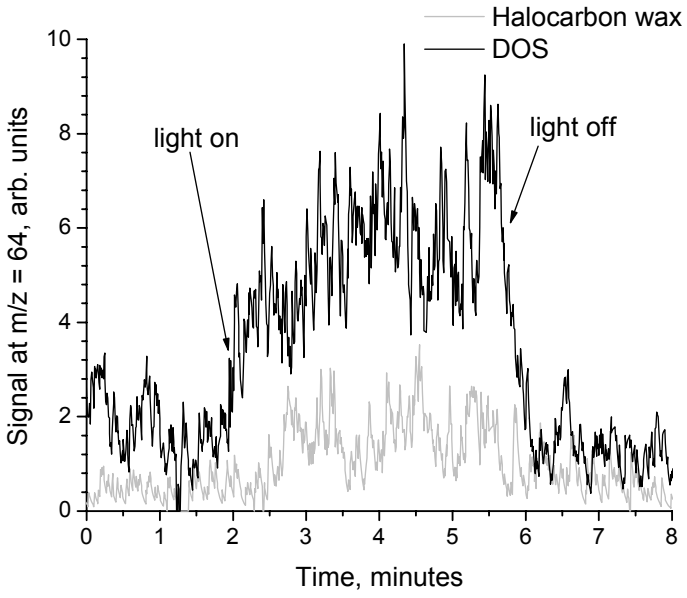

Figure 6.9. Gas phase H_2O_2 detected with NO^+ ionization as $[H_2O_2+NO]^+$ from the reaction of Cl radicals with the walls of a flow tube coated with halocarbon wax or DOS. The presence of H_2O_2 provides evidence that the Bennett and Summers mechanism is operative.

With a flow of N_2 carrying 20% O_2, and trace amounts of Cl_2, the laser light was alternately blocked and passed and the signal at m/z = 64 was monitored. $[Cl_2]$ and the laser intensity were similar to those used in particle experiments, so the Cl radical concentration was also comparable. Figure 6.9 shows the results from this experiment where the signal rise of m/z = 64 was first measured with a clean flow tube (halocarbon wax), then the inner walls were coated with DOS particles and the signal rise was measured again. With a DOS coating, the signal at m/z = 64 was well above the background reaction, and this provides positive evidence for the Bennett and Summers mechanism. However, since the absolute DOS reaction is unknown, the yield of H_2O_2 cannot be calculated, so this only provides qualitative evidence for this reaction channel.

6.4 Radical initiated physical changes

The mass spectral analysis shows that approximately 60% of the DOS reaction is accounted for in the few products detected. With the exception of H_2O_2, all of the detected products partitioned to the condensed phase, but it is unclear whether the undetected products remain in the particles or not. In order to examine this, the reaction was monitored by simultaneously measuring both particle size distributions (SMPS) and extent of DOS reaction (A-CIMS). The size data was used to determine changes in particle volume as a function of DOS reaction by normalizing the reacted particle volume to the unreacted particle volume. A value of 1 indicates that all of the products remain in the condensed phase and a value of 0 indicates that the particles are completely volatilized. Figure 6.10 shows the normalized particle volume as a function of DOS reaction, and the particle volume remains constant until more than 50% of the DOS is reacted away. After this point, the particle volume decreases only slightly (< 20%) suggesting that gas phase products are produced with small mass yields. The observed volume decrease is probably due to the continued reaction of products at the high exposures needed to react most of the DOS away.

Although most of the products remain in the particles, they are more highly functionalized and may have a different volatility than DOS. Recent studies have measured the volatility of particle constituents in single- and multi-component laboratory generated aerosol [26] ambient aerosol [27-29] and secondary organic aerosol [30]. This is a fairly straightforward approach to measuring physical properties of particle constituents where a particle flow is sent through a heated section of tube and the size change is measured. The remaining particle volume consists of less volatile material that

has been attributed to nonvolatile organics, metal oxides, or elemental carbon. One study measured the volatility of secondary organic aerosol produced from the photo-oxidation of 1,3,5-trimethylbenzene, and the increase in the nonvolatile fraction increased with longer reaction times and was attributed to oligomer formation [30].

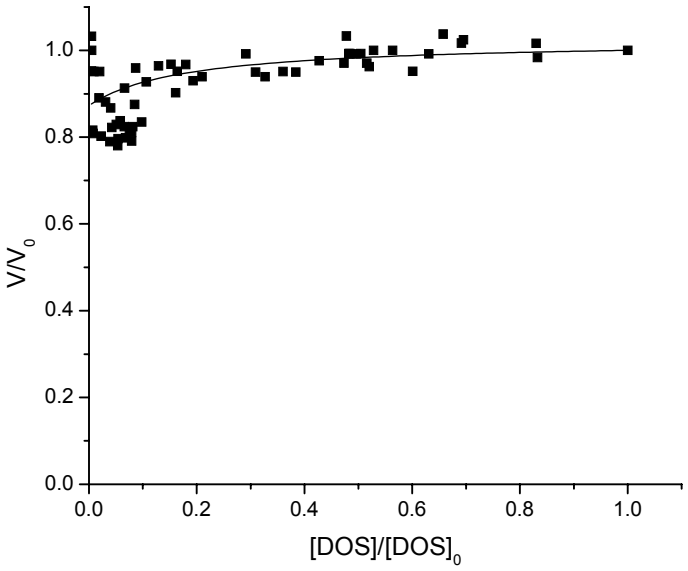

Figure 6.10. Volume changes of reacted DOS particles measured with a SMPS showing that volatile products are made with small yields. The line is drawn to guide the eye.

In order to determine the volatility of reacted and unreacted DOS particles, the flow to the SMPS was diluted with N_2 (0-0.27 slpm) and sent through a ¼ inch outer diameter stainless steel tube heated for 2 inches at a total flow rate of 0.3 slpm (0.2 second residence time). The flow was then cooled back to room temperature, and the size distribution was measured with a SMPS. The total particulate volume was normalized to the volume at 20ºC, and this was done at several different temperatures and at three different exposures. Figure 6.11 shows a plot of the fractional volume remaining

after heating as a function of the temperature of the heated section of tube. The volume of pure DOS particles rapidly decreases with tube temperatures between 75ºC to 100ºC, and essentially all the particle volume is gone at temperatures greater than 100ºC. When DOS particles are only 20% reacted (open squares), the volatility curve deviates from the pure DOS curve only at the tail. This is expected since the products are more heavily oxidized than DOS which reduces their vapor pressure. At 80% reaction (open circles), the volatility curve is shifted to even higher temperatures. Additionally, the reacted particles show a gradual decrease in particle volume with temperature, in contrast to pure particles (DOS and Pentavac 5) which show very rapid drops in particle volume with respect to the temperature. This is expected since the reacted particles are composed of many different products with different vapor pressures which broadens the volatility

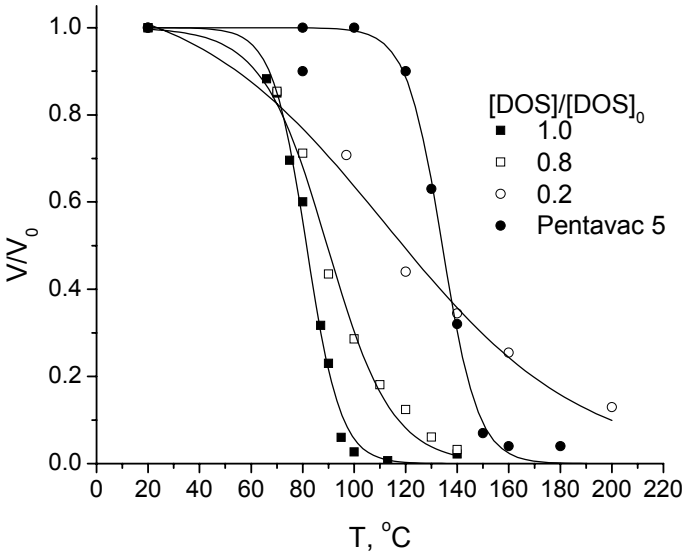

Figure 6.11. Volatility of unreacted and reacted DOS particles. Particles were sent through a heated section of stainless steel tubing and the integrated particle volume was measured. The reacted particles show lower volatility than pure DOS. Pentavac 5 is shown as a low vapor pressure reference. Lines are drawn to guide the eye.

curve. As a low vapor pressure reference the volatility of diffusion pump oil particles (Pentavac 5, P = 4 x 10^{-10} Torr @ 25ºC) [31] was also measured.

We repeated the experiment at a lower particle concentration by increasing the N_2 dilution flow to ensure that re-nucleation of the volatilized portion of the particles was not important. The fractional volume remaining did not change for the lower particle concentration (data not shown) confirming that only the non-volatile components remain in the condensed phase. This decrease in volatility can be attributed to more oxygenated products.

6.5 Discussion

Figure 6.1 shows the reaction mechanism for a radical initiated oxidation of a hydrocarbon. Although DOS has two ester groups, it will react with Cl or OH in the same way. There are two general classes of reactions in radical initiated reactions, those involving peroxy radicals (ROO•) and those involving alkoxy radicals (RO•). In the gas phase, reactions between secondary peroxy radicals produce both the termination products (alcohols and ketones) and alkoxy radicals (RO•). On the other hand, condensed phase reactions between secondary peroxy radicals yield almost exclusively termination products (alcohols and ketones). Unfortunately, DOS has both secondary and tertiary carbon atoms, and the tertiary peroxy radical self reaction only generates alkoxy radicals in both condensed and gas phase reactions. This added complexity ensures that at least some of the time, alkoxy radical chemistry is occurring. In the following discussion, I will make a case for the operative mechanisms in this reaction and estimate their relative importance.

From the mass spectral data, it is clear that the dominant products from the reaction are ketones and alcohols, and the ketone yield is 2.8 times the alcohol yield. Without further analysis, this suggests that the Russell mechanism for peroxy radical self-reaction to form an alcohol and ketone pair is not the only operative mechanism. Otherwise, the alcohol and ketone yields would be equal. There are, however, two other ways of generating additional ketone product either through the Bennett and Summers mechanism for peroxy radical self reactions or through the reaction of alkoxy radicals with O_2. The former will also make H_2O_2 and the latter will show a dependence on O_2 concentration. The results shown above provide positive evidence for both of these channels. Unfortunately, since the extent of DOS reaction was unknown in the H_2O_2 detection, it only shows that the Bennett and Summers mechanism is operative. The $[O_2]$ dependence, on the other hand, can be used to determine the relative importance of the alkoxy radical + O_2 reaction.

From the fit in Figure 6.8B, we estimate that the yield of the alkoxy radical + O_2 reaction is 0.16, so the sum of the other two ketone-producing channels (Russell mechanism and Bennett and Summers mechanism) is 0.23. This yield (0.23) is still significantly higher than the alcohol yield (0.14) and suggests that the Russell mechanism is not the only other operative reaction, otherwise the ketone and alcohol yields would be equal. At least some of the ketone production is coming from the Bennett and Summers mechanism since H_2O_2 was detected in the gas phase (see Figure 6.9). In fact, it is possible that all of this ketone production is coming from this reaction while the alcohol product is generated through the efficient reaction of alkoxy radicals with hydrocarbons ($k = 10^5$-10^7 M^{-1} $sec.^{-1}$). This scheme for alcohol production is corroborated by the

presence of a radical chain mechanism (see Chapter 5) since it would also consume additional DOS molecules. Therefore, we have no direct (or indirect) evidence that the Russell mechanism is even operative. This does not mean it is not happening, but from the results presented here, we cannot say one way or the other.

One other possible explanation of the higher ketone yield is that its proton transfer rate constant is larger than for the alcohol. Indeed, acetone has a slightly higher proton transfer rate constant than isopropanol (k_{PT} = 3.9 and 2.8 $\times 10^{-9}$ cm^3/molecule/sec., respectively [32]), but the products from the oxidation of DOS have two ester groups that can also accept the proton. This will reduce the difference between the proton transfer rate constants of the alcohol and ketone products, so it is unlikely that ionization efficiencies can explain the high ketone signal.

Even with the broad assumptions made for the product yield analysis, A-CIMS is still blind to 40% of the product yield. Unfortunately, A-CIMS is only sensitive to ions with m/z < 500 amu, so it is conceivable that products are made that are outside this mass range. While peroxides (reaction between two alkoxy radicals) were not detected in the FTMS data they may still be present, and there are other mechanisms for generating large molecular weight products. However, in the absence of positive evidence for such reactions, suggesting their presence it is pure speculation.

As discussed in Chapter 5, radical initiated oxidation of organic particles is fast enough to chemically transform particles before their removal from the atmosphere through wet deposition. However, if radical initiated oxidation of organic particles makes smaller, more volatile products, then chemical reaction can compete with wet deposition as a removal process. In fact, Molina et al. concluded that radical initiated

volatilization is an important sink for organic aerosol because in the reaction between OH radicals and an organic monolayer, the organic monolayer disappeared after only an average of 3 OH collisions per molecule [4]. This conclusion is in contrast to the results presented above where even at the extreme case of reacting > 95% of the DOS, there was only about 10% of the particle volume lost. Additionally, the products that remained in the reacted DOS particles showed decreased volatility which is not consistent with β-scission to make smaller, more volatile species. Together, this suggests that volatilization through β-scission of the alkoxy radical is a minor channel for radical initiated oxidation of liquid organic particles. The mechanism for rapid volatilization of organic molecules observed by Molina et al. may be specific for a monolayer surface and may not occur in liquids.

With the exception of the work by Molina et al., the present work compares well with recent work on radical initiated oxidation of organic films and particles. Eliason et al. identified ketone products from the oxidation of a hexadecane film by OH as well as octanal from β-scission [5]. They did not observe the alcohol product which suggests that the Russell mechanism was not operative in their film. They attribute the ketone product to the alkoxy radical reaction with O_2 with no mention of the Bennett and Summers mechanism. However, there may have been contribution from both channels in their reaction. It is interesting that they did not observe any alcohol formation whereas we see a significant amount. This difference is probably due to the tertiary carbons in DOS which, if oxidized, cannot make a ketone and must make an alcohol. The reaction between NO_3 radicals and unsaturated organics has also been studied, and only higher molecular weight products have been detected in the oxidation of oleic acid particles [6].

Additionally, NO_3 causes a maximum of only 10% volatilization of unsaturated organic surfaces [7], similar to the results presented here.

6.6 Summary

In summary, we have used mass spectrometry to monitor the radical initiated heterogeneous oxidation of DOS particles. The results show that the dominant product from the reaction is a ketone and 42% of its yield comes from the reaction between alkoxy radicals and O_2 at the particle surface. Additionally, the Bennett and Summers mechanism (formation of two ketones from a peroxy radical self-reaction) is operative, but it is not clear how much it contributes to the ketone yield. The products from the reaction remained in the particles with very little volatilization even at a large extent of reaction ($[DOS]/[DOS]_0 < 0.05$), and we conclude that volatilization from radical initiated oxidation will not be an important loss process for organic aerosol in the atmosphere. Products from the reaction also had a lower volatility than DOS, consistent with the addition of oxygen containing functional groups. The undetected products could be peroxides or oligomers outside the mass range of A-CIMS.

References

1. Cooper, P.L. and J.P.D. Abbatt, *Heterogeneous interactions of OH and HO2 radicals with surfaces characteristic of atmospheric particulate matter.* Journal of Physical Chemistry, 1996. **100**(6): p. 2249-2254.

2. Bertram, A.K., et al., *The reaction probability of OH on organic surfaces of tropospheric interest.* Journal of Physical Chemistry A, 2001. **105**(41): p. 9415-9421.

3. Moise, T. and Y. Rudich, *Uptake of Cl and Br by organic surfaces - a perspective on organic aerosols processing by tropospheric oxidants.* Geophysical Research Letters, 2001. **28**(21): p. 4083-4086.

4. Molina, M.J., et al., *Atmospheric evolution of organic aerosol.* Geophysical Research Letters, 2004. **31**(22): p. L22104.

5. Eliason, T.L., J.B. Gilman, and V. Vaida, *Oxidation of organic films relevant to atmospheric aerosols.* Atmospheric Environment, 2004. **38**(9): p. 1367-1378.

6. Docherty, K.S. and P.J. Ziemann, *Reaction of oleic acid particles with NO3 radicals: Products, mechanism, and implications for radical-initiated organic aerosol oxidation.* Journal of Physical Chemistry A, 2006. **110**(10): p. 3567-3577.

7. Knopf, D.A., et al., *Does atmospheric processing of saturated hydrocarbon surfaces by NO3 lead to volatilization?* Geophysical Research Letters, 2006. **33**(17): p. L17816.

8. Hearn, J.D. and G.D. Smith, *A mixed-phase relative rates technique for measuring aerosol reaction kinetics.* Geophysical Research Letters, 2006. **33**(17): p. L17805.

9. Finlayson-Pitts, B.J. and J.N.J. Pitts, *Chemistry of the Upper and Lower Atmosphere*. 2000, San Diego, CA: Academic Press. 969.

10. Wong, S.K., *An Indirect Measurement of the Absolute Rate-Constant of the Self-Reaction of Tert-Butoxy Radicals.* International Journal of Chemical Kinetics, 1981. **13**(5): p. 433-444.

11. Zhao, J. and R.Y. Zhang, *Proton transfer reaction rate constants between hydronium ion (H3O(+)) and volatile organic compounds.* Atmospheric Environment, 2004. **38**(14): p. 2177-2185.

12. Rondeau, D., R. Vogel, and J.C. Tabet, *Unusual atmospheric pressure chemical ionization conditions for detection of organic peroxides.* Journal of Mass Spectrometry, 2003. **38**(9): p. 931-940.

13. Schalley, C.A., et al., *On the cleavage of the peroxide O-O bond in methyl hydroperoxide and dimethyl peroxide upon protonation.* International Journal of Mass Spectrometry and Ion Processes, 1997. **163**(1-2): p. 101-119.

14. Wojcik, L. and K. Bederski, *Determination of the ion transmission coefficient for a mass spectrometer with a quadrupole ion analyzer.* International Journal of Mass Spectrometry and Ion Processes, 1996. **153**(2-3): p. 139-144.

15. Wood, K.V., A.H. Grange, and J.W. Taylor, *Mass Discrimination Effects in a Quadrupole Mass-Spectrometer.* Analytical Chemistry, 1978. **50**(12): p. 1652-1654.

16. *CRC Handbook of Chemistry and Physics*. 76 ed, ed. D.R. Lide. 1995, Boca Raton, FL: CRC Press, Inc.

17. Zhang, L.K., et al., *Accurate mass measurements by Fourier transform mass spectrometry.* Mass Spectrometry Reviews, 2005. **24**(2): p. 286-309.

18. Sterner, J.L., et al., *Signal suppression in electrospray ionization Fourier transform mass spectrometry of multi-component samples.* Journal of Mass Spectrometry, 2000. **35**(3): p. 385-391.

19. Walling, C., *Autoxidation*, in *Active Oxygen in Chemistry*, C.S. Foote, et al., Editors. 1995, Chapman & Hall: New York. p. 24-65.

20. Yin, H.Y., D.L. Hachey, and N.A. Porter, *Structural analysis of diacyl peroxides by electrospray tandem mass spectrometry with ammonium acetate: bond homolysis of peroxide-ammonium and peroxide-proton adducts.* Rapid Communications in Mass Spectrometry, 2000. **14**(14): p. 1248-1254.

21. Atkinson, R., *Gas-phase tropospheric chemistry of volatile organic compounds .1. Alkanes and alkenes.* Journal of Physical and Chemical Reference Data, 1997. **26**(2): p. 215-290.

22. Houston, P.L., *Chemical Kinetics and Reaction Dynamics*. 1 ed. 2001, New York, NY: McGraw-Hill.

23. Bennett, J.E. and R. Summers, *Product Studies of Mutual Termination Reactions of Sec-Alkylperoxy Radicals - Evidence for Non-Cyclic Termination.* Canadian Journal of Chemistry-Revue Canadienne De Chimie, 1974. **52**(8): p. 1377-1379.

24. Spanel, P., et al., *A SIFT study of the reactions of H3O+, NO+ and O-2(+) with hydrogen peroxide and peroxyacetic acid.* International Journal of Mass Spectrometry, 2003. **228**(2-3): p. 269-283.

25. Atkinson, R., et al., *Evaluated kinetic and photochemical data for atmospheric chemistry: Supplement VIII, halogen species - IUPAC Subcommittee on Gas Kinetic Data Evaluation for Atmospheric Chemistry.* Journal of Physical and Chemical Reference Data, 2000. **29**(2): p. 167-266.

26. Brooks, B.J., et al., *Size-differentiated volatility analysis of internally mixed laboratory-generated aerosol.* Journal of Aerosol Science, 2002. **33**(4): p. 555-579.

27. Wehner, B., et al., *Variability of non-volatile fractions of atmospheric aerosol particles with traffic influence.* Atmospheric Environment, 2004. **38**(36): p. 6081-6090.

28. Kuhn, T., et al., *Volatility of indoor and outdoor ultrafine particulate matter near a freeway.* Journal of Aerosol Science, 2005. **36**(3): p. 291-302.

29. Kuhn, T., et al., *Physical and chemical characteristics and volatility of PM in the proximity of a light-duty vehicle freeway.* Aerosol Science and Technology, 2005. **39**(4): p. 347-357.

30. Kalberer, M., et al., *Identification of polymers as major components of atmospheric organic aerosols.* Science, 2004. **303**(5664): p. 1659-1662.

31. *Duniway Product Literature*.

32. Lindinger, W., A. Hansel, and A. Jordan, *On-line monitoring of volatile organic compounds at pptv levels by means of proton-transfer-reaction mass spectrometry (PTR-MS) - Medical applications, food control and environmental research.* International Journal of Mass Spectrometry, 1998. **173**(3): p. 191-241.

CHAPTER 7

ANALYSIS OF COMPLEX PARTICLES USING AEROSOL CHEMICAL IONIZATION MASS SPECTROMETRY[1]

7.1 Introduction

As mentioned in Chapter 1, aerosols are found throughout the atmosphere and originate from a variety of sources [1]. Particles that make up aerosols are complex mixtures of perhaps hundreds of compounds. Some of the challenges that face the aerosol community are identifying and quantifying individual particle constituents in real time and accurately measuring and predicting particle reactivity. Aerosol mass spectrometry has become an excellent tool for addressing these challenges [2, 3].

Aerosol mass spectrometers vary in their vaporization, ionization, and mass filtering schemes. Thermal vaporization followed by chemical ionization has proven to be an effective approach to analyzing complex organic particles because of the low degree of fragmentation it offers compared to electron impact or multiphoton ionization. This "soft" ionization reduces overlap of ion peaks and simplifies spectra of multi-component mixtures allowing easier measurements of individual species. Chemical ionization has previously been used for studying the kinetics of and products from heterogeneous reactions of up to two component particles [4-7] as well as secondary organic aerosol formation in chamber studies [8-11].

---

[1] Hearn, J.D. and G.D. Smith, *Reactions and mass spectra of complex particles using A-CIMS.* International Journal of Mass Spectrometry, 2006. **258**(1-3): p. 95-103. Reproduced in part with permission of the publisher.

Here we demonstrate both on- and off-line measurements made with A-CIMS to highlight some of the advantages of this technique for analyzing complex aerosols. We first show on-line measurements of laboratory-generated and ambient aerosol to characterize this detection method, and then we test the performance of a real-time particle concentrator interfaced with A-CIMS. We also use off-line collection of particles to concentrate tobacco and wood smoke, meat cooking aerosol, and nonvolatile organic products from gas phase ozonolysis reactions for analysis by A-CIMS. This off-line collection technique is then used to concentrate ambient aerosol to demonstrate its utility.

7.2 Materials and Methods

Primary ions were generated as described in Chapter 2. The ion tube used was a ½ in. o.d. 24 cm long stainless steel tube heated to 220°C. Off-line collections of particles were made by sampling 5 standard liters per minute (slpm) of aerosol through a 2 in. section of heated ¼ in. o.d. stainless steel tube (300°C) to strip off nonvolatile organics with an oil-free rotary vane pump (Gast Manufacturing Inc.). This flow immediately entered a stainless steel U-tube (10 in.) immersed in an ice water bath (0°C) to condense the desorbed organics. Trapped organics were then desorbed directly into the ion tube of the A-CIMS by heating the condensation U-tube with heating rope and flowing 1 slpm N_2 through the tube. The temperature of the U-tube was raised to 300°C over seven minutes, but most organics were completely desorbed after only four minutes of heating.

Cigarette, white oak, and pine smokes were collected by first igniting the material in a natural gas flame, removing it from the flame and then pumping 5 slpm of the smoke

from the burning material through the collection apparatus. Ground beef (20% fat) was cooked over a natural gas flame, and the generated aerosol was drawn in to an evacuated flask and stored. These stored particles were then swept out with a small flow of N_2 into the collection U-tube.

Gases used were N_2 (99.99%, National Welders), O_2 (99.999%, National Welders), NO (CP grade, Matheson), and SF_6 (CP grade, Airgas). Ozone was generated as described in Chapter 3 and used immediately (orange peel and limonene experiments). Chemicals were purchased from Sigma-Aldrich and used without further purification: R-limonene (96%), oleic acid (90%), palmitic acid (99%), lauric acid (99%), ammonium sulfate (100%), and cholesterol (95%). Bis (2-ethylhexyl) sebacate (dioctyl sebacate, DOS, 97%) was purchased from Fluka and purified as described in section 5.2. Ground beef (80% lean, 20% fat) was purchased from a local grocery store.

7.3 On-line measurements

On-line measurement is the preferred method of detecting aerosol since it generates data in real time, and it bypasses the need for and problems associated with collecting and derivitizing a sample. In the following sections, I show results from on-line measurements made with A-CIMS. I begin by calibrating the instrument for ammonium sulfate, and then I show real-time measurements of ambient condensed phase sulfate. Since ambient condensed phase organics exist at several ng/m^3 or less [12], below the detection limit of A-CIMS, I will show some preliminary data on a real-time particle concentrator that reduces its on-line detection limit.

7.3.1 Detection of ambient sulfate in real time

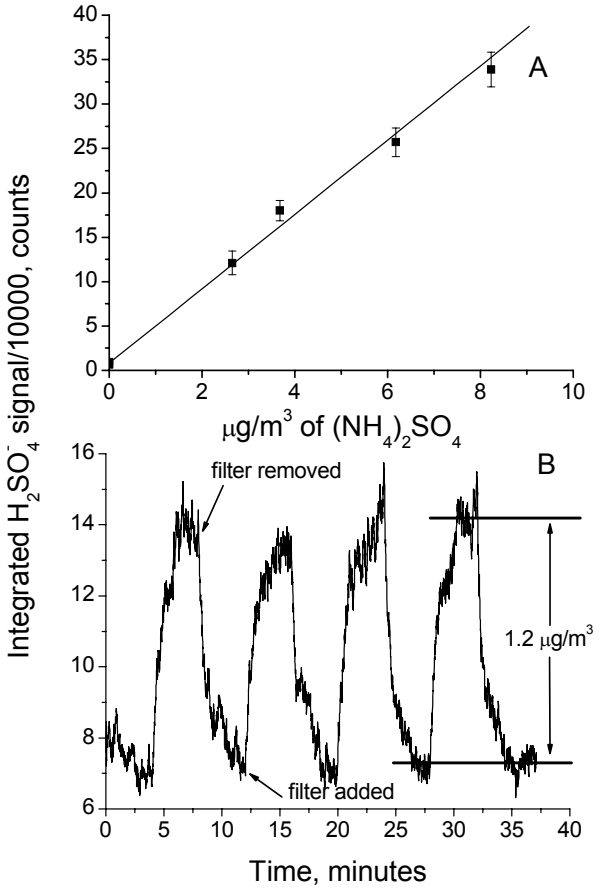

Figure 7.1 (A) Calibration of ammonium sulfate particles with A-CIMS and (B) data collected from ambient sulfate in real time using SF_6^- as the primary ion. A filter was either bypassed or not to separate gas and condensed phase sulfate signal. The linear fit in (A) was used to calculate the ambient particulate sulfate concentration (1.2 μg/m^3).

Sulfate can be found in ambient concentrations of several μg/m^3 [13], so A-CIMS may be a suitable technique to monitor sulfate concentrations in real time [14]. To test for this, A-CIMS was first calibrated by generating ammonium sulfate particles via heterogeneous nucleation as described in section 2.6. Particles were either sampled directly into the mass spectrometer or into a scanning mobility particle sizer (DMA

model 3081, TSI inc.) to determine the total mass concentration. Figure 7.1A shows the results from this calibration using SF_6^- as the primary ion, and with a signal-to-noise of 2, the detection limit is 64 ng/m^3, well below typical ambient ammonium sulfate concentrations.

We then sampled 6 slpm of outside air through conductive tubing and 1.5 slpm of this flow was sampled through the vaporizer into A-CIMS. A filter (0.3 μm pore size) was either placed in line to remove particles or bypassed to sample particles every 4 minutes, thereby separating gas and particle phase contributions to the signal. Results are shown in Figure 7.1B, and each time the filter is removed from the flow, the bisulfate (HSO_4^-) signal doubles, indicating there is a significant fraction of sulfate on particles. From our calibration, we determined the ambient condensed phase sulfate concentration to be 1.2 μg/m^3 (7.5x10^9 molecules/cm^3). This, however, does not give a measure of the ammonium sulfate since there are likely contributions to the sulfate signal from other sources such as condensed phase sulfuric acid and sodium sulfate. However, it is clear that A-CIMS can be used to monitor condensed phase species that are in a large abundance in the atmosphere in real time.

7.3.2 Real-time particle concentration

There are two approaches to detecting ambient organic aerosol with A-CIMS. The first is to reduce the detection limit of A-CIMS, but as discussed in Chapter 2, the instrument is performing near its optimum level (detection limit for oleic acid = 200 ng/m^3). Without some major design changes (see Chapter 8 for suggestions), A-CIMS detection cannot be improved to the level needed for real-time ambient organic aerosol detection (individual ambient organic concentration = 1-20 ng/m^3). The other approach

is to concentrate ambient particles in real-time before analysis with A-CIMS. This can be accomplished with a virtual impactor, provided the particles are large enough. Geller et al. have described the design of a particle concentrator that concentrates submicron particles by a factor of 30 [15]. The particles are grown by first saturating a 30 slpm flow with water vapor and then condensing the water vapor on the particles in a chilled condenser. The large particles (> 2 μm diameter) are then concentrated in a virtual impactor via inertial "impaction". Figure 7.2 shows a schematic of the virtual impactor, and the large particles continue on their trajectory into a minor flow (1 slpm) while the remaining flow (29 slpm) is discarded. The concentrated aerosol is then dried with a diffusion drier to return the particles to their original size.

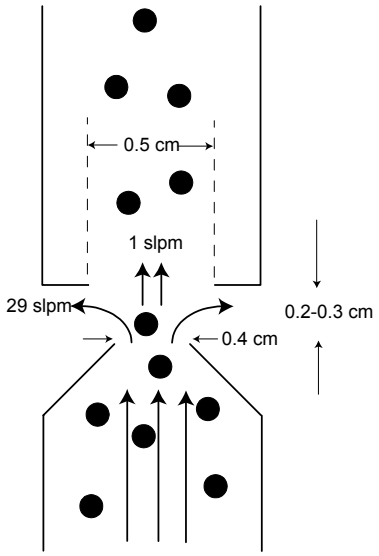

Figure 7.2. Design of the virtual impactor for concentration of super-micron particles. Particles remain on-axis and are sampled into the minor flow (1 slpm) and the major flow (29 slpm) is removed.

In order to test the performance of the real-time concentrator, DOS particles were generated using heterogeneous nucleation as described in section 2.6 and diluted into a 30 slpm total flow of N_2. The diluted aerosol was then analyzed with the SMPS to

determine the size distribution and the total particle concentration. The particles were then concentrated and the size distribution and number concentration were measured again with the SMPS. The results are plotted in Figure 7.3A showing that the particle size distribution is unaffected by concentration and the number concentration increases by a factor of 20. Therefore, the homemade concentrator is performing correctly.

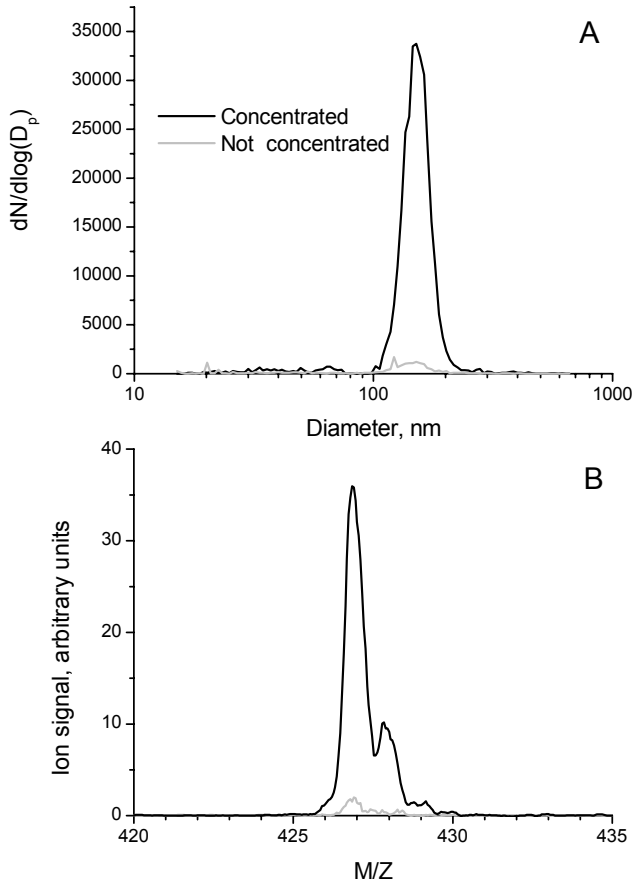

Figure 7.3. (A) SMPS data and (B) A-CIMS data of DOS particles that were either concentrated (black line) or not concentrated. Both measurements show an increase in signal of a factor of 20 and the size distribution (A) is unchanged by the concentrator.

Additionally, the concentrator was tested with A-CIMS, and mass spectra before and after particle concentration are shown in Figure 7.3B. The signal at m/z = 427

increases by a factor of 20 when the particles are concentrated, close to the theoretical amplification ($\times 30$) and consistent with the measured amplification from the SMPS data. This test demonstrates a relatively simple and inexpensive way of decreasing the detection limit of A-CIMS by over an order of magnitude. However, this only brings the *detection limit* of A-CIMS near ambient organic concentrations (≈ 20 ng/m^3). Ideally, the signal from ambient organics would be much higher than the detection limit so that accurate measurements can be made.

Even with the excellent performance of the real-time particle concentrator shown above, it is not without its faults. For instance, the particle concentrator does not always perform the same and the amplification factor seems to decrease over time. The latter problem is probably caused by asymmetric flow patterns from a build-up of water on the walls of the virtual impactor. The conical design of the virtual impactor shown in Figure 7.2 helps with this problem, but there may be other factors that are affecting its performance. If the virtual impactor is not aligned properly with the proper gap distance, it only concentrates particles by a factor of 2 or 3. More work needs to be done to stabilize the performance of this instrument before it can be used as a reliable particle concentrator.

7.4 Off-line measurements

While A-CIMS is well suited to monitor heterogeneous reactions and to detect some ambient condensed phase species that are in large abundance, it still lacks the detection capability necessary to make real-time measurements of individual organic compounds in the atmosphere. Additionally, it measures volatile, semivolatile, and nonvolatile components simultaneously making condensed phase partitioning

assignments cumbersome. In order to better characterize particulate emissions from several primary sources and to improve detection for ambient measurements, I collected particles off-line before analysis. In the sections that follow, I first characterize this method of collection with known mixtures and then I present results from several primary sources and one secondary source of aerosol. Finally, I show mass spectra from collected ambient aerosol.

7.4.1 Collection efficiency and desorption profiles

To determine the collection efficiency of the desorption/ condensation method for sampling organic particles, we generated 180 nm internally mixed particles containing oleic acid, palmitic acid, and myristic acid via heterogeneous nucleation. The particle mass spectra were then monitored in real time using A-CIMS, and the signal for each component decreased by 90% when passed through the U-tube collection apparatus (data not shown). The collection efficiency for these components is very high suggesting that this may be a convenient approach to concentrating nonvolatile organics from particles. However, there will be a collection bias against components that have extremely low volatilities such as ammonium sulfate which melts at 280ºC, and indeed we only collect 25% of the sulfate with this technique. While this bias is going to make quantification difficult, this method can still be valuable in identifying condensed phase components on particles.

Collected organics are expected to be liberated in the opposite order of their volatilities (most volatile to least volatile). In order to examine this under controlled conditions, small amounts (≈ 500 ng) of lauric acid, palmitic acid, oleic acid, and cholesterol were simultaneously deposited in the collection tube and desorbed into the

mass spectrometer. Figure 7.4 shows the normalized integrated signal for each organic demonstrating that the organics are in fact liberated in the opposite order of their boiling and melting points: lauric acid (m.p. = 48ºC, b.p. = 299ºC), palmitic acid (m.p. = 64ºC, b.p. = 354ºC), oleic acid (m.p. = 14ºC, b.p. = 360ºC) [16], and cholesterol (m.p. = 147ºC, b.p. = 360ºC) [17]. These desorption profiles add one more degree of separation so that one could, in principle, differentiate between two molecules of the same molecular weight if they have sufficiently different vapor pressures.

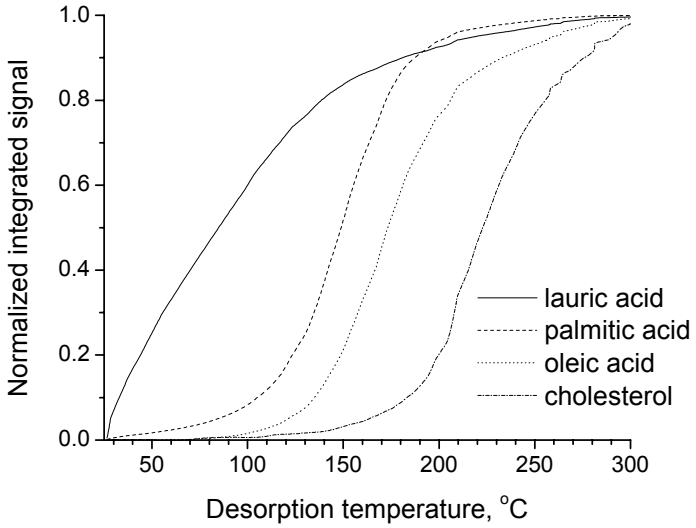

Figure 7.4. Desorption profiles of organics deposited in the collection tube. The organics desorb in the opposite order of their volatility.

7.4.2 Meat cooking aerosol

Off-line collection was used to record mass spectra of emissions from pan frying ground beef. Figure 7.5A shows a mass spectrum using proton transfer ionization of the collected aerosol as it is liberated from the tube. This snapshot of the collected sample shows several prominent peaks that correspond to organic acids which, as a class, comprise a large fraction of the total organic aerosol emitted from cooking ground beef

[12, 18]. Peaks at m/z = 145, 159, 173, 187, 255, 257, and 283 correspond to octanoic acid, nonanoic acid, decanoic acid, undecanoic acid, palmitoleic acid, palmitic acid, and oleic acid, respectively. There may be other contributions to these signals from other organics, but the organic acids listed above are expected to be the major contributors to signal at those masses.

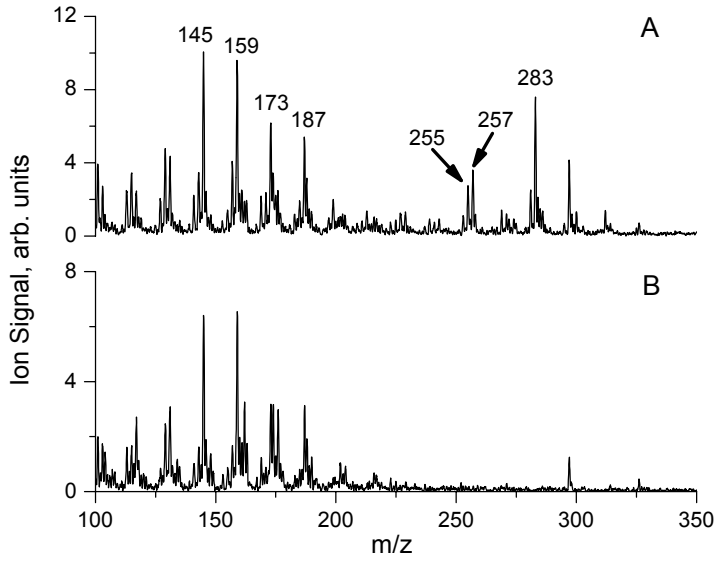

Figure 7.5. Mass spectra of collected meat cooking aerosol when the particles were either heated (A) or kept at room temperature (B) before the condensation tube. Higher m/z are missing in (B).

Perhaps another separation technique is to bias the collection for semivolatile components by not heating prior to the collection tube. Organics that exist both in the gas phase and in the particles at 25°C may still be collected in the condenser (0ºC). To test for this, suspended meat cooking aerosol was sent through two collection tubes in parallel, one heated to 300ºC and the other kept at room temperature before passing into the cold tube. Figure 7.5B shows the mass spectrum from unheated collection of meat cooking emissions. Interestingly, components with lower molecular weight that are

expected to have a higher vapor pressure are still trapped in the collection tube, but higher molecular weight species (m/z > 220 amu) are absent from the spectrum. Therefore, these high molecular weight organics are completely confined to the particles while the smaller ones partition to the gas phase. Of course, this measurement does not quantify the fraction of the semivolatile organics on the particles, but it does give qualitative results showing which organics significantly partition to the gas phase yet condense at 0°C.

7.4.3 Tobacco and wood smoke

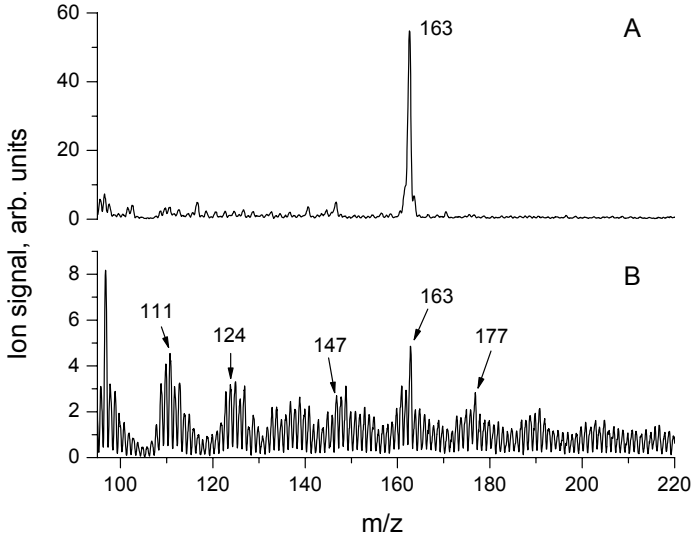

Figure 7.6. Mass spectra for collected cigarette smoke before (A) and after (B) the collection tube was heated. Peaks are identified in the text.

Smoke from cigarette, white oak, and pine combustion was analyzed off-line using A-CIMS. Figure 7.6 shows two snapshots of the mass spectrum as the sample from collected cigarette smoke is desorbed from the U-tube. Panel A shows the mass spectrum before the collection tube was heated (semivolatile organics) showing significant amounts of nicotine (m/z = 163) which is consistent with its high vapor pressure of 42.5

mTorr [19] and previous observations that it is found both in the gas phase and on particles [20]. Panel B shows the mass spectrum after a few minutes of heating. There is signal at every mass unit which is expected considering the complexity of the emitted aerosol [21]. Some of the larger peaks in the mass spectrum (m/z = 111, 124, 147, 163, and 177 amu) correspond to organic compounds that have been identified previously as condensed phase components on cigarette smoke (benzenediol, nicotinic acid, myosmine, nicotine, and cotinine, respectively) [21].

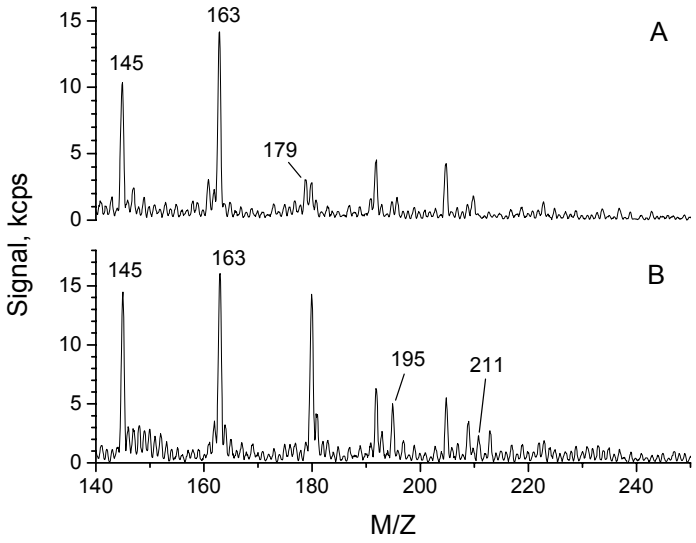

Figure 7.7. Mass spectra from collected pine (A) and white oak (B) smoke. Peaks are identified in the text.

Figure 7.7 shows a snapshot of the desorption of collected aerosol from burning pine (panel A) and white oak (panel B) woods. The dominant peak in both spectra (m/z = 163) is from levoglucosan (m.w. = 163 amu) which is a particle tracer for biomass burning [22]. Peaks at m/z = 195 and 211 probably correspond to methoxyeugenol (m.w. = 194 amu) and syringyl acetone (m.w. = 200 amu), respectively. Both of these organics are expected to be emitted in larger abundance from white oak combustion than pine [23,

24]. Additionally, a peak at m/z = 179 is present in larger relative abundance in the pine smoke spectrum than white oak and could be from coniferyl aldehyde (m.w. = 178 amu) [24]. The large peak at m/z = 145 is most likely a fragment peak from levoglucosan (water loss). Of course, there may be contributions from other organics to these peaks, but the relative difference between these two spectra is expected based on what is known about emissions from oak and pine combustion.

7.4.4 Secondary organic aerosol

Ozone reacts with volatile emissions from orange peel to form low volatility products that in high enough concentration can form new particles [25]. This is not likely to be an important process in ambient particle formation, but these low volatility products will probably condense onto existing particles. To investigate the products from this reaction, we filled a 500 mL flask with ozone and inserted a piece of orange peel. Particles were immediately visible, and they were swept out with a small flow of O_2/O_3 and collected in the collection tube. The products were then analyzed via A-CIMS, and Figure 7.8A shows a mass spectrum from desorbing the ozonolysis products. R-limonene is expected to be the major gas phase emission from orange peel that is reactive with ozone [26], and it is known to form low volatility products [27-29]. In a separate experiment, we put a drop of R-limonene in the ozone filled flask and collected the particles off-line, and Figure 7.8B shows a product mass spectrum from this reaction.

Many of the prominent peaks in the R-limonene spectrum are also present in the orange peel spectrum which is consistent with the fact that it is the dominant organic emitted. Peaks at m/z = 169, 171, 185, 187, and 201 correspond to limonaldehyde, limonalic acid, limononic acid, limonic acid, and 7-hydroxy-limononic acid, respectively

[30]. Significant amounts of products at higher molecular weight are also visible in the spectra of both the orange peel and R-limonene reactions which could be from secondary chemistry. Stabilized Criegee intermediates are known to react with carboxylic acids and aldehydes to form larger molecular weight products and oligomers [31], and recent studies have suggested that Criegee intermediates can react with carbon-carbon double bonds to generate large molecules [32]. In any case, it is clear from the product mass spectra that additional chemistry is occurring.

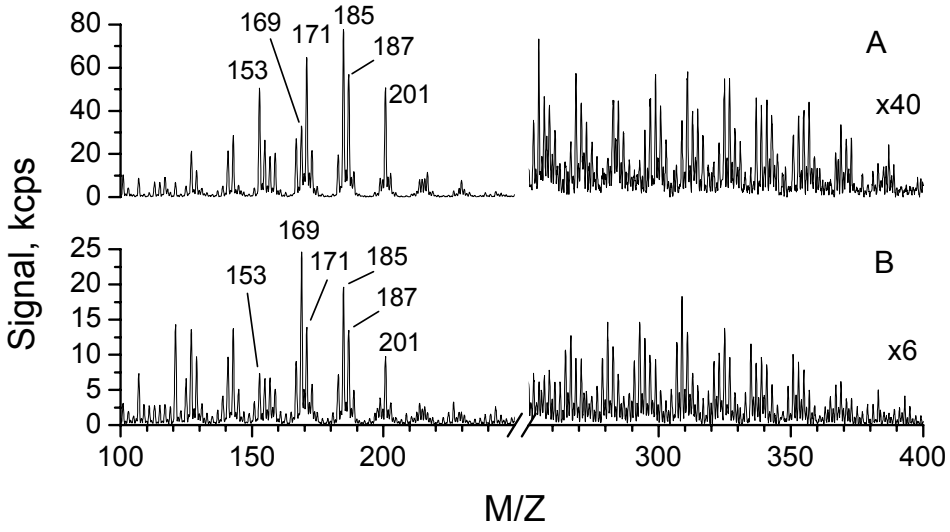

Figure 7.8. Mass spectra from the reaction of ozone with volatile emissions from orange peel (A) and R-limonene (B). Peaks are identified in the text. The large molecular weight peaks suggest the formation of oligomers.

7.4.5 Ambient Sampling

This off-line collection method allows concentration of aerosol particles to allow detection of organics that would otherwise be below the detection limit for A-CIMS. To extend this technique to ambient sampling, outside air (5 slpm) was drawn through two collection tubes in parallel, and the air was filtered before entering one of the collection

tubes. The parallel runs ensure that collected organics are not artifacts of the technique but actually come from ambient aerosol. Figure 7.9 shows a mass spectrum of the collected organics as they are desorbed into the A-CIMS with peaks at nearly every mass-to-charge ratio. Analysis of the filtered sample showed no collected organics (data not shown). Upon closer inspection of Figure 7.9, it is clear that the peaks are in groups spaced by 14 amu (see hash marks). This is typical of functionalized organic molecules that are separated by $-CH_2-$ groups, and these results are similar to those reported recently from Germany using another soft ionization technique [8-11, 33]. The distribution of the detected organic molecules may be indicative of aged particles. The prominent peaks at even mass-to-charge ratio suggest the presence of nitrogen-containing functional groups. Organic molecules with an odd number of nitrogen atoms have odd molecular weights, but since we are using proton transfer ionization, they show up at even m/z. This large abundance of nitrogen-containing molecules has three likely explanations. First, the sampling site is in Athens, GA, a rural town surrounded by agriculture, and agricultural processes often emit nitrogen containing compounds [34-36]. Second, the sampling site is approximately one mile from a wastewater treatment plant which emits amines [37]. Finally, NO_3 could be reacting with organic molecules to form organic nitrates [38]. All three of these sources could explain the apparent presence of amines or nitrates in the mass spectrum, but at this point, we cannot determine their relative importance.

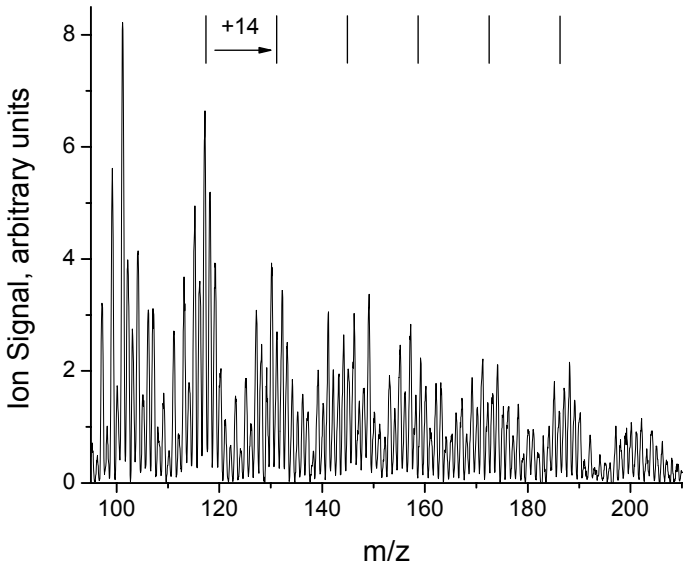

Figure 7.9. Mass spectrum of collected ambient aerosol in Athens, GA showing groups of peaks every 14 amu (see hash marks). The prominent peaks at even m/z suggests the presence of nitrogen containing compounds.

7.5 Conclusions and Future Direction

A-CIMS is a powerful tool for studying laboratory generated particles and heterogeneous reactions, and steps have been taken to apply this technique to detecting ambient aerosol. We have shown that it is possible to measure sulfate concentrations on ambient particles in real time. Additionally, A-CIMS simultaneously monitors gas phase species and simply placing a filter in line allows determination of gas phase concentrations to ion signals. On-line particle concentration improves the detection capability of A-CIMS by more than an order of magnitude, but the detection limit needs to be reduced even more in order to quantitatively measure organics with low concentrations ($\approx$ 20 ng/m^3). Spectra from off-line collection demonstrate the utility of the U-tube collection technique, and abundant particle tracer species, such as

levoglucosan from wood smoke, are easily detected from primary emissions. The low degree of fragmentation allows large molecular weight products from R-limonene ozonolysis to be detected suggesting the formation of oligomers through secondary chemistry. Finally, to extend this technique to detecting individual ambient organics, outdoor particles were collected off-line, and the spectrum was consistent with highly functionalized organics. Definitive assignments of the peaks in these complex aerosols are impractical without an additional separation technique such as GC or MS/MS, but these could be easily combined with A-CIMS.

References

1. Finlayson-Pitts, B.J. and J.N.J. Pitts, *Chemistry of the Upper and Lower Atmosphere*. 2000, San Diego, CA: Academic Press. 969.

2. Suess, D.T. and K.A. Prather, *Mass Spectrometry of Aerosols.* Chemical Reviews, 1999. **99**: p. 3007-3035.

3. Noble, C.A. and K.A. Prather, *Real-time single particle mass spectrometry: A historical review of a quarter century of the chemical analysis of aerosols.* Mass Spectrometry Reviews, 2000. **19**: p. 248-274.

4. Hearn, J.D., A.J. Lovett, and G.D. Smith, *Ozonolysis of oleic acid particles: evidence for a surface reaction and secondary reactions involving Criegee intermediates.* Physical Chemistry Chemical Physics, 2005. **7**(3): p. 501-511.

5. Hearn, J.D. and G.D. Smith, *Kinetics and product studies for ozonolysis reactions of organic particles using aerosol CIMS.* Journal of Physical Chemistry A, 2004. **108**(45): p. 10019-10029.

6. Hearn, J.D. and G.D. Smith, *Measuring rates of reaction in supercooled organic particles with implications for atmospheric aerosol.* Physical Chemistry Chemical Physics, 2005. **7**(13): p. 2549-2551.

7. Hearn, J.D. and G.D. Smith, *A mixed-phase relative rates technique for measuring aerosol reaction kinetics.* Geophysical Research Letters, 2006. **33**(17): p. L17805.

8. Hoffmann, T., et al., *On-line characterization of gaseous and particulate organic analytes using atmospheric pressure chemical ionization mass spectrometry.* Spectrochimica Acta Part B-Atomic Spectroscopy, 2002. **57**(10): p. 1635-1647.

9. Warscheid, B. and T. Hoffmann, *On-line measurements of a-pinene ozonolysis products using an atmospheric pressure chemical ionisation ion-trap mass spectrometer.* Atmospheric Environment, 2001. **35**(16): p. 2927-2940.

10. Warscheid, B. and T. Hoffmann, *Structural elucidation of monoterpene oxidation products by ion trap fragmentation using on-line atmospheric pressure chemical ionisation mass spectrometry in the negative ion mode.* Rapid Communications in Mass Spectrometry, 2001. **15**(23): p. 2259-2272.

11. Kuckelmann, U., S. Warscheid, and T. Hoffmann, *On-line characterization of organic aerosols formed from biogenic precursors using atmospheric pressure chemical ionization mass spectrometry.* Analytical Chemistry, 2000. **72**(8): p. 1905-1912.

12. Rogge, W.F., et al., *Sources of Fine Organic Aerosol .1. Charbroilers and Meat Cooking Operations.* Environmental Science & Technology, 1991. **25**(6): p. 1112-1125.

13. Walker, J.T., et al., *Inorganic PM2.5 at a US agricultural site.* Environmental Pollution, 2006. **139**(2): p. 258-271.

14. Smith, J.N., et al., *Chemical composition of atmospheric nanoparticles during nucleation events in Atlanta.* Journal of Geophysical Research-Atmospheres, 2005. **110**(D22): p. -.

15. Geller, M.D., et al., *A new compact aerosol concentrator for use in conjunction with low flow-rate continuous aerosol instrumentation.* Journal of Aerosol Science, 2005. **36**(8): p. 1006-1022.

16. Stull, D.R., *Vapor Pressure of Pure Substances - Organic Compounds.* Industrial and Engineering Chemistry, 1947. **39**(4): p. 517-540.

17. Brown, R.L. and S.E. Stein, *Boiling Point Data*, in *NIST Chemistry WebBook, Nist Standard Reference Database Number 69*, P.J. Linstrom and W.G. Mallard, Editors. 2005, National Institute of Standards and Technology: Gaithersburg MD.

18. McDonald, J.D., et al., *Emissions from charbroiling and grilling of chicken and beef.* Journal of the Air & Waste Management Association, 2003. **53**(2): p. 185-194.

19. Norton, L.B., C.R. Bigelow, and W.B. Vincent, *Partial vapor pressures from nicotine solutions at 25 Deg.* Journal of the American Chemical Society, 1940. **62**: p. 261-4.

20. Pankow, J.F., *A consideration of the role of gas/particle partitioning in the deposition of nicotine and other tobacco smoke compounds in the respiratory tract.* Chemical Research in Toxicology, 2001. **14**(11): p. 1465-1481.

21. Rogge, W.F., et al., *Sources of Fine Organic Aerosol .6. Cigarette-Smoke in the Urban Atmosphere.* Environmental Science & Technology, 1994. **28**(7): p. 1375-1388.

22. Simoneit, B.R.T., et al., *Levoglucosan, a tracer for cellulose in biomass burning and atmospheric particles.* Atmospheric Environment, 1999. **33**(2): p. 173-182.

23. Schauer, J.J. and G.R. Cass, *Source Apportionment of Wintertime Gas-Phase and Particle-Phase Air Pollutants Using Organic Compounds as Tracers.* Environmental Science and Technology, 2000. **34**(9): p. 1821-1832.

24. Fine, P.M., G.R. Cass, and B.R.T. Simoneit, *Chemical characterization of fine particle emissions from the wood stove combustion of prevalent United States tree species.* Environmental Engineering Science, 2004. **21**(6): p. 705-721.

25. Andino, J.M., et al., *A classroom demonstration of the formation of aerosols from biogenic hydrocarbons.* Journal of Chemical Education, 2000. **77**(12): p. 1584-1586.

26. Lund, E.D., et al., *Quantitative Composition Studies of Water-Soluble Aromatics from Orange Peel.* Journal of Agricultural and Food Chemistry, 1972. **20**(3): p. 685-&.

27. Wainman, T., et al., *Ozone and limonene in indoor air: A source of submicron particle exposure.* Environmental Health Perspectives, 2000. **108**(12): p. 1139-1145.

28. Jonsson, A.M., M. Hallquist, and E. Ljungstrom, *Impact of humidity on the ozone initiated oxidation of limonene, Delta(3)-carene, and alpha-pinene.* Environmental Science & Technology, 2006. **40**(1): p. 188-194.

29. Zhang, J.Y., et al., *Secondary organic aerosol formation from limonene ozonolysis: Homogeneous and heterogeneous influences as a function of NOx.* Journal of Physical Chemistry A, 2006. **110**(38): p. 11053-11063.

30. Leungsakul, S., M. Jaoui, and R.M. Kamens, *Kinetic mechanism for predicting secondary organic aerosol formation from the reaction of d-limonene with ozone.* Environmental Science & Technology, 2005. **39**(24): p. 9583-9594.

31. Rebrovic, L., *The Peroxidic Species Generated by Ozonolysis of Oleic Acid or Methyl Oleate in a Carboxylic Acid Medium.* Journal of the American Oil Chemists Society, 1992. **69**(2): p. 159-165.

32. Katrib, Y., et al., *Products and mechanisms of ozone reactions with oleic acid for aerosol particles having core-shell morphologies.* Journal of Physical Chemistry A, 2004. **108**(32): p. 6686-6695.

33. Warscheid, B., U. Kuckelmann, and T. Hoffmann, *Direct quantitative analysis of organic compounds in the gas and particle phase using a modified atmospheric pressure chemical ionization source in combination with ion trap mass spectrometry.* Analytical Chemistry, 2003. **75**(6): p. 1410-1417.

34. Aneja, V.P., et al., *Agricultural ammonia emissions and ammonium concentrations associated with aerosols and precipitation in the southeast United States.* Journal of Geophysical Research-Atmospheres, 2003. **108**(D4): p. -.

35. Anderson, N., R. Strader, and C. Davidson, *Airborne reduced nitrogen: ammonia emissions from agriculture and other sources.* Environment International, 2003. **29**(2-3): p. 277-286.

36. Lammel, G., et al., *Aerosols emitted from a livestock farm in southern Germany.* Water Air and Soil Pollution, 2004. **154**(1-4): p. 313-330.

37. Manahan, S.E., *Environmental Chemistry*. 6 ed. 1994, Boca Raton, FL: CRC Press Inc.

38. Docherty, K.S. and P.J. Ziemann, *Reaction of oleic acid particles with NO3 radicals: Products, mechanism, and implications for radical-initiated organic aerosol oxidation.* Journal of Physical Chemistry A, 2006. **110**(10): p. 3567-3577.

CHAPTER 8

CONCLUSIONS AND FUTURE DIRECTION

8.1 A-CIMS advantages and disadvantages

Aerosol chemical ionization mass spectrometry (A-CIMS) has proven to be a useful tool in analyzing organic aerosol composition and reactivity [1-6]. The primary advantage of A-CIMS is the low degree of fragmentation achieved through this "soft" ionization. This often enables detection of intact molecular ions which simplifies spectra and the fragments that do appear are usually unique to the parent ion, limiting overlap of signals with other functionalized organics. This also makes quantification easier since most of the ion signal is contained in one peak. In addition, fragmentation can be induced by raising the temperature on the ion tube. This can add confidence to peak assignments and could, in principle, give some structural information. In addition to the soft ionization, chemical ionization is also flexible and can be tailored to ionize a species of interest.

A-CIMS also detects gases and particles, so it is truly an "aerosol" mass spectrometer. This gives more complete information since gas and condensed phase measurements are made simultaneously, so in monitoring heterogeneous reactions, A-CIMS (unlike particle mass spectrometers) is not blind to gas phase products. Unfortunately, this also makes gas-particle partitioning assignments cumbersome, but as discussed in Chapters 3 and 6, the particles can either be directed away from the vaporizer inlet or a filter can be placed in-line to determine which products partition to the gas phase.

The last major advantage of A-CIMS is that it has a very simple design. In fact, Hoffmann and coworkers simply modified the inlet to a commercial proton transfer reaction mass spectrometer to detect aerosol particles [7]. A-CIMS requires no critical alignment for sampling the particles into the vaporizer, whereas in other particle mass spectrometers they must be directed to a heated block or laser ablation spot. Additionally, accurate timing is not required for vaporizing or ionizing a particle with lasers since A-CIMS does not use lasers. This can be a challenging task since the particle vapor plume and the laser shot must overlap each other in space and time to get enough ion signal. The simple design of A-CIMS makes it an attractive analytical tool to measure particle composition.

Although there are some clear advantages to A-CIMS, it is not without fault. The primary disadvantage of this detection method is that it has a relatively high detection limit. Single particle mass spectrometers are sensitive enough to detect the material in one particle, whereas A-CIMS can only detect condensed phase organics down to ≈ 200 ng/m^3 without the aid of a concentrator. However, this is only a problem for measurement of ambient aerosol and not for laboratory studies.

8.2 A-CIMS as a tool for studying particle evolution

A-CIMS is particularly well-suited for monitoring heterogeneous reactions in a laboratory setting where relatively high concentrations of individual organics are used. We first measured the kinetics and products from reactions between oleic acid and ozone to demonstrate that A-CIMS can be used quantitatively, and the results reconciled some discrepancies among previously published work. In the case of oleic acid ozonolysis, secondary chemistry affects both the kinetics of the reaction and the observed product

distribution. These results emphasize the need to account for secondary chemistry before equating condensed phase losses to gas phase losses.

Kinetics of radical initiated oxidation of organic aerosol was also investigated using a mixed phase relative rates approach. Since A-CIMS can be used to monitor both the gas and particle phase signals simultaneously, it can be used for such a measurement. The radical initiated reactions were faster than the upper limit of the uptake coefficient (unity), suggesting that secondary chemistry is involved in further oxidation of the particles. The radical chain was at least 2 for both OH and Cl initiated reactions.

Finally, A-CIMS was used to measure the reactivity of internally mixed particles. Solid components slowed the reaction down, but this was dependent on the interactions between the solid and liquid components. The low degree of fragmentation also enabled the reactivity of meat cooking aerosol to be measured, and some of the oleic acid present was unreactive with ozone, consistent with the binary mixture results.

8.3 Future Direction

As mentioned above, the primary disadvantage with A-CIMS is the "high" detection limit. In the sections that follow, I will give three suggestions for improvement. They are ordered in their ease of implementation with the last suggestion being what might be called a "pipe dream".

8.3.1 Development of a real-time concentrator

As discussed in section 7.3, a real-time concentrator [8] can improve the detection capability of A-CIMS by over an order of magnitude. This approach does not really decrease the detection limit of A-CIMS; it only brings the particle concentration up.

However, it does work, and it needs some additional improvements in order to be a reliable source of particle concentration. When the instrument is working, the amplification does not stay constant, rather it drifts downward (lower amplification). Here are two possible explanations for this drift. First, there may be water build-up in or just before the virtual impactor that causes turbulence in the air flow. If this alters the particle trajectory, it could have devastating effects on the impactor function. Second, the particle growth may not be uniform in time. This would be caused by a lower supersaturation as a result of either a lower temperature in the saturator or a higher temperature in the condenser. The latter seems more likely since cooling a 30 slpm flow of air requires a large amount of heat transfer and the condenser is made out of glass. A simple solution to this is to make a condenser out of stainless steel to have better heat transfer.

Even if the particle concentrator were working to perfection, it would only reduce the detection limit of A-CIMS to approximately 10 ng/m^3. This is near the ambient concentration of many organic molecules, but in order to make quantitative measurements, the detection limit needs to be much lower than the concentration of the sample. There is another way of improving A-CIMS as discussed in the next section.

8.3.2 Ion funnel

Since A-CIMS uses high pressure (≈ 40 Torr) for ionization, a significant pressure drop must be achieved before ion detection (≈ 10^{-5} Torr). Currently, the ions are sampled in through a 200 μm diameter orifice and a small potential gradient (≈ 3V) to get the ions into high vacuum. Unfortunately, most of the ions are pumped away with the diaphragm pump, so an easy way of improving the detection limit is to sample more ions into the

high-vacuum chamber. Currently, a smaller A-CIMS instrument is under construction where a collisional dissociation chamber is added as an additional stage of pumping. This allows the flow limiting orifices to be opened up to increase the throughput of the ions. This chamber houses a series of electrostatic lenses where the voltage is incrementally dropped over the length of the chamber which increases the transmission of the ions. Unfortunately, this chamber has a relatively high pressure (≈ 0.5 Torr), so a static electric field does not transport the ions effectively.

A better solution is to replace the static lenses with an ion funnel. Ion funnels, like the static lenses, have a voltage drop down the length of the funnel, but there is also quadrupole RF field applied. The dynamic electric field corrects ion trajectories after collisions and improves ion transmission through a high pressure region. Ion funnels are used in many commercial instruments, and it increases the signal by over an order of magnitude [9]. Such an improvement on A-CIMS would be well worth the effort and could enable its use in field measurements.

8.3.3 Single particle CIMS

One of the advantages of single particle mass spectrometers is that they differentiate particles from different sources if tracers are present. A lofty goal is to marry the single particle mass spectrometer with chemical ionization. Rate constants for proton transfer reactions are near collision rate (≈ 10^{-9} cm^3/molecule/sec.) [10], so the limiting factor in single particle chemical ionization will be the number of ion-molecule collisions. Particles with a diameter of 1 μm have approximately 10^{10} molecules, and during the initial expansion of the particle vapor plume, there will be a high density of molecules. Therefore, neutral molecules will not limit the number of collisions, and the

challenge will be generating a high enough flux of primary ions. A first approach might be to use electron impact ionization to generate N_2^+ and draw the ions into the vapor plume with a small negative potential. Ideally, the primary ions will have no kinetic energy to minimize fragmentation of the organic molecules, so an approach similar to electron capture ionization may be convenient. Following chemical ionization, the product ions can be pulse extracted into a time-of-flight mass spectrometer to generate an entire mass spectrum from a single particle. While this is a lofty goal, it is currently being developed in Kim Prather's group [11].

8.4 Concluding remarks

Heterogeneous chemistry is an exciting field to be working in, and I am glad to have made a small contribution to the understanding of organic particle evolution through my work with A-CIMS. There is still a lot of work to do and plenty of room for improving the performance of A-CIMS. I am confident that A-CIMS will be instrumental (chuckles) in advancing our understanding of heterogeneous reactions in the coming years.

References

1. Hearn, J.D., A.J. Lovett, and G.D. Smith, *Ozonolysis of oleic acid particles: evidence for a surface reaction and secondary reactions involving Criegee intermediates.* Physical Chemistry Chemical Physics, 2005. **7**(3): p. 501-511.

2. Hearn, J.D. and G.D. Smith, *Kinetics and product studies for ozonolysis reactions of organic particles using aerosol CIMS.* Journal of Physical Chemistry A, 2004. **108**(45): p. 10019-10029.

3. Hearn, J.D. and G.D. Smith, *A chemical ionization mass spectrometry method for the online analysis of organic aerosols.* Analytical Chemistry, 2004. **76**(10): p. 2820-2826.

4. Hearn, J.D. and G.D. Smith, *Measuring rates of reaction in supercooled organic particles with implications for atmospheric aerosol.* Physical Chemistry Chemical Physics, 2005. **7**(13): p. 2549-2551.

5. Hearn, J.D. and G.D. Smith, *A mixed-phase relative rates technique for measuring aerosol reaction kinetics.* Geophysical Research Letters, 2006. **33**(17): p. L17805.

6. Hearn, J.D. and G.D. Smith, *Reactions and mass spectra of complex particles using Aerosol CIMS.* International Journal of Mass Spectrometry, 2006. **258**(1-3): p. 95-103.

7. Kuckelmann, U., S. Warscheid, and T. Hoffmann, *On-line characterization of organic aerosols formed from biogenic precursors using atmospheric pressure chemical ionization mass spectrometry.* Analytical Chemistry, 2000. **72**(8): p. 1905-1912.

8. Geller, M.D., et al., *A new compact aerosol concentrator for use in conjunction with low flow-rate continuous aerosol instrumentation.* Journal of Aerosol Science, 2005. **36**(8): p. 1006-1022.

9. Shaffer, S.A., et al., *An ion funnel interface for improved ion focusing and sensitivity using electrospray ionization mass spectrometry.* Analytical Chemistry, 1998. **70**(19): p. 4111-4119.

10. Zhao, J. and R.Y. Zhang, *Proton transfer reaction rate constants between hydronium ion (H3O(+)) and volatile organic compounds.* Atmospheric Environment, 2004. **38**(14): p. 2177-2185.

11. Prather, K., *Personal Communication*. 2006.

APPENDIX A

COMPUTER ALGORITHMS

Algorithm for determining gamma from a polydisperse aerosol:

```
#include <origin.h>
bf(int points, float lower, float step, int steps)
/* function to sum up particle decays for a distribution of particle sizes */
{
	int i,j,k;
	float sum=0,a,c,lowest,diff[100];
	a=3/2.46e19*3.6e4/8/82.057/298/3.16*1000*1e7;
	Dataset size("data1",0);
	Dataset n("data1",1);
	Dataset time("data3",0);
	Dataset OA("data3",2);
	Dataset time_real("data5",0);
	Dataset OA_real("data5",2);
	Dataset OA_calc("data5",4);
	Dataset OA_final("data3",4);
	lowest=0;
	for(k=0; k<steps; k++)
	{
		c = a*(lower+k*step);
		sum=0;
		for(j=0; j<51; j++)
			sum += size[j]^3*n[j];
		for(i=0; i<2000; i++)
		{
			OA[i]=0;
			for(j=0; j<51; j++)
				if((size[j]/2/c) >= time[i])
					OA[i] += (1-2*c/size[j]*time[i])^2*size[j]^3*n[j];
			OA[i] /= sum;
		}
		diff[k] = 0;
		for(i=0;i<points;i++)
			diff[k] += (OA[round(time_real[i]/1e13,0)]-OA_real[i])^2;
		printf("gamma: %f   diff: %f\n",(lower+k*step),diff[k]);
		if(diff[k]<=diff[lowest])
		{
			lowest=k;
			for(i=0;i<points;i++)
				OA_calc[i] = OA[round(time_real[i]/1e13,0)];
			OA_final = OA;
```

```
                }
        }       printf("gamma: %f\n",lower+lowest*step);
}
```

Algorithm for determining gamma with a quadratic function without increasing after it reaches the minimum:

```
#include <origin.h>
sqrt(int points)
/* function to fit a decay curve with a square root function without turning up */
{
	int i,j,k;
	float
slope=0,diff,lowest=10000000,best1=0,best2=0,best3=0,best4=0,max=0,calc[100];
	Dataset exposure("data1",0);
	Dataset signal("data1",3);
	Dataset error("data1",4);
	Dataset exposurecalc("data1",5);
	Dataset bestfit("data1",6);
	for(i=0;i<points;i++)
	{
		if(exposure[i]>max)
			max=exposure[i];
	}
	/* calculates exposure values for best fit curve (100 points) */
	for(i=0;i<100;i++)
		exposurecalc[i]=max*i/100;
	for(j=0;j<10;j++) /* calculates the nearest power of 10 for the slope */
	{
		slope=10^(-10-j);
		for(i=0;i<points;i++)
		{
			if(exposure[i]*slope>=1)
				calc[i]=0;
			if(exposure[i]*slope<1)
				calc[i]=(1-slope*exposure[i])^2;
		}
		diff=0;
		for(i=0;i<points;i++)
			diff += 1/(error[i]/signal[i])^2*(signal[i]-calc[i])^2;
		printf("slope: %f error:%f\n",(slope*1e16),diff);
		if(diff <= lowest)
		{
			lowest = diff, best1 = slope;
		}
	}
	best2=best1;
	for(k=0;k<2;k++) /* calculates the first significant digit */
	{
	for(j=0;j<10;j++)
```

```
{
        slope=best1/(10^(1-k))*j;
        for(i=0;i<points;i++)
        {
                if(exposure[i]*slope>=1)
                        calc[i]=0;
                if(exposure[i]*slope<1)
                        calc[i]=(1-slope*exposure[i])^2;
        }
        diff=0;
        for(i=0;i<points;i++)
                diff += 1/(error[i]/signal[i])^2*(signal[i]-calc[i])^2;
        printf("slope: %f error:%f\n",(slope*1e16),diff);
        if(diff <= lowest)
        {
                lowest = diff, best2 = slope;
        }
}
}
k=100;
if(best2>=best1)
        k=10;
best3=best2;
for(j=0;j<20;j++) /* calculates the second significant digit */
{
        slope=(best2-best1/(k/10)+best1/k*j);
        for(i=0;i<points;i++)
        {
                if(exposure[i]*slope>=1)
                        calc[i]=0;
                if(exposure[i]*slope<1)
                        calc[i]=(1-slope*exposure[i])^2;
        }
        diff=0;
        for(i=0;i<points;i++)
                diff += 1/(error[i]/signal[i])^2*(signal[i]-calc[i])^2;
        printf("slope: %f error:%f\n",(slope*1e16),diff);
        if(diff <= lowest)
                lowest = diff, best3 = slope;
}
best4=best3;
k=1000;
if(best2>=best1)
        k=100;
for(j=0;j<20;j++) /* calculates the third significant digit */
{
```

```
                slope=(best3-best1/(k/10)+best1/k*j);
                for(i=0;i<points;i++)
                {
                        if(exposure[i]*slope>=1)
                                calc[i]=0;
                        if(exposure[i]*slope<1)
                                calc[i]=(1-slope*exposure[i])^2;
                }
                diff=0;
                for(i=0;i<points;i++)
                        diff += 1/(error[i]/signal[i])^2*(signal[i]-calc[i])^2;
                printf("slope: %f error:%f\n",(slope*1e16),diff);
                if(diff <= lowest)
                        lowest = diff, best4 = slope;
        }
        for(i=0;i<100;i++)
        {
                if(exposurecalc[i]*best4>=1)
                        bestfit[i]=0;
                if(exposurecalc[i]*best4<=1)
                        bestfit[i]=(1-best4*exposurecalc[i])^2;
        }
        printf("bestslope: %f error:%f\n",(best4*1e16),lowest);
}
```